

AN ABSTRACT OF THE THESIS OF

Peter Gumplinger for the degree of Doctor of Philosophy in Physics  
presented on November 7, 1986.

Title: A Measurement of the Neutral Pion Form Factor by Means of the  
Reaction  $\pi^0 \rightarrow e^+ e^- \gamma$ .

Abstract approved: Redacted for Privacy  
Albert W. Stetz

The slope parameter "a" of the  $\pi^0$ -electromagnetic transition form factor was obtained from a measurement of the partial branching ratio of the Dalitz decay  $\pi^0 \rightarrow e^+ e^- \gamma$  into high invariant-mass electron-positron pairs. The experiment was carried out at the TRIUMF cyclotron laboratory. A beam of  $\pi^-$  mesons was stopped in a liquid hydrogen target to produce neutral pions in the reaction  $\pi^- p \rightarrow n \pi^0$ . The electron-positron pairs were detected with two delay-line chamber telescopes, each followed by a large NaI crystal. A third NaI crystal measured the number of  $\pi^0$ 's in the target by counting the photons from the decay  $\pi^0 \rightarrow \gamma \gamma$ .

Data was taken at three detector opening angles  $60^\circ$ ,  $130^\circ$  and  $156^\circ$ . The  $60^\circ$  measurement confirms our normalization. A value  $a = -0.01 \pm 0.035^{+0.07}_{-0.05}$ , where the first error is due to statistics and the second is an estimate of systematic effects, was obtained

from the  $130^\circ$  geometry. This value does not support the result of the most recent previous experiment and is in accord with most theoretical calculations indicating that there is no unexpected structure in the  $\pi^0$  decay form factor.

A MEASUREMENT OF THE NEUTRAL PION FORM FACTOR BY

MEANS OF THE REACTION  $\pi^0 \rightarrow e^+ e^- \gamma$

by

Peter Gumplinger

A Thesis

submitted to

Oregon State University

in partial fulfillment of  
the requirements for the  
degree of

Doctor of Philosophy

Completed November 7, 1986

Commencement June 1987

APPROVED:

Redacted for Privacy

---

Professor of Physics in charge of major

Redacted for Privacy

---

Chairman of Department of Physics

Redacted for Privacy

---

Dean of Graduate School

Date thesis is presented November 7, 1986

Typed by Peter Gumplinger for Peter Gumplinger

## ACKNOWLEDGEMENTS

This experiment and thesis could not have been successful without the help of a great many people. I wish to thank my collaborators Dr. M. Hasinoff, C. Virtue, I. Blevis, Dr. J. Lowe, Dr. B. Robertson, Dr. T. Mulera, Dr. A. Shor, and Dr. S. Chew, who helped at one stage or another.

I am particularly grateful to Dr. Jean-Michel Poutissou who has been a constant source of support and encouragement. Without his guidance throughout all aspects of the experiment, analysis and even writing of the thesis, none of this work would have been possible.

I am fortunate that my supervisor Dr. Al Stetz challenged me into undertaking this experiment. I have received a great deal of help from him along the way and important advice at critical moments of the project.

I owe many thanks to Dr. Chris Waltham who has taken some load of my shoulders by analysing part of the experiment. I am deeply grateful to Dr. D. Beder, Dr. L. Roberts, Dr. J. Smith and Dr. G. Tupper for their assistance with the radiative corrections.

I am also indebted to Dr. John Gardner for his advice during my graduate studies in Corvallis and for his support of my application to the Graduate School at OSU. Without it, I would not have been able to come to North America in the first place.

I would like to use this occasion to thank all my friends for their companionship during the years, be it over a beer, kayaking or climbing.

Finally, I would like to dedicate this thesis to my parents who taught me the value of education. They have always stood by me and knowing that makes all the difference to me.

## TABLE OF CONTENTS

<u>Chapter</u>	<u>Page</u>
1. INTRODUCTION	1
1.1 Review of the hadron structure notation	1
1.2 $\pi^0$ decays	5
1.3 Dalitz decay $\pi^0 \rightarrow e^+ e^- \gamma$	8
1.4 $\pi^0$ transition form factor	9
2. HISTORICAL BACKGROUND	11
2.1 Theoretical models	11
2.2 Previous experimental work	14
3. SPECTRUM AND DESIGN	17
3.1 Source of neutral pions	17
3.2 Event acceptance	20
3.3 Strategy for the analysis	22
3.4 Systematic and statistical errors	28
3.5 Normalization	33
4. EXPERIMENTAL DETAILS	34
4.1 Experimental set-up	34
4.2 $\pi^-$ beam	36
4.3 Liquid hydrogen target	38
4.4 Layered scintillator	38
4.5 Wire chamber telescope	39
4.6 Sodium iodide crystals	40
5. EXPERIMENTAL PROCEDURE	42

6.	PRELIMINARY ANALYSIS	48
6.1	Electron positron pair identification by a three scintillator arrangement	48
6.2	Resolution of the wire chamber telescope	50
6.3	Wire chamber efficiencies	52
6.4	NaI response functions	54
6.5	Energy calibration of the NaI crystals	56
6.5.1	In-beam energy calibration	56
6.5.2	$\pi^+ \rightarrow e^+ \nu_e$ energy calibration	56
6.5.3	Energy calibration with neutral events	58
6.5.4	Gain stability	64
6.6	A large NaI spectrometer as a $\pi^0$ monitor	64
7.	MONTE CARLO SIMULATION	67
8.	RADIATIVE CORRECTIONS	73
9.	FINAL EVENT ANALYSIS	79
9.1	Overall normalization	79
9.2	Background from $\pi^-$ pile-up in the target	85
9.3	Event selection	87
10.	RESULTS AND CONCLUSION	101
10.1	$60^\circ$ Geometry	101
10.2	$130^\circ$ Geometry	103
10.2	$156^\circ$ Geometry	105
	BIBLIOGRAPHY	110
	APPENDIX	112

## LIST OF FIGURES

<u>Figure</u>	<u>Page</u>
1.1 Electron-pion scattering	3
1.2 Electron-positron annihilation	3
1.3 Internal conversion decay	7
1.4 $\pi^0$ Dalitz decay	7
2.1 Dalitz decay in the VDM	12
2.2 $\pi^0$ decay in the quark triangle loop model	12
3.1 $E_{\text{pair}}$ vs. $x_{\text{vis}}$ for $\pi^-$ stopped in $\text{LH}_2$ at $156^\circ$	19
3.2 Kroll-Wada distribution	21
3.3 Detection efficiency	23
3.4 Invariant mass spectrum at $156^\circ$	24
3.5 Relative change in Dalitz rate due to the $\pi^0$ form factor	26
3.6 Kroll-Wada distribution for different values of "a"	27
3.7 The sensitivity factor $\Gamma_{\text{SI}}/2\Gamma_{\text{SD}}$	29
3.8 Absolute error in "a" due to energy calibration errors	30
3.9 Allowed phase space (x,y)	31
4.1 Experimental layout at $130^\circ$	35
4.2 Beam telescope	37

5.1 Surface muon edge	44
5.2 Detected $\pi^+ \rightarrow e^+ \nu_e$ spectrum	45
5.3 Absolute acceptance calibration of $\pi^0$ -monitor SOPHIE	47
6.1 TINA layered scintillator response	49
6.2 TINA in-beam energy calibration	57
6.3 Energy loss of electrons in the dead-layers of the NaI	60
6.4 Sketch of the method to determine the projected ADC zero	62
6.5 Variation of TINA energy calibration factor during the run	63
6.6 Ratio between TINA and MINA $\pi^0$ -box centroid position	65
7.1 Correlation between the two delay-line sums for single $e^-$	72
8.1 One photon diagrams	74
8.2 Two photon diagrams	76
9.1 Variation of $N_{\text{det } \pi^0_i} / N_{\text{SOPHIE}_i}$ during the run	81
9.2 $E_{\text{MINA}}$ vs. $E_{\text{TINA}}$ Monte Carlo result at $156^\circ$	88
9.3 Measured stopping distribution in the target (X vs. Z)	90
9.4 The value of "a" at $130^\circ$ for different $E_{\text{min}}$	92
9.5 $E_{\text{TINA}}$ at $130^\circ$ before energy cut is applied	93
9.6 TINA-arm DIFMAX distribution at $156^\circ$	95
9.7 The value of "a" at $156^\circ$ for different CUTMAX	96
9.8 $E_{\text{TINA}}$ at $156^\circ$ after all cuts are applied	98
9.9 The difference (Data - Monte Carlo) of $E_{\text{MINA}}$ vs. $E_{\text{TINA}}$ at $156^\circ$	99
9.10 The invariant mass spectrum at $130^\circ$	100

10.1	The $\pi^-$ stopping distribution in the Z-direction at $130^\circ$	106
10.2	$E_{\text{MINA}}$ vs. $E_{\text{TINA}}$ at $156^\circ$ before any cuts are applied	107
A.1	Kroll-Wada distribution with $\theta_{\text{min}}=100^\circ$ and different $E_{\text{min}}$	114
A.2	Kroll-Wada distribution with $E_{\text{min}}=10\text{MeV}$ and different $\theta_{\text{min}}$	115
A.3	Sketch of the optimized Monte Carlo "rejection" technique	119

## LIST OF TABLES

<u>Table</u>	<u>Page</u>
2.1 Experimental results from the study of the $\pi^0$ form factor in the decay $\pi^0 \rightarrow e^+ e^- \gamma$ .	16

A MEASUREMENT OF THE NEUTRAL PION FORM FACTOR BY  
MEANS OF THE REACTION  $\pi^0 \rightarrow e^+e^-\gamma$

1. INTRODUCTION

In recent years new theoretical advances and improved experimental techniques have fostered a renewed interest in the electromagnetic decays of mesons. Electromagnetic phenomena provide information on the quark configurations in hadronic matter since they reflect the interaction of photons with the electric charges of the quarks. Electromagnetic processes are found to be simpler to calculate and they allow one to make a more complete theoretical interpretation than it is the case for purely hadronic interactions. Consequently, electromagnetic processes constitute a testing ground for any theory describing the structure of strongly interacting particles.

1.1 Review of the hadron structure notation

Understanding the electromagnetic structure of hadrons has been a major pursuit of high energy physics since Hofstadter's electron scattering experiment first revealed the extended charge distribution of the proton [1]. In first Born Approximation, the differential cross-section for the scattering of an electron by a particle with a specific structure can be written in the form:

$$\frac{d\sigma}{dq^2} = \left[ \frac{d\sigma}{dq^2} \right]_{\text{pointlike}} |f(\vec{q}^2)|^2 \quad (1.1)$$

where  $\vec{q}$  is the momentum transfer,  $\vec{q} = \vec{p} - \vec{p}'$ .  $\vec{p}$  and  $\vec{p}'$  are the

momenta of the incident and scattered electron. The function  $f(\vec{q}^2)$  is said to be the form factor of a particle. In the nonrelativistic case the form factor and the charge density distribution are related by a Fourier transformation. In the limit of small momentum transfer, i.e., for  $\vec{q}^2 \ll 1/r$ , where  $r$  is the radius of the particle's electric charge distribution, we find  $f(\vec{q}^2) \approx 1$ . Conversely, if  $\vec{q}^2 \gg 1/r$ , then  $f(\vec{q}^2)$  falls off rapidly and becomes much less than unity. The quantity  $a = \left. \frac{df(\vec{q}^2)}{d(\vec{q}^2)} \right|_{\vec{q}^2=0}$  is usually called the slope of the form factor and is related to  $r$  in the nonrelativistic limit:

$$a = -\frac{1}{6} \langle r^2 \rangle \quad (1.2)$$

In quantum field theory, the process of electromagnetic interaction between particles is described by the exchange of virtual photons. The simplest interaction mechanism is the exchange of one virtual photon (see Figure 1.1). The virtual photon transfers the 4-momentum  $q^2 = (\Delta E)^2 - (\Delta \vec{p})^2$ . In the centre-of-mass reference frame of the colliding particles, the energy of the electron remains unchanged in elastic collisions, and only the direction of the momentum is affected:  $q^2 < 0$ . Such a momentum transfer is said to be space-like.

In the process of electron-positron annihilation (see Figure 1.2) the virtual photon transfers energy but does not transfer momentum. Thus,  $q^2 > 0$  and such photons are said to be time-like. The electromagnetic structure of the  $\pi$  mesons changes the cross-section into:

$$\sigma(e^+e^- \rightarrow \pi^+\pi^-) = [\sigma(e^+e^- \rightarrow \pi^+\pi^-)] \Big|_{\text{pointlike}} |f_\pi(q^2)|^2 \quad (1.3)$$

Consequently, annihilation experiments offer another way to study the form factor of the pion,  $|f_\pi(q^2)|$ , but now in the range of time-like 4-momentum transfer.

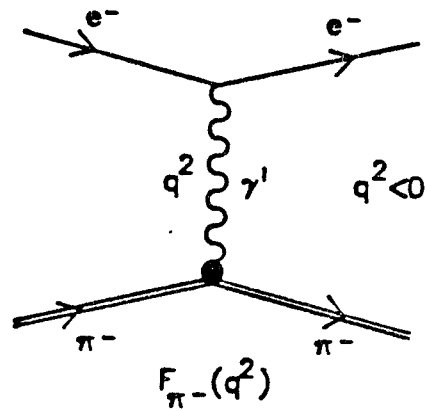


Figure 1.1 Electron-pion scattering

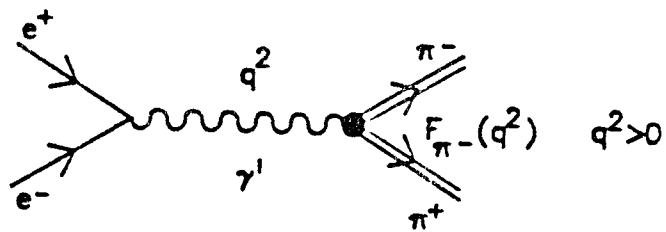


Figure 1.2 Electron-positron annihilation

When the 4-momentum squared, approaches the squared mass of a vector meson  $V$  with quantum numbers equal to those of the photon (spin 1 and negative parity:  $J^P=1^-$ ), the virtual photon materializes and then decays through the channel  $V \rightarrow \pi^+\pi^-$ . This realization of an intermediate particle results in a strong resonance enhancement of the form factor of a  $\pi^\pm$  meson. Another name for this effect is vector-meson dominance (VMD).

So far we have discussed the phenomena stemming from the structure of "charged" particles. "Neutral" particles, with no "charges" such as electric charge, baryon number, strangeness, etc., are identical to their antiparticles. The group of truly "neutral" particles includes the photon and some mesons, e.g., the  $\pi^0$ ,  $\eta$ ,  $\eta'$ ,  $\rho^0$ ,  $\omega$ , and  $\phi$  mesons. These particles are eigenstates of an additional symmetry called charge-conjugation invariance, with the photon having a sign-reversed eigenvalue from that of the  $\pi^0$ ,  $\eta$  and  $\eta'$ .

The process of single-photon exchange (of the type shown in Figure 1.1) are forbidden for "neutral" mesons  $M^0$  owing to the conservation of charge-conjugation invariance in electromagnetic interactions. Since the amplitudes of such single-photon processes are proportional to the electromagnetic form factors of neutral mesons,  $|f_{M^0}(q^2)|$ , these electromagnetic form factors are always equal to zero.

However, the complex internal structure of neutral mesons can manifest itself in electromagnetic radiative decays of the form:

$$A \rightarrow B + \gamma \quad (1.4)$$

where  $A$  and  $B$  are neutral mesons with opposite charge-conjugation quantum numbers. If the radiative decay (1.4) is allowed, another process is also possible in which the  $\gamma$ -quantum is virtual, and then turns into a lepton pair:

$$A \rightarrow B + l^+ + l^- \quad (1.5)$$

This effect is called internal conversion (see Figure 1.3).

The probability of formation of a lepton pair with an effective mass  $m_{l^+l^-}$  in an internal conversion decay (1.5) is proportional to the probability of emitting a virtual photon with time-like 4-momentum  $q^2 = m_{l^+l^-}^2 = (E_{l^+} + E_{l^-})^2 - (\vec{p}_{l^+} + \vec{p}_{l^-})^2$ .

However, the probability of emission of this photon is caused by the dynamic electromagnetic structure arising at the "vertex" of the transition  $A \rightarrow B$  which is characterized by a specific form factor called the transition form factor. The ordinary "static" form factors of "neutral" mesons thus vanish, but transition "dynamic" form factors may appear.

One example of these transitions is the decay

$$A \rightarrow \gamma + l^+ + l^- \quad (1.6)$$

which corresponds to the internal conversion of a photon in the decay  $A \rightarrow \gamma\gamma$  which is allowed, e.g., for "neutral" pseudoscalar mesons  $M^0$ . In this case the transition form factor describes the electromagnetic structure of the "vertex"  $A \rightarrow \gamma\gamma$  which incorporates only the decaying meson.

## 1.2 $\pi^0$ decays

The rare electromagnetic decay  $\pi^0 \rightarrow e^+ + e^- + \gamma$ , is of interest because it may reveal information about the structure arising at the "vertex"  $\pi^0 \rightarrow \gamma\gamma$ . This decay is especially suited for experimental research since high fluxes of  $\pi^0$ 's can be obtained at "meson-factories". The  $\pi^0$  meson, being the lightest of the known hadrons is stable vis a vis strong interactions and decays only

<sup>1</sup> A pseudoscalar particle has spin 0 and negative intrinsic parity.

through electromagnetic processes:<sup>2</sup>

<u>Decay</u>	<u>Branching ratio</u>	
$\pi^0 \rightarrow \gamma \gamma$	$98.787\% \pm 0.030\%$	(1.7)
$\pi^0 \rightarrow e^+ e^- \gamma$	$1.160\% \pm 0.047\%$	(1.8)
$\pi^0 \rightarrow e^+ e^- e^+ e^-$	$3.28 \cdot 10^{-5}$	(1.9)
$\pi^0 \rightarrow e^+ e^-$	$(1.8 \pm 0.6) 10^{-7}$	(1.10)

In 1951 Dalitz [3] first noted the existence of the internal conversion reaction (1.8), interpreting it as the production of one real and one virtual photon in reaction (1.7). The virtual photon then decays into an electron positron pair (see Figure 1.4). Similarly, reaction (1.9) may be described as double internal pair production with two virtual photons in reaction (1.7). The two photon decay (1.7) implies that the  $\pi^0$  has a charge conjugation eigenvalue of +1. It was pointed out by Yang [4], through parity and angular momentum arguments, that the relative plane of polarization of the two photons determines whether the  $\pi^0$  is a scalar or pseudoscalar particle. Observing this polarization by means of the double Dalitz decay (1.9), Plano et.al. [5] demonstrated that the  $\pi^0$  has negative intrinsic parity.

The main branch (1.7) establishes quantum numbers for the neutral pion as well as its coupling constant to the electromagnetic field. However, this decay cannot serve further in the investigation of the  $\pi^0$  quark structure since energy and momentum conservation require a unique two-body final state. The Dalitz decay (1.8), on the other hand, has final states with a finite range of particle momenta. They can be used as probes to study the details of the interaction, specifically the strong interaction effects at the  $\pi^0 \rightarrow \gamma\gamma$  "vertex" when one  $\gamma$  is "off-mass shell".

<sup>2</sup> with a lifetime of  $0.828 \cdot 10^{-16}$  s.

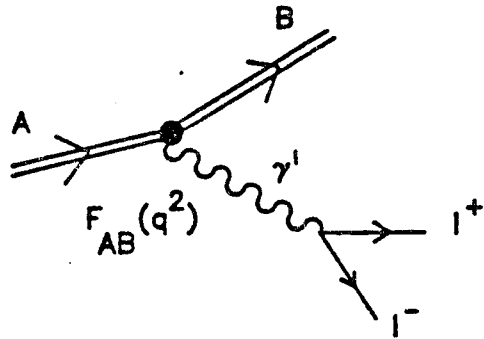


Figure 1.3 Internal conversion decay

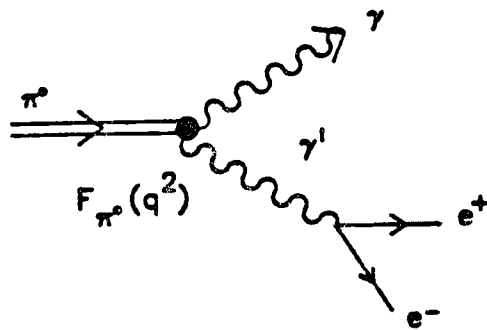


Figure 1.4  $\pi^0$  Dalitz decay

### 1.3 Dalitz decay $\pi^0 \rightarrow e^+ e^- \gamma$

To lowest order in the fine structure constant  $\alpha$ , the conversion decay amplitude of a pseudoscalar meson has the Lorentz invariant form:

$$M = 8\pi\alpha i \left[ f_{\pi^0}(q^2) G^{\alpha\beta\gamma\delta} k_{1\alpha} k_{2\beta} \varepsilon_{\gamma} \right] \frac{1}{q^2} \left[ \bar{u} \gamma_{\delta} u \right] \quad (1.11)$$

Here, and in what follows,  $f_{\pi^0}(q^2)$  is the form factor of the  $\pi^0 \rightarrow \gamma\gamma$  transition, a Lorentz scalar;  $k_{2\beta}$  is the 4-momentum of the virtual photon;  $q^2 = m_e^2 + e^-$  is the effective mass squared of the leptonic pair;  $k_{1\alpha}$  is the 4-momentum of the real photon and  $\varepsilon_{\gamma}$  its polarization 4-vector;  $G^{\alpha\beta\gamma\delta}$  is the totally antisymmetric unit tensor, so that  $G^{\alpha\beta\gamma\delta} p_{\alpha} q_{\beta} \varepsilon_{\gamma}$  is the simplest pseudoscalar that can be formed from the electromagnetic fields of the two photons;  $u$  and  $\bar{u}$  are Dirac spinors and the  $\gamma_{\delta}$  are the 4x4 Dirac matrices;  $m_{\pi^0}$  is the pion mass; and  $m_e$  is the electron mass. From this amplitude, Kroll and Wada [6] derived the effective mass spectrum of the lepton pair in the decay (1.8) to lowest order in the fine structure constant  $\alpha$ . Their differential decay rate, normalized to the total  $\pi^0$  width, as a function of the non-trivial parameters of the decay  $x$  and  $y$ , is given by the well-known distribution:

$$\frac{d}{dx dy} \left[ \frac{\Gamma(\pi^0 \rightarrow e^+ e^- \gamma)}{\Gamma(\pi^0 \rightarrow \gamma \gamma)} \right]_{K+W} = \frac{\alpha}{4\pi} \frac{(1-x)^3}{x} \left[ 1 + y^2 + \frac{r}{x} \right] |F_{\pi^0}(x)|^2 \quad (1.12)$$

$$\text{or } \frac{d}{dx} \left[ \frac{\Gamma(\pi^0 \rightarrow e^+ e^- \gamma)}{\Gamma(\pi^0 \rightarrow \gamma \gamma)} \right]_{K+W} = \frac{\alpha}{3\pi} \frac{1}{x} (1-x)^3 \left( 2 + \frac{r}{x} \right) \left( 1 - \frac{r}{x} \right)^{1/2} |F_{\pi^0}(x)|^2$$

where

$$F_{\pi^0}(x) = \frac{f_{\pi^0}(x)}{f_{\pi^0}(0)} \quad ; \quad r = \left( 4 m_e^2 \right) / \left( m_{\pi^0}^2 \right) \quad (1.13)$$

and the normalization is such that

$$F_{\pi^0}(0) = 1 \quad (1.14)$$

The crucial variable of the decay is  $x$ , the square of the invariant mass of the leptonic pair in units of the  $\pi^0$  mass squared:

$$x = q^2 / m_{\pi^0}^2 \quad (1.15)$$

$y$  is the energy partition of the electron and positron:

$$y = (E_{e^+} + E_{e^-}) / |\vec{p}_{e^+} + \vec{p}_{e^-}| \quad (1.16)$$

For the reaction  $\pi^0 \rightarrow e^+e^-\gamma$ :

$$x \in (r, 1) \quad y \in (-\eta, \eta) \quad (1.17)$$

where  $\eta = (1 - r/x)^{1/2}$

#### 1.4 $\pi^0$ transition form factor

It is possible to determine the electromagnetic transition form factor  $F_{\pi^0}(x)$  from experimental data on the  $\pi^0$  Dalitz decay invariant mass spectrum, once the quantum electrodynamic (QED) multipliers in eq. (1.12) have been singled out. The form factor modifies the shape of the electron positron pair spectrum as derived for a point particle. The effect of the  $\pi^0$  structure can also be seen by looking at the partial rate of events corresponding to large invariant mass pairs (see chapter 3). In contrast, the total integrated rate is very insensitive to the structure effect. This has recently been verified at LAMPF [7], where the decay rate was found to be  $R_{e^+e^-\gamma}(\text{exp.}) = (1.160 \pm 0.047) * 10^{-2}$  compared to  $R_{e^+e^-\gamma}(\text{theo}) = 1.19 * 10^{-2}$ , in good agreement with the Dalitz prediction for a point particle.

Assuming  $F_{\pi^0}(q^2)$  to be a slowly varying function in the range of momentum transfers accessible by the Dalitz decay (1.8) ( $q^2 \leq m_{\pi^0}^2$ ), we may write the form factor in the form:

$$|F_{\pi^0}(x)|^2 \approx (1 + [dF_{\pi^0}(x)/dx]_{x=0} * x)^2 \approx 1 + 2ax \quad (1.18)$$

In this linear approximation, the test of a theory is its prediction of a single parameter, the form factor slope "a". The next chapter outlines a number of theoretical models of the  $\pi^0$  form factor and points out the theoretical discrepancy with hitherto existing experiments.

## 2. HISTORICAL BACKGROUND

### 2.1 Theoretical models

The  $\pi^0$  form factor  $F_{\pi^0}(x)$  depends on the intermediate states contributing to the  $\pi^0 \rightarrow \gamma\gamma$  vertex. To estimate the order of magnitude and the sign of the expected effect, one may use the vector dominance model (VDM) which has its origin in dispersion relations [8-15]. According to the VDM, the photon interactions with hadrons proceed through virtual vector mesons (see Figure 2.1) and the  $\pi^0$  form factor is calculated with a dispersion relation where the spectral function is constructed from single vector intermediate states. In the simplest form of this calculation an unsubtracted dispersion relation is used, and the intermediate state is assumed to be dominated by the  $\rho$ -meson. This leads to a unique prediction for the slope parameter:

$$a \approx m_{\pi^0}^2 / m_{\rho}^2 = + 0.032 \quad (2.1)$$

and provides justification for the linear expansion in (1.18). As the VDM evolved, a once-subtracted dispersion relation was used to calculate the slope of the form factor. In this approach one obtains many ambiguous solutions for "a", since the relative sign of the contributions from the different vector mesons cannot be determined.

In a classic paper by Adler [23], the  $\pi^0$  decay width was calculated from the single quark triangle diagram in Figure 2.2. The result is in excellent agreement with experiment, if it is assumed that the fundamental fermions (quarks) of the strong interaction come in three colored species. This is one of the cornerstones for the belief in SU(3) as an internal symmetry group for the strong

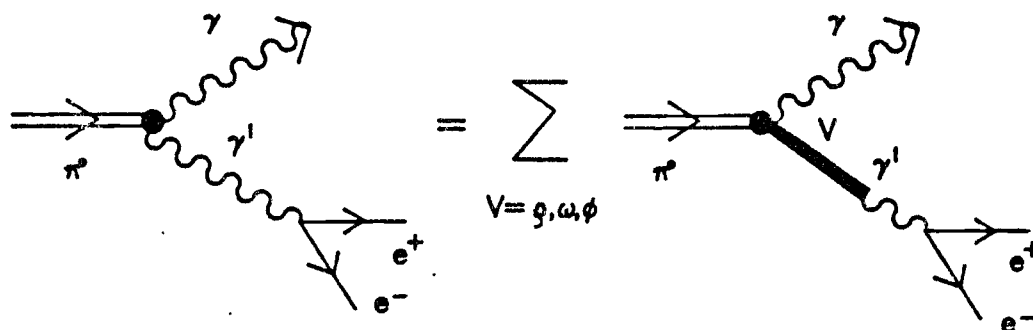


Figure 2.1 Dalitz decay in the VDM

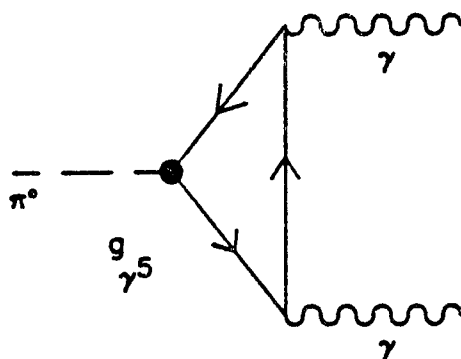


Figure 2.2  $\pi^0$  decay in the quark triangle loop model

interaction. It is therefore of interest to consider dynamical models for the transition form factors by extending this successful theory to treat the "off-mass shell"  $\pi^0 \rightarrow \gamma\gamma$  vertex. This is usually done by either an exact relativistic quark loop calculation or by the hard pion techniques of Weinberg and Schnitzer [24,25] with the inclusion of anomalous terms. The decay of pseudoscalar mesons, including the radiative decays  $\pi^0 \rightarrow \gamma\gamma$  and  $\pi^0 \rightarrow e^+e^-\gamma$ , have been discussed in reference [26] under the assumption that the amplitude of these processes are dominated by quark triangle anomalies. The authors of [26] come to the conclusion that VDM must hold well in the decay  $\pi^0 \rightarrow e^+e^-\gamma$ .

At this point, it should be noted that the simple VDM need not always be sufficient for a quantitative description of physical processes. There are known situation involving large momentum transfers where the model breaks down. A careful analysis on the validity of the VDM for the decay  $\pi^0 \rightarrow e^+e^-\gamma$  is therefore necessary. This has recently been done in the framework of QCD by the authors of reference [27]. They conclude that the correction to the simple VDM result does not exceed 5-10%.

Another approach based on the concept of  $Q^2$ -duality was developed in references [28-31]. This  $Q^2$ -duality establishes the equivalence between the VDM and the quark triangle loop model. In the quark triangle loop model with a phenomenologically fitted coupling  $g\gamma^5$  of the pseudoscalar meson to the constituent quarks (see Figure 2.2), the transition form factor is given in the "soft meson" limit, i.e., for  $m_\pi \rightarrow 0$ ,  $q^2 \neq 0$  by [17]:

$$F_{\pi^0}(x) \Big|_{\text{soft}} = \left\{ \sum_q \frac{4m_q}{2q} \frac{g_{\pi^0 qq} - Q_q^2}{m_q} \arcsin\left(\frac{(m_\pi^2 - x)}{2m_q}\right)^{1/2} \right\} / \left\{ \sum_q \frac{g_{\pi^0 qq} - Q_q^2}{m_q} \right\} \quad (2.2)$$

where  $m_\pi$  is the  $\pi^0$  mass;  $m_q$  is the quark mass;  $g_{\pi^0 qq}$  are the meson quark loop couplings;  $Q_q$  is the quark charge and the sum is performed over a superposition of quark loops with different "flavors". The result for the  $\pi^0$ -meson is found to be only weakly

dependent on the assumptions made in the "soft meson" approximation and produces the VDM result for constituent quark masses of around 225MeV.  $Q^2$ -duality cannot be expected to give an exact quantitative description of the form factor because of the approximations made in the theory. Unfortunately, more consistent QCD calculations are not possible for the range of momentum transfers typical for  $\pi^0 \rightarrow e^+e^-\gamma$  ( $q^2 < m_{\pi^0}^2$ ). An asymptotic QCD extrapolation from sufficiently larger  $q^2$ , where perturbative QCD calculations are practical, was carried out in reference [32]. Their analysis shows that the asymptotic behavior of the transition form factor obtained from QCD predictions at high  $q^2$ , smoothly matches the predictions of the VDM in the region of low momentum transfers.

In summary, all theoretical predictions in the framework of present models of the strong interaction converge on the value +0.03 for the  $\pi^0$  transition form factor slope. An experimental value significantly different from that would require calculations in the realm of yet unknown and new physics.

## 2.2 Previous experimental work

Over the last 25 years, experiments on the  $\pi^0$  transition form factor were carried out sporadically at various laboratories. The experimental development is summarized in Table 2.1. The original liquid hydrogen bubble chambers were replaced by magnetic spectrometers in the more recent experiments, while the sole NaI spectrometer experiment of S. Devons et.al. [20] was never repeated. It suffered from no obvious technical difficulties but was quite limited by statistics and can nowadays be improved by the use of modern delay-line wire chambers which are far superior to the optical spark chambers used in the old experiment.

A quantitative analysis shows that, while the form factor of the  $\eta$  meson agrees well with VDM predictions [21], a considerable deviation from this model is found in the result of the most recent measurement of the  $\pi^0$  form factor [22]. However, no thorough investigation of systematical errors was conducted for any of the

previous  $\pi^0$  experiments, and J. Fischer et.al. [22] is the only collaboration who included radiative corrections from second order Feynman diagrams (see chapter 8) in their analysis. The sensitivity of their experiment to these corrections was large and increased the result by a factor of two, thus bringing it into contradiction with theory. This experimental situation provided the motivation for the present experiment.

Table 2.1 Experimental results from the study of the  $\pi^0$  form factor in the decay  $\pi^0 \rightarrow e^+e^-\gamma$ .

<u>Experiment</u>	<u>Ref.</u>	<u>Date</u>	<u>Result</u>	<u>Technique</u>
H. Kobrak et.al.	[19]	1961	$a = -0.15 \pm 0.1^a$	Liquid hydrogen bubble chamber
P. Samios et.al.	[18]	1961	$a = -0.24 \pm 0.16$	Liquid hydrogen bubble chamber
S. Devons et.al.	[20]	1969	$a = 0.01 \pm 0.11$	Optical spark chambers and NaI spectrometers
J. Burger et.al.	[2]	1972	$a = 0.02 \pm 0.1$	Magn. spectrometer
J. Fischer et al.	[22]	1978	$a = 0.1 \pm 0.03^b$	Magn. spectrometer Electrons are identified by gas Cerenkov counters. $K^+ \rightarrow \pi^+ \pi^0$ decay in flight is the source of tagged $\pi^0$ .

a Errors are statistical only. Radiative corrections have not been included

b Errors are statistical only and come from 21000  $\pi^0 \rightarrow e^+e^-\gamma$  events in the region  $0.3 < x < 0.9$ . Radiative corrections have been included. They increase the slope "a" by a factor of two.

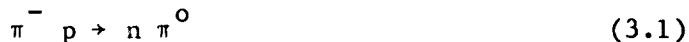
### 3. SPECTRUM AND DESIGN

Estimates made in the framework of the VDM show that in internal conversion decays (1.5), the form factor influence on the effective mass spectrum of the lepton pair becomes greater the larger the mass of the decaying meson A. For the Dalitz decay (1.8), the form factor does not change the partial decay rate by more than 6% even for the highest admissible value of  $X=1$ . For this reason, the study of the  $\pi^0$  transition form factor is a particularly complicated problem which requires enormous statistics. If the decay leptons are  $e^+e^-$  as in (1.8), an important role is also played by radiative corrections of higher order Feynman diagrams which are proportional to  $\ln((m_{\pi^0})^2/(m_e)^2 * X)^2$ . The situation is further complicated by external conversion of photons from (1.7) in the set-up material.

Although the branching ratio for the observation of (1.8) is relatively large, most of the contribution occurs in the low invariant mass region which, in view of eq. (1.18), is insensitive to the form factor slope. Thus, studying the  $\pi^0$  transition form factor is very difficult from the experimental point of view, requiring enormous statistics, an experimental design which optimizes the sensitivity to "a" and a precise knowledge of systematic errors including all conventional, uninteresting background processes.

#### 3.1 Source of neutral pions

To obtain sufficient statistics in a reasonable time scale, an abundant source of neutral pions had to be found. Present meson factories provide intense beams of  $\pi^-$  mesons, which when moderated and brought to rest in a liquid hydrogen target produce neutral pions through the reaction:



This charge exchange at rest is the most copious production method for  $\pi^0$ 's. It results in an isotropic flux of 3.4MeV  $\pi^0$ 's with a velocity  $\beta = 0.20$ .

Two other dominant reactions take place when a  $\pi^-$  at rest is captured by a proton:



For a  $\pi^-$  at rest, the relative rate into the strong and electromagnetic channels is given by the Panofsky ratio [33]:

$$P = \frac{\Gamma(\pi^- p \rightarrow n \pi^0)}{\Gamma(\pi^- p \rightarrow n \gamma) + \Gamma(\pi^- p \rightarrow n e^+ e^-)} = 1.546 \pm 0.009 \quad (3.4)$$

Thus,  $\pi^0$ 's are produced from about 60% of a stopped  $\pi^-$  beam in hydrogen.

One problem associated with this method of  $\pi^0$  production is the high internal conversion background (3.3), which is 0.7% of the electromagnetic channel. Due to the finite resolution of any physical detector, Dalitz decay pairs and internal conversion pairs occupy kinematic regions which overlap at large values of the invariant mass  $x$  (see Figure 3.1). It is therefore difficult to separate the two channels, and only a careful Monte Carlo simulation of the  $\pi^- p \rightarrow e^+ e^- n$  events can give information on their contribution to the final spectrum.

It is possible to reduce the internal conversion background by choosing different methods of  $\pi^0$  production. Charge exchange at the  $\Delta$  resonance was used in the recent LAMPF experiment [7], but there the  $\pi^0$  production is lower by a factor of 20. The Kaon-decay:



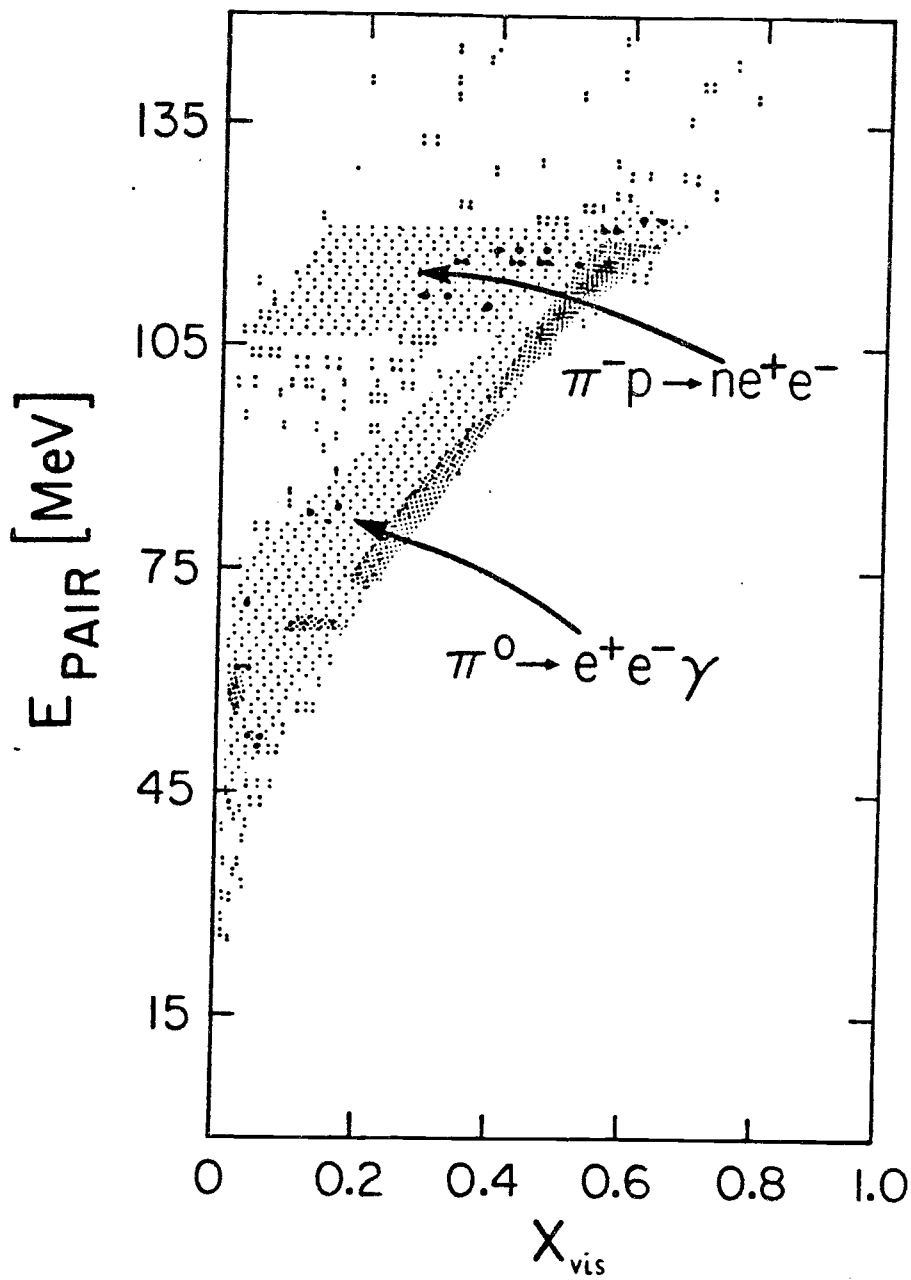


Figure 3.1  $E_{\text{pair}}$  vs.  $x_{\text{vis}}$  for  $\pi^-$  stopped in  $\text{LH}_2$  at  $156^\circ$ .

can be used to obtain a tagged  $\pi^0$  beam [22]. Here again, the  $\pi^0$  production rate is low. In the CERN experiment [22] for instance, it was down by a factor of 300.

### 3.2 Event acceptance

The differential decay rate as given by the Kroll-Wada distribution (1.12) is plotted in Figure 3.2. It reaches a maximum at  $x \approx 10^{-4}$  and then falls many decades in a narrow region of  $x$ . That this behavior is associated with small opening angle pairs, can be seen by rewriting equation (1.15) for the invariant mass  $x$ , as a function of lepton energies and pair opening angle  $\theta_{e^+e^-}$ .

$$x \cong (1/m_\pi^2) [2E_{e^+}E_{e^-}(1 - \cos \theta_{e^+e^-})] \quad (3.6)$$

Consequently, both an angle and an energy measurement of the leptons is required in order to establish the invariant mass spectrum of the Dalitz pair.

Determining "a" from the slope, or the total integrated rate of the curve in Figure 3.2 would place impossible demands on the experimental resolution. Thus, it is imperative to configure the experiment so that it is only sensitive to large opening angle pairs. To realize this, two large NaI crystals (TINA and MINA), each with a finite solid angle, were mounted on a scattering table so that the angle between them could be changed continuously from  $60.5^\circ$  to  $180^\circ$ . NaI scintillation counters were the natural choice for the energy measurement of the decay particles, since they were readily available at TRIUMF and possess an energy resolution which is adequate for the experiment. Incidentally, it is also clear, that for a  $\pi^0$  form factor measurement with a  $4\pi$  detector like a TPC or SINDRUM, a trigger condition has to be employed which restricts the acceptance to larger opening angle pairs.

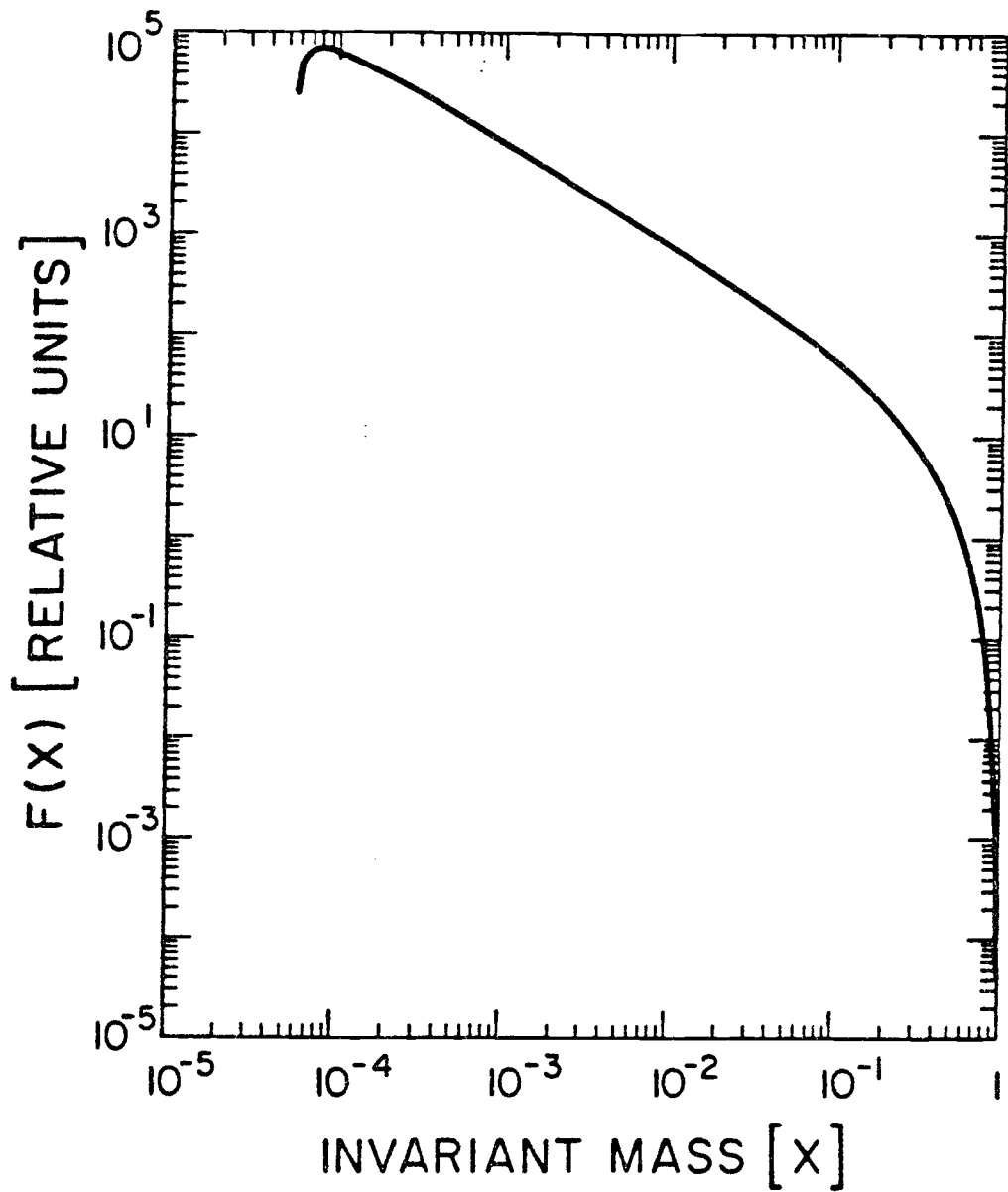


Figure 3.2 Kroll-Wada distribution

### 3.3 Strategy for the analysis

The experiment has to rely entirely on a Monte Carlo study of the event acceptance for both Dalitz events and the various backgrounds. However, this acceptance depends strongly on the relative opening angle of the detectors. It was therefore important to have a redundant check on the Monte Carlo by measuring at more than one opening angle. We performed an "a"-independent, small angle measurement ( $60.5^\circ$ ) and an "a"-dependent, large angle measurement ( $156^\circ$ ). In addition, a measurement was taken at an intermediate angle ( $130^\circ$ ). The detection efficiency as a function of  $x$  is shown in Figure 3.3 for three different NaI spectrometer configurations. We see, that the efficiency maximum shifts to higher  $x$ -values for larger angles subtended by TINA and MINA and that the acceptance varies very little over a wide range of  $x$ , once the opening angle is  $150^\circ$ . How this restricted acceptance changes the invariant mass distribution, can be seen by comparing the spectrum in Figure 3.4 for detected events at  $156^\circ$  with the Kroll-Wada distribution of a  $4\pi$  detector in Figure 3.2. We see immediately that a large opening angle configuration eliminates the huge number of low-mass pairs, which would otherwise swamp the apparatus. Since the NaI spectrometers are also sensitive to neutrals, the detected invariant mass,  $x_{vis}$ , can be different from the invariant mass of the pair  $x$ . This happens when the coincident photon is picked up by one of the detectors. Thus, the  $x_{vis}$  distribution shows an additional diminution of events near low  $X_{vis}$  together with an accumulation of events near  $X_{vis} = 1$ , i.e., events are shifted toward  $X_{vis} = 1$ . This effect disappears when the NaI detectors subtend a smaller angle, since it becomes kinematically impossible to produce events with  $X_{vis} = 1$ . In view of the factor  $(1+2ax)$  in the invariant mass distribution of the pair (see equation 1.12 and 1.18), one expects the larger  $x$ -region to be more sensitive to the hadronic structure of the  $\pi^0$ . This is shown in Figure 3.5, where the relative change of rate for different values of the form factor slope "a" is plotted

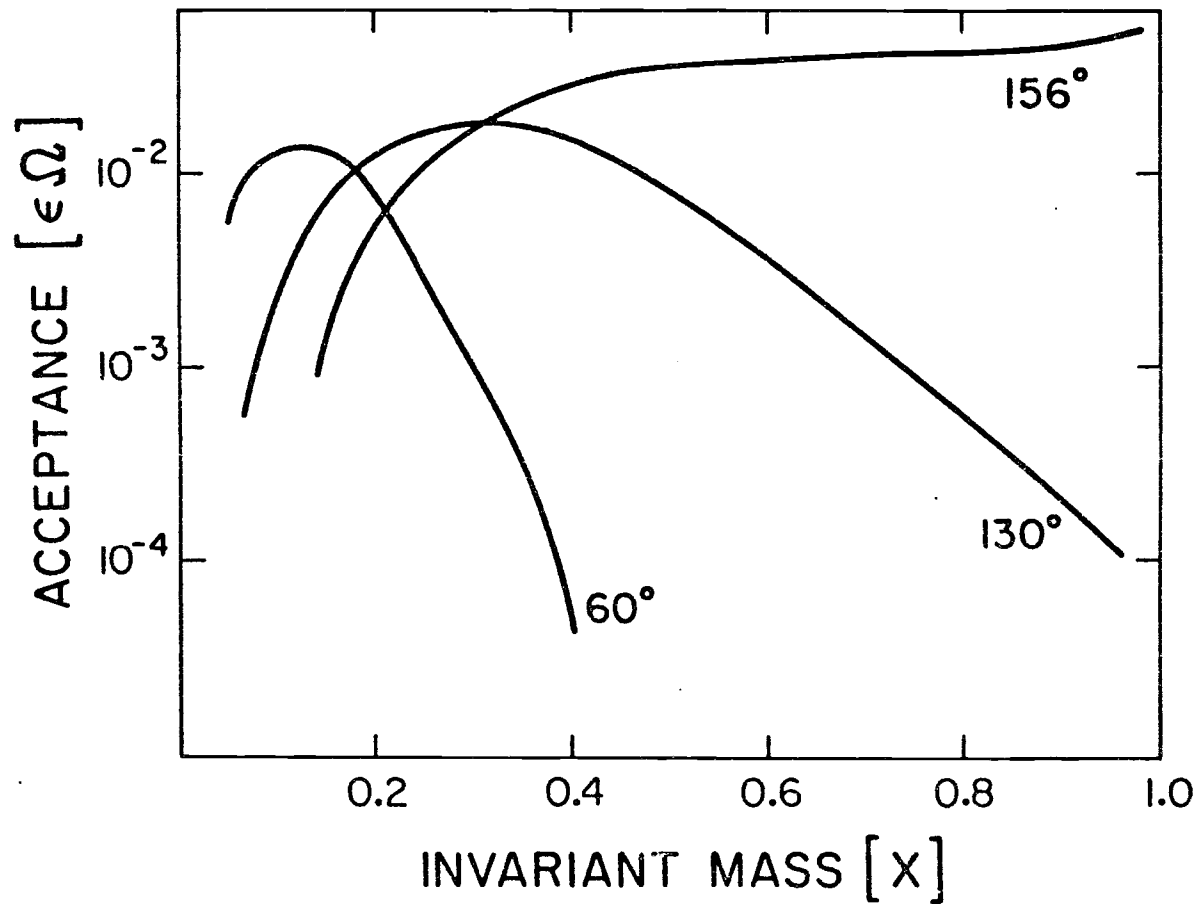


Figure 3.3 Detection efficiency for Dalitz pairs of TINA/MINA at  $60^\circ$ ,  $130^\circ$  and  $156^\circ$ .

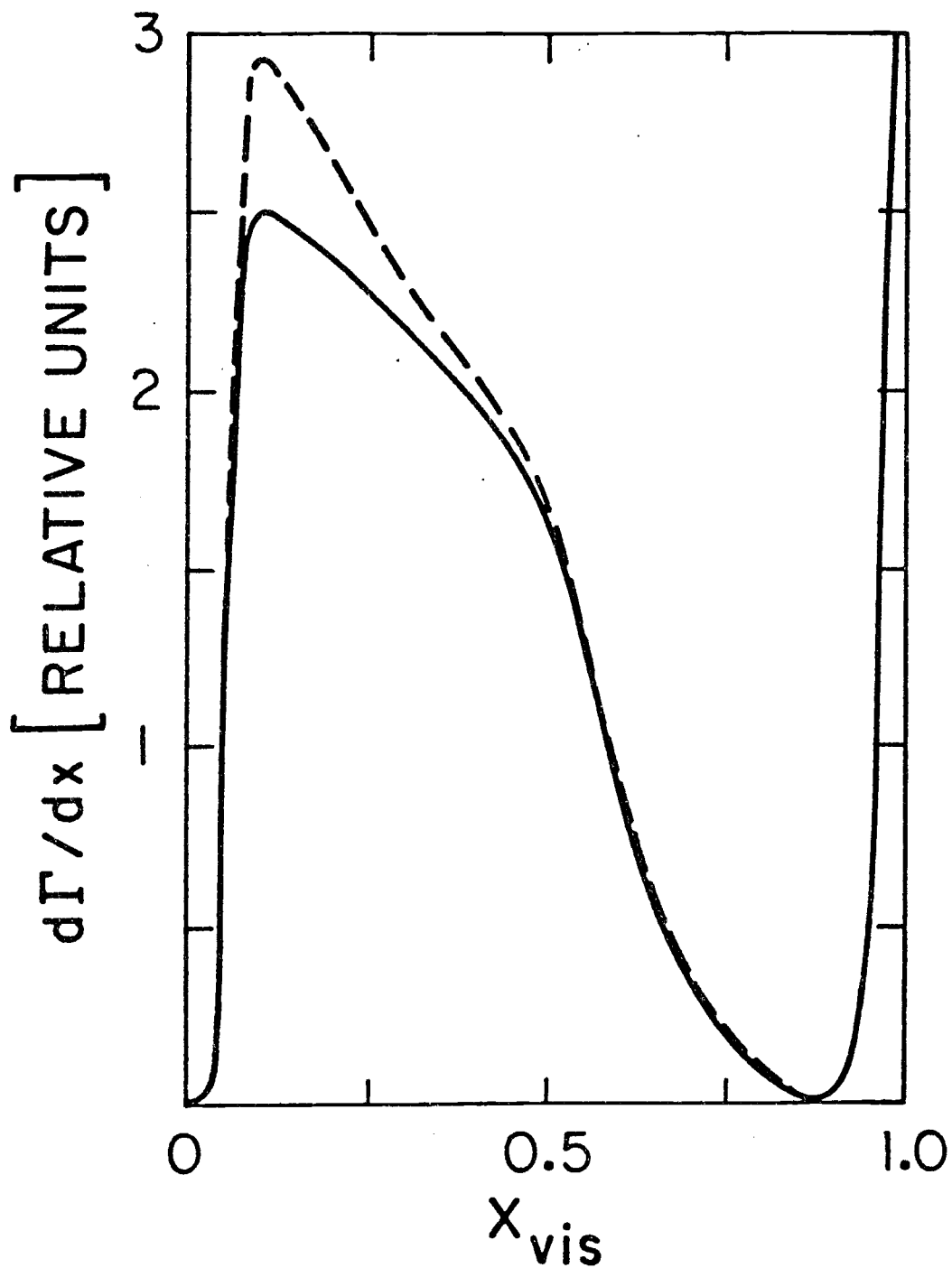


Figure 3.4 Detected invariant mass spectrum for Dalitz pairs at  $156^\circ$  (solid line). The dashed line is the invariant mass distribution of the lepton pairs if the apparatus was insensitive to the photons in  $\pi^0 + e^+e^-\gamma$ .

against the lower edge of an  $x$  interval with  $\Delta x = 0.4$ . These curves were produced for  $\pi^0$ 's decaying at rest and an idealized  $4\pi$  detector with a flat acceptance for events with an opening angle  $\Theta_{e^+e^-}$  larger than a specified minimum  $\Theta_{\min}$ .

For reasonable assumptions on the resolutions of the detectors and on the accuracy with which the energy scale can be established, a Monte Carlo study which determined "a" from a two parameter fit to the shape of the invariant mass distribution showed, that it is impossible by this method to determine the slope parameter to a desired accuracy of 0.02. To appreciate this difficulty one should observe that there is only a slight change in shape between curves in Figure 3.6 for different values of "a". It is apparent, that a small shift in energy calibration can easily confuse the different distributions, making a determination of "a" based on this analysis very difficult.

Fortunately, there is a way out of this problem: Rather than concentrating on the shape of the distribution, one can analyse the change in decay rate due to the slope parameter. The total integrated rate is rather insensitive to "a". The sensitivity is however greatly improved if one measures the decay rate in a restricted region of larger  $x$ . This can be accomplished by either a cut on minimum energy of the electrons/positrons in a wide opening angle geometry or by simply applying a cut on  $x$  (see also Figure 3.5). The form factor slope is then determined by:

$$a = \frac{\Gamma_m(x_{\text{cut}}) - \Gamma_{\text{SI}}(x_{\text{cut}})}{2 \Gamma_{\text{SD}}(x_{\text{cut}})} \quad \text{where} \quad \begin{aligned} \Gamma_{\text{SI}} &= \int (d\Gamma/dx)_{\text{K+W}} dx \\ \Gamma_{\text{SD}} &= \int (d\Gamma/dx)_{\text{K+W}}^* x dx \end{aligned} \quad (3.8)$$

and where  $\Gamma_m$  is the experimental number of Dalitz events detected with an invariant mass of the electron pair  $x$  larger than  $x_{\text{cut}}$ .  $d\Gamma/dx|_{\text{K+W}}$  is the expression given in A.2.  $\Gamma_{\text{SI}}$  and  $\Gamma_{\text{SD}}$  are the theoretical rates corrected for experimental acceptance and all resolution effects. Both measured and theoretical rates are

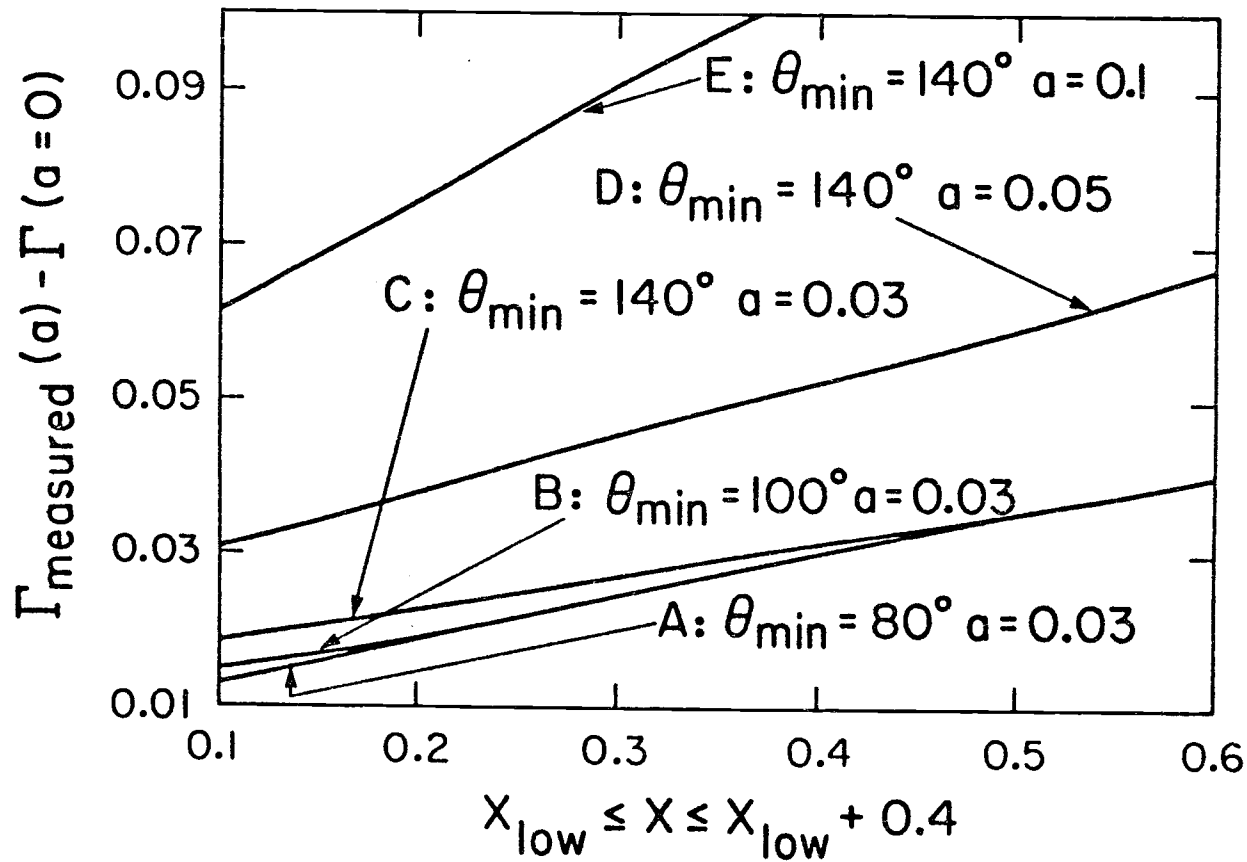


Figure 3.5 Relative change in rate due to the  $\pi^0$  form factor in a region  $x_{\text{low}} < x < x_{\text{low}} + 0.4$  for an idealized detector with efficiency  $\equiv 1$  for pair opening angles  $\theta > \theta_{\text{min}}$  and zero otherwise.

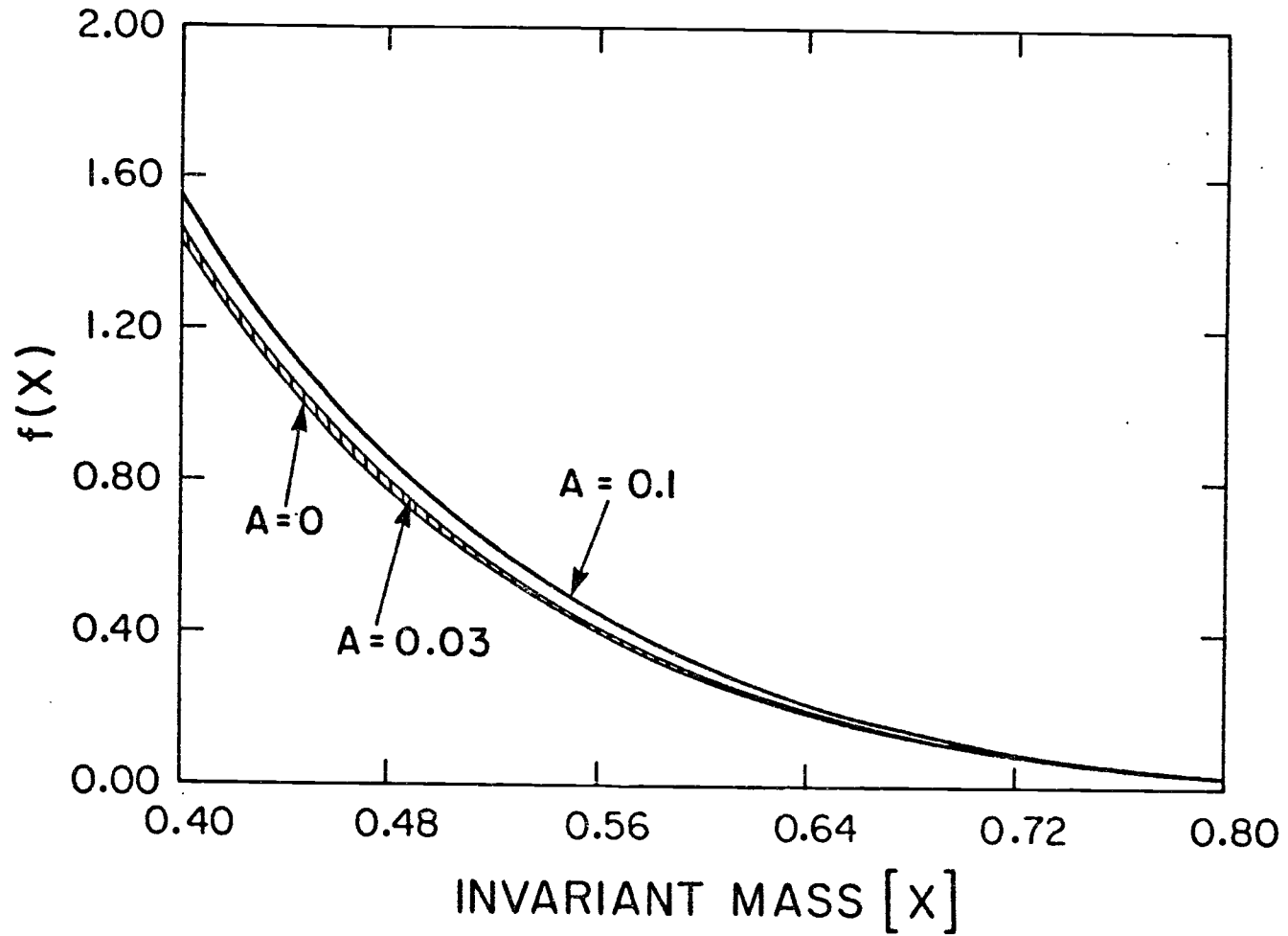


Figure 3.6 Kroll-Wada distribution for different values of the form factor slope.

normalized relative to the number of  $\pi^0$  in the target. The distributions  $\Gamma_{SI}$  and  $\Gamma_{SD}$  can only be obtained by the Monte Carlo method and make a thorough Monte Carlo simulation of the experiment indispensable.

### 3.4 Systematic and statistical errors

To eliminate background processes from the data sample, one has to apply a cut in energy and/or  $x$ . This introduces a systematic error in "a" due to an error in energy scale which is given by:

$$\Delta a = \left( \frac{\Gamma_{SI}(x_{cut})}{2 \Gamma_{SD}(x_{cut})} \right) \frac{\Delta \Gamma(x_{cut})}{\Gamma(x_{cut})} \quad (3.9)$$

if we assume that there are no errors in  $\Gamma_{SI}$  and  $\Gamma_{SD}$ .<sup>3</sup> Here,  $\Delta \Gamma$  is the change in the branching ratio due to a shift  $\Delta E$  at the cut-off energy. To understand the energy problem it is sufficient to study a simple model which can be calculated analytically. In this model the  $\pi^0$  decays at rest and the acceptance of the apparatus is flat for  $\theta_{e^+e^-} > \theta_{min}$  and  $E > E_{min}$  and zero elsewhere. The sensitivity factor  $\Gamma_{SI} / 2\Gamma_{SD}$  obtained in this model is plotted in Figure 3.7. Now suppose the detectors are in error by an amount  $\Delta E$ , i.e., the measured energy is too large by an additive constant  $\Delta E$ . This is equivalent to changing  $E_{min} \rightarrow E_{min} - \Delta E$  and  $x_{cut} \rightarrow x_{cut} - \Delta E / (m_{\pi^0}/4)$ . For  $\Delta E = +0.2 \text{ MeV}$ , the resulting error in "a", as a function of  $x_{cut}$  behaves as shown in Figure 3.8, for various combinations of  $\theta_{min}$  and  $E_{min}$ . The behavior of these curves can be understood with the help of Figure 3.9. The region of allowed values of the integration variable  $x$  and  $y$ , for given  $\theta_{min}$  and  $E_{min}$  lies to the right of the corresponding solid lines. A change in energy scale changes the integration boundaries from the solid lines to the dashed lines in Figure 3.9 and increases the integration region by either, or a

<sup>3</sup> This assumption is not quite correct due to statistical errors in the Monte Carlo and the problem with radiative corrections, but can be ignored for now.

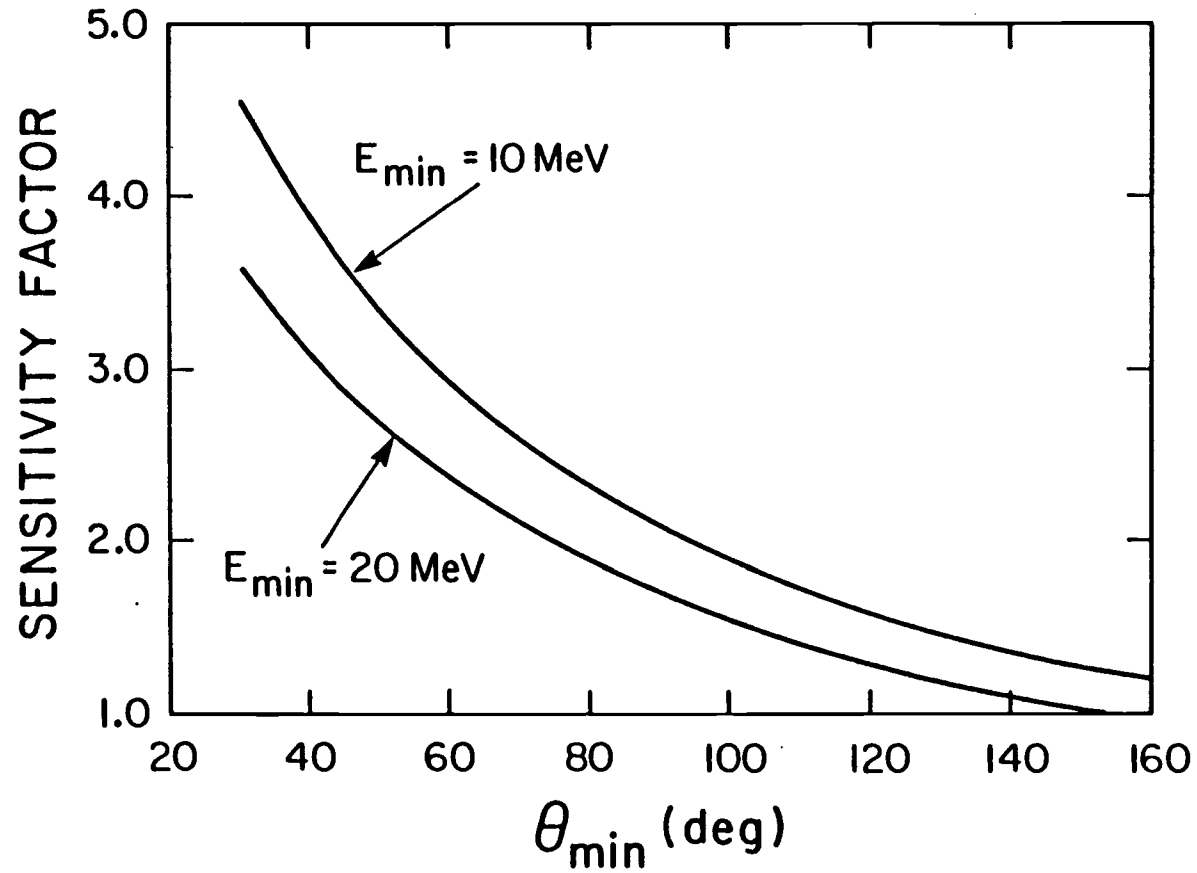


Figure 3.7 The sensitivity factor  $\Gamma_{\text{SI}}/2\Gamma_{\text{SD}}$  for an idealized detector with efficiency  $\equiv 1$  for lepton energies  $E > E_{\min}$  and pair opening angles  $\theta > \theta_{\min}$ , and zero otherwise.

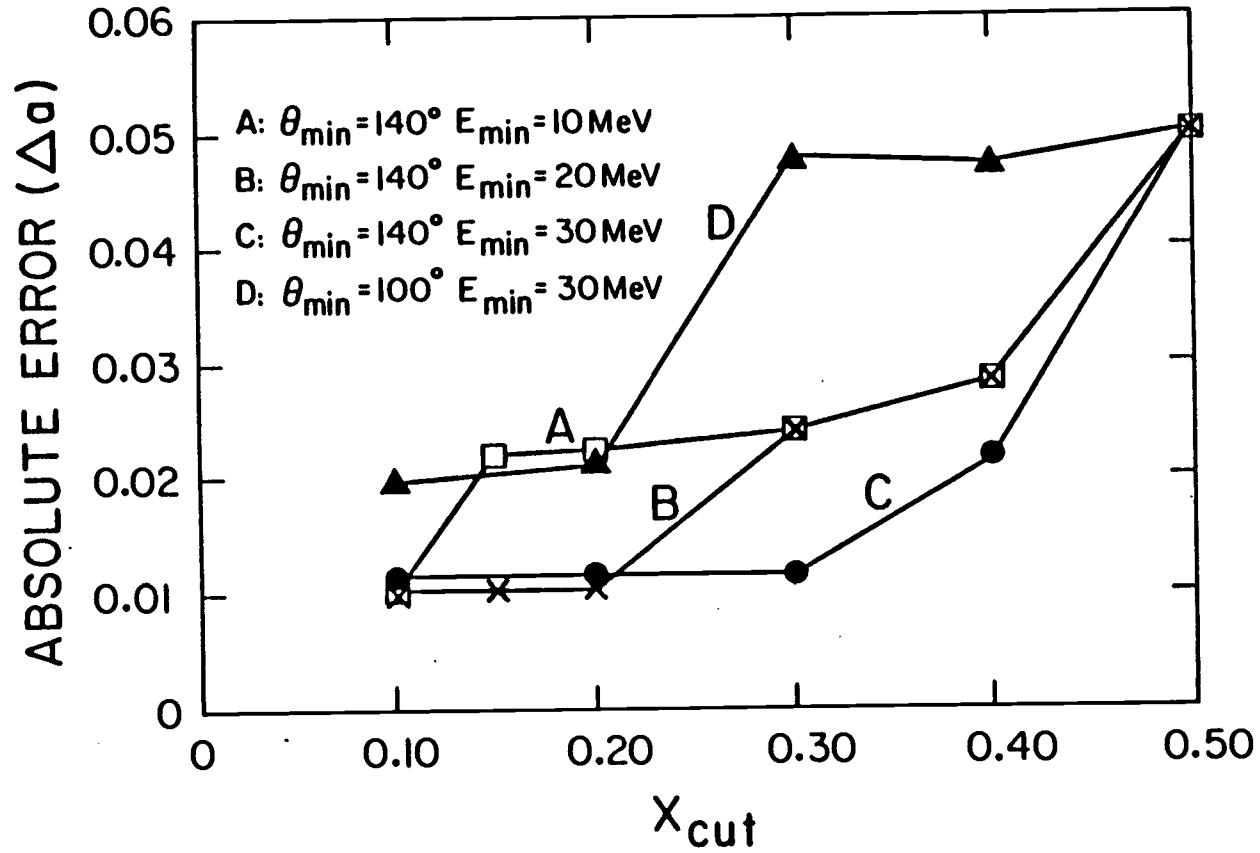


Figure 3.8 Absolute error in "a" due to a calibration error of 200keV at the Energy cut  $E_{min}$  (assuming  $a=0.03$ ) for an idealized detector with efficiency  $\equiv 1$  for pair opening angles  $\theta > \theta_{min}$ , as a function of a cut in x.

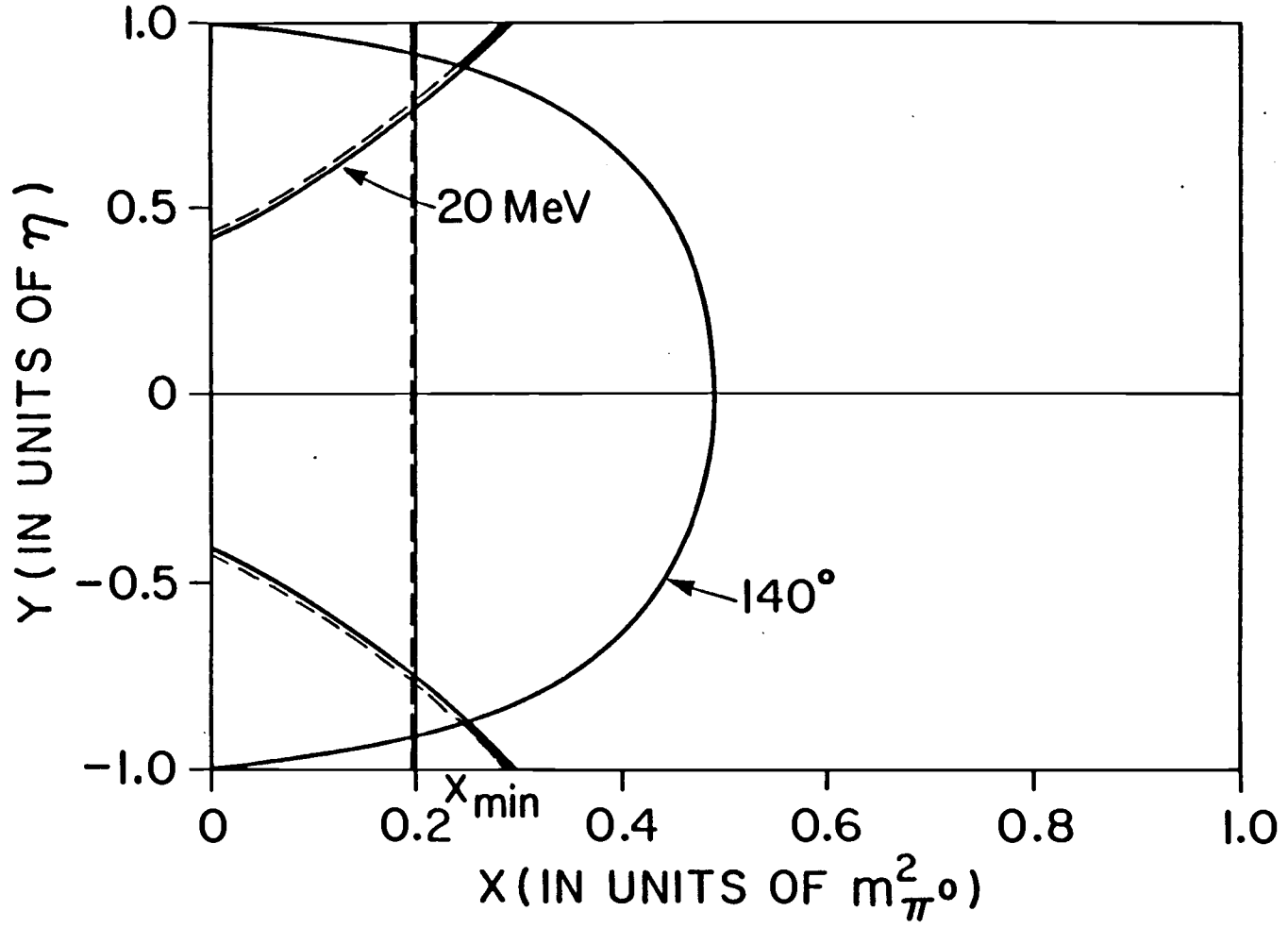


Figure 3.9 Allowed phase space (integration) region for Dalitz pairs with  $\theta > 140^\circ$ ,  $E > 20 \text{ MeV}$  and  $X > 0.2$ .

combination of the two shaded areas. The effect on the integral itself is even more pronounced since the topology of the integrand is highly peaked for small  $x$  and very asymmetric pairs, i.e., large absolute values of  $y$ . The "notch" in the curves is due to the intersection of the  $\theta_{e^+e^-} = \theta_{\min}$  and  $E = E_{\min}$  boundaries, which for  $\theta_{\min} = 150^\circ$  and  $E_{\min} = 10\text{MeV}$  occurs at  $x = 0.14$ . As long as  $x_{\text{cut}}$  is much less than this, the shift in  $x_{\text{cut}}$  with  $\Delta E$  has no effect on the branching ratio because all of the events with  $x < x_{\text{cut}}$  have already been eliminated by the  $\theta_{e^+e^-} > \theta_{\min}$  and  $E > E_{\min}$  cut. Once the smallest possible  $x$  is crossed,  $\Delta a$  increases rapidly as the integral region is now limited for small  $x$  by the  $x$ -cut. Below the steep edge of the notch  $\Delta a$  is small and  $\Delta a/\Delta E$  is independent of  $\Delta E$ . It is therefore advantageous to use a relative high  $E_{\min}$  in conjunction with an acceptance for large  $\theta_{e^+e^-}$  only. So, for example, with  $E_{\min} = 10\text{MeV}$ ,  $\theta_{\min} = 140^\circ$  and an  $x$  cut-off of 0.2-0.3 as possibly required for background suppression, one can still achieve  $\Delta a \cong 0.02$ .

This simple model indicates that one needs to know the energy calibration at just one point  $E_{\min}$ . For a linear response of the detectors one can determine  $\Delta E$  to 200keV at 10MeV by doing a  $\Delta E = 1.4\text{MeV}$  calibration at 70MeV. This is more easily accomplished than a direct calibration at 10MeV but requires a careful investigation of the detector response.

The statistical error in "a" is simply related to the total number of analysed events  $N_{e^+e^-}$ <sup>4</sup>.

$$\Delta a \approx (\Gamma_{SI}/2\Gamma_{SD}) (N_{e^+e^-})^{1/2} \quad (3.9)$$

Thus, a statistical error of  $\Delta a = 0.01$  can be achieved with  $10^4$  Dalitz events in the accepted spectrum.

<sup>4</sup> The Dalitz decay rate (1.12) is traditionally normalized to the number of ordinary  $\pi^0$  decays,  $\pi^0 \rightarrow \gamma\gamma$ . For this reason, there is also a statistical error in the measured number of these decays. However, this number is normally much larger than  $N_{e^+e^-}$  and can be neglected in comparison.

### 3.5 Normalization

For a measurement of the decay rate, one has to know the absolute normalization of the data to the number of  $\pi^0$ 's in the target accurate to 1%. This can be accomplished by using a third NaI crystal with a well defined acceptance. Knowing this acceptance, one can infer the rate of  $\pi^0$ 's in the target by simply counting the number of gammas from  $\pi^0 \rightarrow \gamma\gamma$ . The absolute normalization also depends on the efficiencies of all detectors used in the experiment. These efficiencies have to be monitored during the entire time of the experiment by specialized event triggers (see chapters 4.4 and 4.5).

In conclusion, we see that a rate measurement improves the errors in the form factor slope, but only at the expense of having to monitor the efficiencies of all the counters and the  $\pi^0$ -flux in the target. On-line monitoring of the calibration and stability is still essential to the experiment and can be achieved by studying the copious number of uncharged events.

## 4. EXPERIMENTAL DETAILS

4.1 Experimental set-up

The two large NaI crystals TINA and MINA were placed in the configuration shown in Figure 4.1. The coincident electrons and positrons were required to pass through a three wire chamber telescope and three scintillators on each side and then be totally absorbed by the NaI spectrometers. A valid event was required to produce tracks in the multi-wire-proportional counters (MWPC's) which could be traced back to a common interaction point in the active volume of the target. The variable  $x_{vis}$  was calculated from:

$$x_{vis} = (1/m_{\pi}^2) ( 2m_e^2 + 2E_{e^+e^-} - 2p_{e^+}p_{e^-} \cos \theta_{e^+e^-} ) \quad (4.1)$$

where  $E_{e^+}, p_{e^+}, E_{e^-}$  and  $p_{e^-}$ , the energies and momenta of the electron and positron, were determined by the NaI detectors and  $\theta_{e^+e^-}$ , the opening angle of the pair, was determined by the MWPC's. T1 and M1 defined the acceptance for charged particles. The lead collimators were used to define the acceptance for gammas from both the first order Dalitz term and the second order bremsstrahlung correction (see chapter 8). The layered scintillator measured  $dE/dx$  for electrons redundantly three times, to add in the separation of single electrons from electron-positron pairs (see chapter 6.1). These pairs are due to external conversions of the copious photons from the dominant  $\pi^0$  decay,  $\pi^0 \rightarrow \gamma\gamma$ , in either the target, wire chambers or the lead collimator. The MWPC's were read out by a delay-line system. This read-out system provided additional identification of wide angle external conversion pairs (see chapter 6.3).

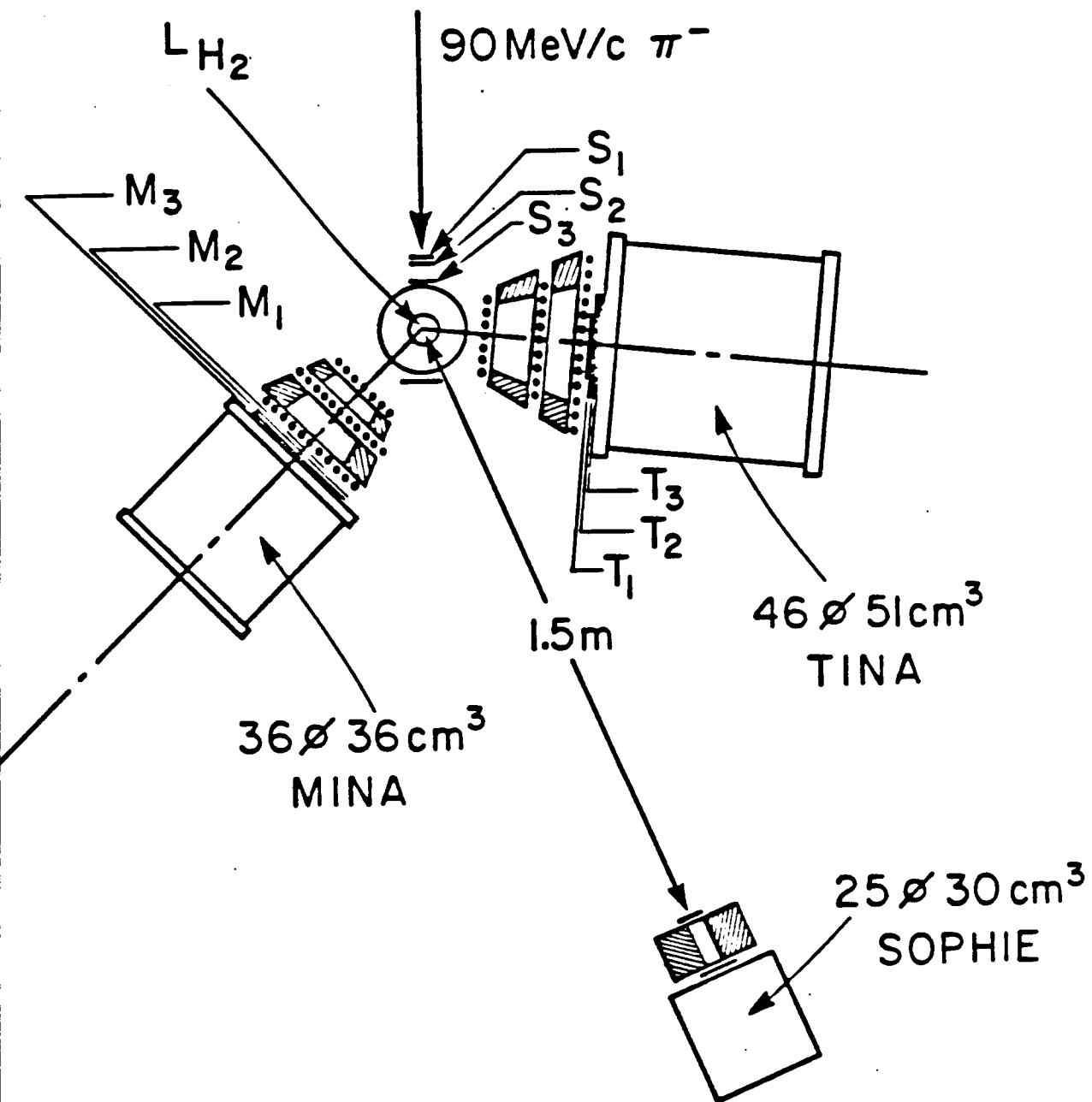


Figure 4.1 Experimental layout at  $130^\circ$

A third NaI, SOPHIE<sup>5</sup>, was used as a  $\pi^0$  monitor. It was set up to view the target through a small collimator (10cm  $\emptyset$ ) at a large distance (1.5m) and detected photons from  $\pi^0 \rightarrow \gamma\gamma$  decay. The collimator was sandwiched between two plastic counters, V1 and V2, to reject charge particles.

#### 4.2 $\pi^-$ beam

The experiment was performed in the low energy pion channel M13 at the TRIUMF facility. Negative pions are produced through proton-nuclear interactions when TRIUMF's 500MeV primary proton beam impinges on a 1cm thick graphite target. The proton beam microstructure is a 3-4ns beam pulse every 43ns. The total primary beam current is monitored with a non-interceptive capacitive pick up probe whose discriminator output can be used for timing relative to the primary proton pulse.

The low energy pion channel M13 [34] views the production target M1 from a backward angle to the primary proton beam. The channel possesses excellent momentum resolution and a narrow beam spot size both essential to the  $\pi^0$  form factor experiment as these properties allow the use of a relative small liquid hydrogen target.

In the present experiment an incident  $\pi^-$ -momentum of 90MeV/c, with a  $\Delta p/p$  of 2%, was chosen to optimize the number of pions stopped in the target. The average  $\pi^-$  stopping flux was  $2 \cdot 10^5$ /sec. The beam telescope consisted of three scintillation counters (see Figure 4.2). Counters S1 and S2 were small (2.56cm square) and thick (1cm) to define the beam spot and degrade the beam, whereas the last counter in front of the target was thin to give excellent timing resolution. Both counters S3 and S4 were built out of CD<sub>1.1</sub> to avoid  $\pi^0$  production close but outside the target. The veto counter S4 was included in the set-up for later software trigger analysis, but was not used in anti-coincidence to define a STOP-trigger. This precaution was taken because a photon from Dalitz decay which converted in the target or surrounding counters could trigger the

<sup>5</sup> On loan from the University of Oxford Nuclear Physics Dept.

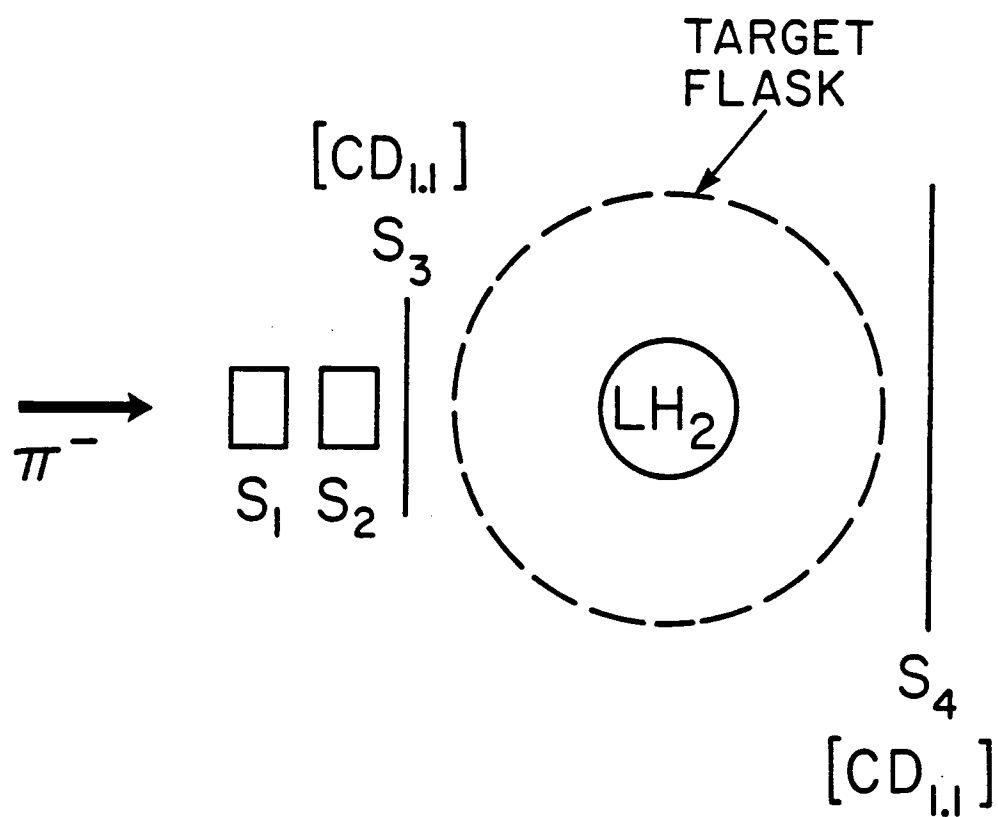


Figure 4.2 Beam telescope

veto counter and thus bias the recorded data sample. The incident beam contained approximately 60%  $\pi^-$ , 30%  $e^-$  and 10%  $\mu^-$  and had a roughly circular cross section of about 1.7cm FWQM. A time-of-flight measurement between the third beam counter S3 and the discriminator output of the capacitive pick up probe allowed separation of the pions from the muons and electrons in the secondary beam.

#### 4.3 Liquid hydrogen target

The liquid hydrogen (LH<sub>2</sub>) target flask was constructed from 0.13mm-thick mylar and was a vertical cylinder; 7.62cm in diameter and 10.16cm high. Five layers of 6 $\mu$ m-thick aluminized mylar "superinsulation" surrounded the flask. The outer vacuum jacket was an upright cylinder of diameter 19cm and height 12.70cm with a 0.13mm-thick mylar window through which the particles exited. To give rigidity to the vacuum vessel a stainless steel vertical post was unavoidable. It subtended 40° in the horizontal plane of the experiment but was positioned so as not to interfere with the particle trajectories to the NaI spectrometers.

#### 4.4 Layered scintillator

Each layered scintillator consisted of three 1.6mm-thick polyvinyltoluene scintillation counters (T1,T2,T3 and M1,M2,M3 in Figure 4.1). These counters were placed directly in front of the NaI spectrometers to minimize electron multiple scattering ahead of the wire chamber telescopes. This choice of positioning also avoided material in front of the first wire chambers which were part of the final software trigger for charge particles. The counters T1 and M1 with diameters 25.4cm and 20.3cm respectively, define the charge particle acceptance. All three scintillators and their lightguides were assembled together as one entity with only light reflecting foils separating the individual counters.

The energy lost by a charged particle traversing a 1.6mm-thick plastic counter is measured redundantly three times. Each measurement of  $dE/dx$  follows a Landau distribution, but sampled three times, it allows for separation of minimum-ionizing electrons between 10-100MeV from heavier charged particles, like muons, pions and protons, which have a considerably larger average  $dE/dx$ . It also helps to distinguish between coincident multiple electrons and single electrons. However, there is a non-unit efficiency attached to this procedure. Obviously, identifying  $e^+e^-$  pairs with high efficiency works counterproductively to the necessity of retaining most of the singles (see chapter 6.1).

A special event trigger was devised to provide layered scintillator efficiency sample events. These were single charge events with a 2 out of 3 layered scintillator coincidence and a signal in the NaI crystal. In software, all three MWPC's in front of the scintillators had to trigger as well. In case of the circular defining counter, the charge particle track was required to intersect its active area. We found that the efficiencies were constant and between 98-100% for all counters.

#### 4.5 Wire chamber telescope

The six proportional wire chambers used in the experiment were equipped with delay-line read-out systems. They were arranged into two telescopes with three chambers each. The two front chambers were 12.7cm square, the last chamber on the TINA side was 30.05cm square and all other wire chambers were 20.3cm square chambers. The middle chambers on both sides were newly constructed to minimize multiple scattering by substantially decreasing the material used for the anode plane. All wire chambers were mounted perpendicular to the detector axis and held in place by aluminum frames to prevent any movement after installation. The gas mixture was 65.7% argon, 30% isobutane, 4% methylal and 0.3% freon.

Several types of information aided in the determination of the wire chamber positions. Optical survey measurements were made on all chambers both before and after the experiment. The separation between chamber planes was determined to within an uncertainty of  $\pm 1.5\text{mm}$ . The absolute transverse chamber locations were also known to within  $\pm 1.5\text{mm}$  from these measurements.

For a delay-line chamber, the true location of a particle is determined from the time difference in the signal appearance at the two ends of the delay-line. By measuring this time difference and by knowing the velocity of the signal in the delay-line and the zero-time offset of these signals, one is able to calculate the position of the hit within the chamber. A collimated ruthenium  $\beta$ -ray source mounted on a precision template allowed us to determine the zero-time offset and signal velocities of each delay-line. The template itself was centered along the telescope axis with the help of a theodolite.

A small counter (1cm) was installed in the lower corner of each detector arm. In these counters some of the copious photons from  $\pi^0 \rightarrow \gamma\gamma$  decay converted into electron positron pairs. These events were tagged by a coincidence between the small counter, the three layered scintillators and the NaI crystal. In addition, a 2 out of 3 wire chamber coincidence was requested in software. These events provided an on-line monitor of the MWPC efficiencies. For this purpose, a routine was developed which was compatible with the data acquisition program. It displayed the number of wire chamber hits for every set of one thousand sample events.

#### 4.6 Sodium iodide crystals

Three large sodium iodide crystals were used in the experiment. The two largest TINA ( $46\text{cm}\emptyset * 51\text{cm}$ ) and MINA ( $36\text{cm}\emptyset * 36\text{cm}$ ) were used to detect the  $e^+e^-$  pairs. Their response function had to be known

for electrons over the entire region of acceptance, i.e., incident position, angle and energy.<sup>6</sup> The energy calibration had to be known at all times to better than 200keV at 10MeV. A third sodium iodide detector, SOPHIE (25cm $\phi$  \* 30cm), was used to monitor the  $\pi^0$  production rate by detecting gamma rays from  $\pi^0 \rightarrow \gamma\gamma$  decay. A resolution of better than 10% was required to distinguish these gamma rays from those from the process  $\pi^- p \rightarrow n \gamma$ , and it was necessary to measure SOPHIE's acceptance to 1%.

TINA and MINA were returned to their manufacturers for surface recompensation to improve their uniformity. Their old photo-multiplier tubes were replaced by RCA S83006E tubes and the number of tubes on MINA was increased from four to seven. The procedure of surface recompensation is outlined in a paper submitted to Nucl. Inst. Meth. [51].

<sup>6</sup> Photons are equivalent to electrons since they convert at the interesting energies immediately into  $e^+e^-$  pairs.

## 5. EXPERIMENTAL PROCEDURE

The experiment was conducted in two runs during the first half of 1984. The data taking was interrupted by a period reserved for cyclotron maintenance. The initial run in February was used to set up the experimental arrangement, string cables, time-in the electronics and thoroughly test the logic. Various properties of the detectors were checked as well. These checks included: finding the efficiency plateaus of all the plastic scintillators, balancing the seven photo-tubes of each NaI crystal, surveying the wire chamber telescopes and aligning both detector arms. We also went through the motions of the several measurements necessary during final data taking.

The actual data taking took place from April 30 to June 15 1984. Initially, a lead converter sheet was placed in front of the layered scintillators to measure their response to  $e^+e^-$  pairs for later comparison with Monte Carlo simulations. Then, TINA and MINA were, in turn, swung around so as to be at the end of the M13 beam line, at a position downstream of the focus, so that the entire front face was illuminated. With the MWPC's it was possible to bin the response function off-line according to position and angle of illumination. Electrons were selected from other particle species by time of flight relative to the signal from the capacitive probe. Matching the outputs of the individual photo-multiplier tubes (PMT's) was done with a 90MeV beam normally incident along the crystal axis. The balance was checked at lower energies and was found to be good to 1%. To decrease the accepted momentum bite in the beamline, the vertical and horizontal slits were closed to a few millimeters. This reduced the contribution of the finite beam momentum spread to the width of the resolution functions to less than 1%. The response function of the two NaI crystals for several electron energies was measured before and after the actual data-taking.

The electrons in beamline M13 can also be used as a quasi-monochromatic calibration source when the large NaI detectors are positioned in the beam. By using different momentum tunes for the beamline components, it was possible to select any desired momentum between 30MeV/c and 110MeV/c. The absolute momentum calibration was based on the best tune for surface muons.<sup>7</sup> To establish this tune, the channel was switched to  $\pi^+$  and the muons were stopped in a thin plastic counter. The decay electrons from  $\mu^+ \rightarrow e^+ \bar{\nu}_\mu \nu_e$  were counted in TINA which was positioned at ninety degrees to the beamline. The bending dipole magnets B1 and B2 and the quadrupole magnets Q1 through Q5 of M13 were adjusted to maximize the counting rate in TINA. The counting rate was normalized to the current of the primary proton beam onto the production target. The magnetic fields of the dipole magnets were measured with NMR probes. Linearity was found between redundant Hall-probe readings, NMR readings and the currents in the magnets. The counting rate in TINA, maximized by optimal quadrupole settings, is given in Figure 5.1 as a function of the magnetic field in B1. The surface muon edge at 29.8MeV/c is associated with a point two thirds up the curve from the high field side. This point is uncertain by about 180keV/c.

The in-beam energy calibration was supplemented by stopping  $\pi^+$  in a liquid hydrogen target. The energy spectra of the Michel positrons and positrons from  $\pi^+ \rightarrow e^+ \nu_e$  decay were measured in both TINA and MINA (see for example Figure 5.2). This measurement provided two additional points for the energy calibration of TINA and MINA with charged particles, 53.85MeV for  $\pi^+ \rightarrow \mu^+ \rightarrow e^+$  and 70.81MeV for  $\pi^+ \rightarrow e^+ \nu_e$ .

<sup>7</sup> Surface muons are muons from pion decay on the surface of the production target. For pions decaying inside the target, the muons from the decay lose energy traversing the target material and therefore have less momentum when entering the secondary beamline. The surface muons carry away the total available Q-value for the pion decay  $\pi^+ \rightarrow \mu^+ \nu_\mu$  which translates into a momentum of 29.8MeV/c.

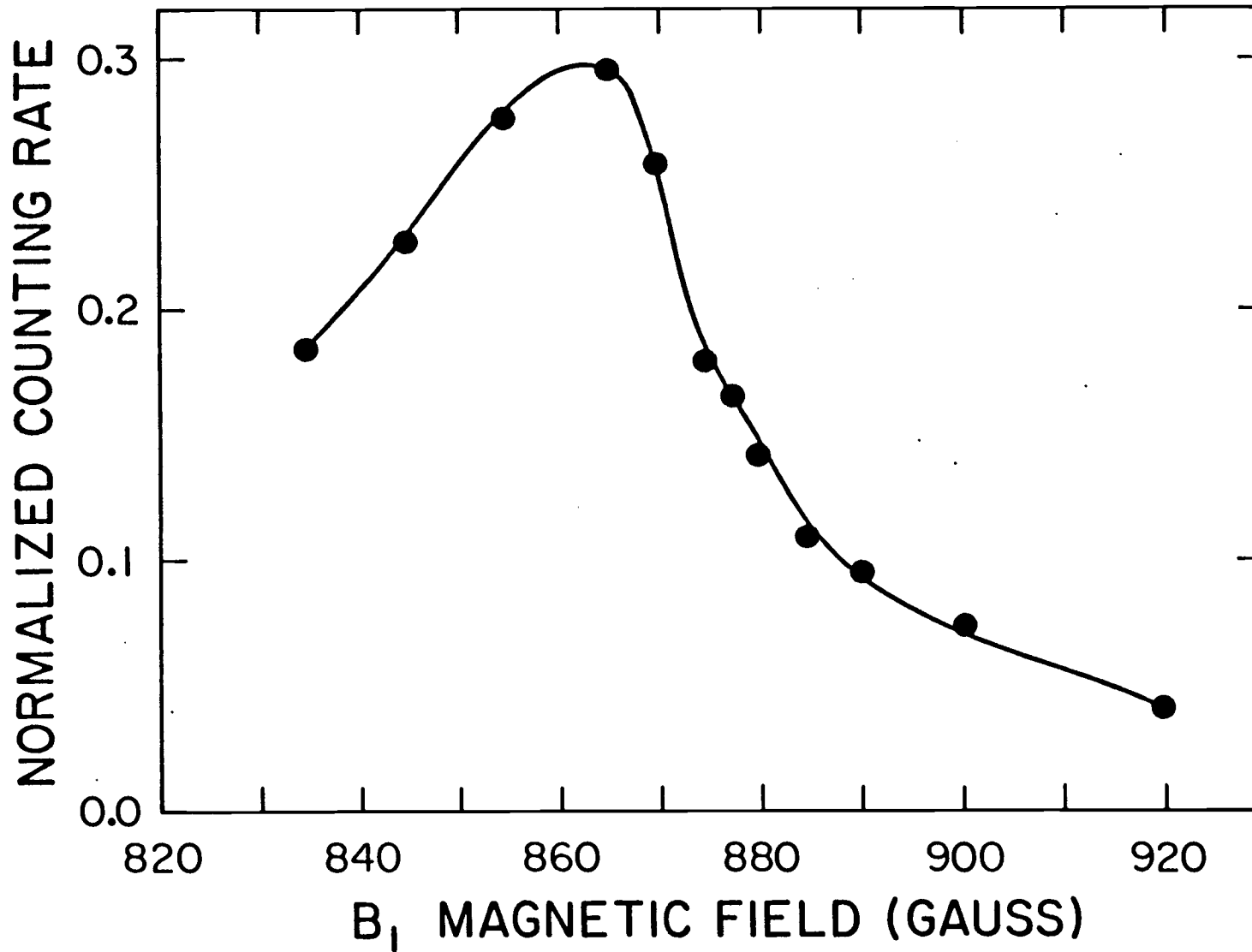


Figure 5.1 Surface muon edge

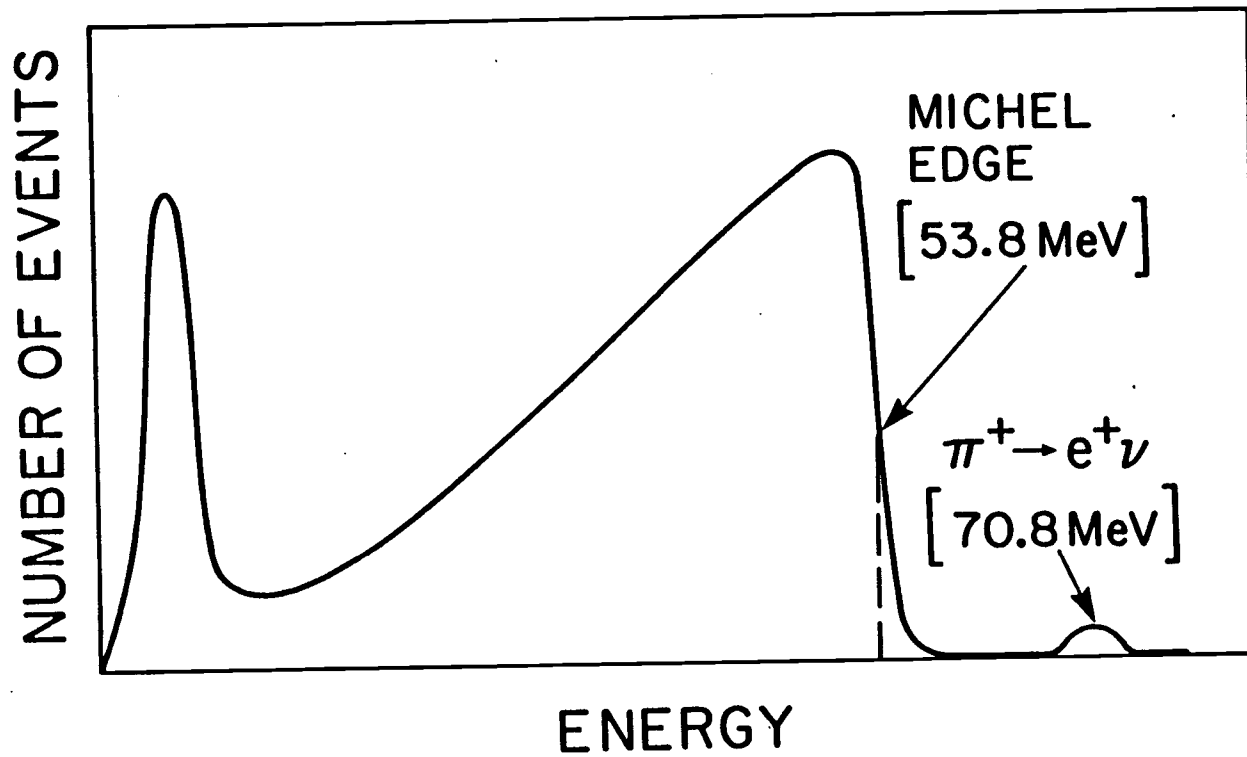


Figure 5.2 Sketch of the detected  $\pi^+ \rightarrow e^+ \nu_e$  spectrum

Finally, the beam line was switched to 90MeV/c  $\pi^-$  and  $\pi^-p \rightarrow n \pi^0 \rightarrow e^+ e^- \gamma$  data was taken at three detector opening angles. Four different event types were written onto tape: The so called type 1 events not only included all charge-charge coincidences, but also some charge-neutral, neutral-neutral, neutral-singles, charge-singles, LS-efficiency sample events and WC-efficiency sample events; the rate of which were reduced by forcing a coincidence with a random pulser. For every event we recorded ADC and TDC spectra from both NaI crystals (TINA and MINA), the four beam counters and six layered scintillators. In addition, the time spectra of the signals from all delay-line discriminators were digitized and recorded on tape. The different kinds of type 1 events were identified by unique bit-patterns in a CAMAC bit register. Charge particles were distinguished from neutrals by a hit in all three layered scintillatores. The data aquisition was controlled by the Multi-data aquisition program, originally developed at Fermi-lab, and a PDP-11 computer.

The neutral singles events from SOPHIE were considered type 2 events and the read-outs of various CAMAC-scalers constituted type 3 events. We also used a LeCroy buffered ADC (CAMAC Module 3512) and a LeCroy Memory Module (CAMAC Module 3588) to histogram the total neutral spectrum in all three NaI spectrometers. These histograms were accumulated independently from the data aquisition computer and were read out every minute. These histograms were tagged as type 4 events and were used off-line as a monitor of the gain stability.

The acceptance of SOPHIE was determined in a separate measurement by inserting a lead-scintillator sandwich in front of MINA tagging the gamma rays incident on a geometrically well defined region, i.e., the lead converter. The layout is shown in Figure 5.3. The number of coincidences between a photon conversion in the lead-scintillator sandwich and a neutral prompt in SOPHIE can be used to extract the effective solid angle of SOPHIE (see chapter 6.6).

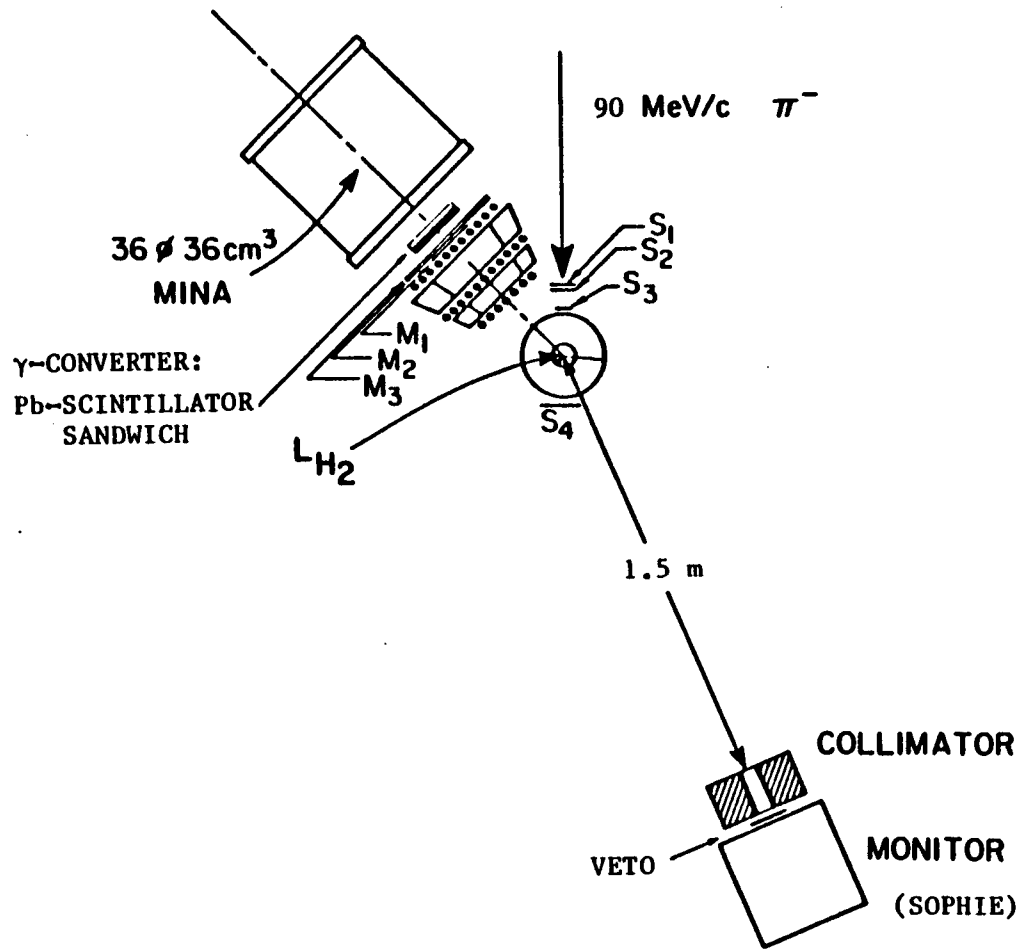


Figure 5.3 Absolute acceptance calibration of  $\pi^0$ -monitor SOPHIE

## 6. PRELIMINARY ANALYSIS

Before we could determine the  $\pi^0$  form factor slope from the data, various parts of the detection system had to be understood first. This included a study on the electron positron pair identification by the three scintillator arrangement, reconstruction properties and position calibration of the wire chamber telescopes and response function parameters of the NaI crystals. In addition, the efficiencies of all counters and the energy calibration of the NaI crystals had to be established beforehand.

### 6.1 Electron positron pair identification by a three scintillator arrangement

The principle of pair separation by the layered scintillators was described in chapter 4.4. Here, we focus on the efficiency with which this can be accomplished. The responses of the layered scintillators to singles were established by analysing  $\pi^-p \rightarrow e^+e^-n$  events which lie in a kinematic region where pairs from external gamma conversions do not contribute to the spectrum. When these empirical responses were sampled in a Monte Carlo program we obtained the efficiencies for singles and rejection probabilities for pairs by calling the response function once for every counter to simulate singles, and twice to simulate pairs. Since the gains and pedestals of the various counters were not identical, their responses were first scaled. The two smaller pulses were then added together and a cut was applied to the sum. This proved to produce slightly higher efficiencies to detect pairs and retain singles than if we had used all three pulses. For the TINA layered scintillator assembly the result, as a function of the cut applied, is shown in Figure 6.1. For a cut at a low channel number, the probability of identifying a

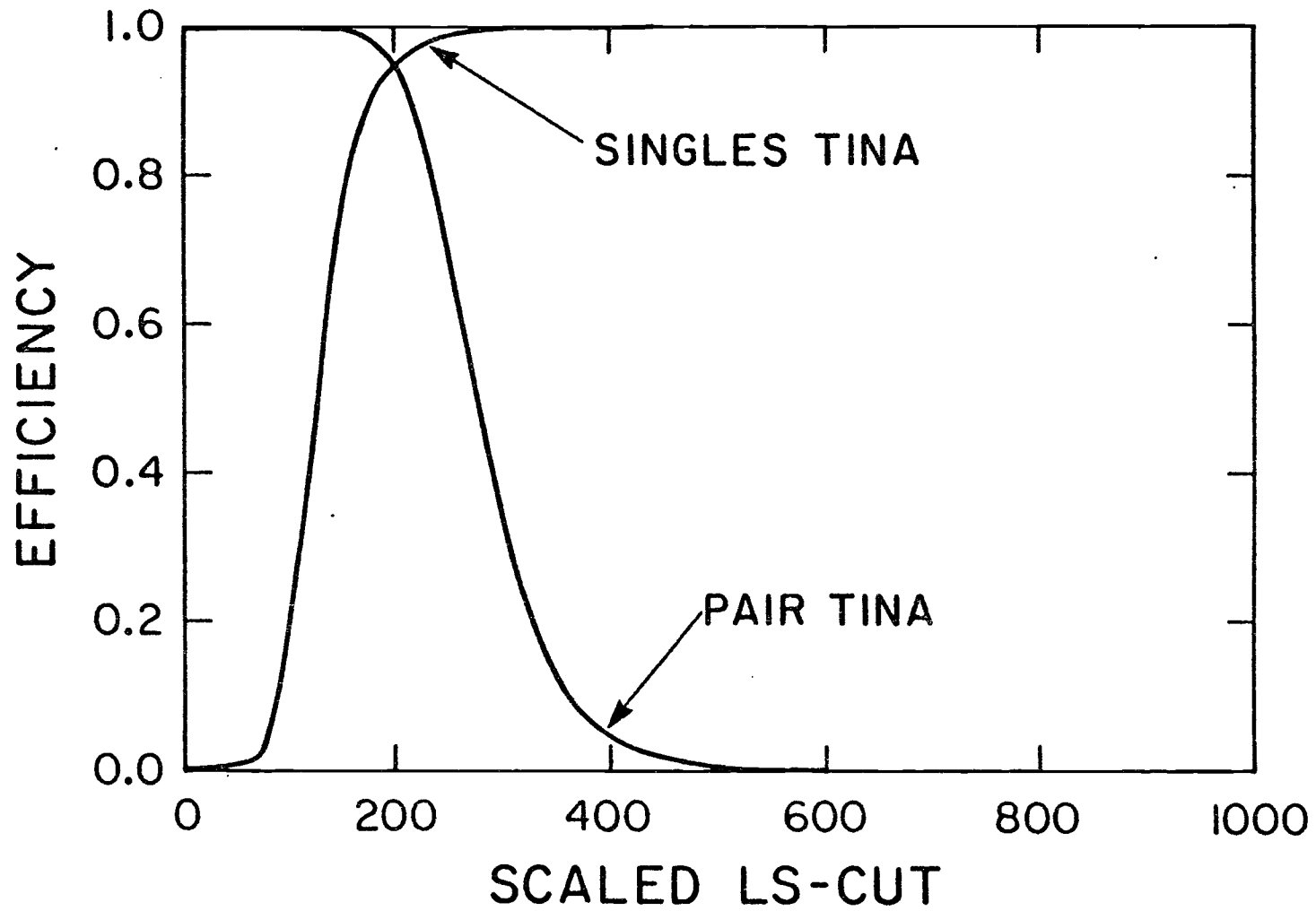


Figure 6.1 TINA layered scintillator response

pair is high but consequently the efficiency for retaining singles is quite low. Unfortunately, there is no region where both efficiencies are high and where the curve changes little with the exact position of the cut.

Since the absolute normalization of the experiment was of primary importance, we decided not to include cuts on the layered scintillators in the final analysis. This decision avoided uncertainties in the normalization which otherwise would have been inevitable due to the steepness of the curves for cuts with high single efficiency and reasonable pair rejection. The curve for singles in Figure 6.1 was verified by applying the above analysis procedure to the  $\pi^-p^+e^+e^-n$  events. Comparison showed that the Monte Carlo program reproduced the empirical distributions quite accurately.

## 6.2 Resolution of the wire chamber telescope

The values for the delay-line constants were refined by data taken when the telescopes were in turn placed in the beam of M13. Electrons were selected by time of flight relative to the cyclotron pulse. Data was taken for electron energies of 30,50,70 and 90MeV. The analysis proceeded as follows: First, the hits in all three chambers were fitted to a straight line by the minimum  $\chi^2$  method. Then, distributions were plotted for the deviations of particle hits from these trajectories.<sup>8</sup> Finally, an iterative procedure which centered all three "difference" spectra for a given coordinate simultaneously at zero, provided an accurate determination of the needed zero-time offset. Once the distributions were centered, the delay-line signal velocities were obtained by simultaneously minimizing the width of each "difference" spectrum. In order to define the centroid of the distributions more precisely, constraints were placed on the quality of the fit in the coordinate orthogonal to

<sup>8</sup> These distributions are referred to as "difference" distributions in the rest of the text.

the one being examined. This tended to eliminate events that underwent large multiple scattering deflections. In this way, the relative transverse locations of all the chambers were obtained to a precision of  $\pm 0.2\text{mm}$ . The final values for the zero-time offset were at most 1.5mm different from the numbers previously measured with the ruthenium  $\beta$ -source. Systematic errors occurred unless we used the original values for the zero-time offset, obtained with the  $\beta$ -source, as the initial estimates in the optimization program. The velocity constants were quite well determined by the source method and no improvements could be made to the width of the "difference" distributions. The above procedure was repeated whenever the detector arms had been moved. In this case, the program analysed high energy  $\pi^-p \rightarrow e^+e^-n$  events from the target.

The MWPC's position resolutions were determined by comparing the measured "difference" distributions with those from Monte Carlo simulation. For every Monte Carlo generated event, the program calculated the intersections of the particle trajectory with the location of the wire chamber planes. The simulated trajectory included multiple scattering in the media of the wire chambers and the intervening air gaps. The magnitude of this effect was calculated from Moliere polar angle distributions. Each wire chamber was modeled according to its design, including the probability of hitting a wire. Stoichiometrically weighted Z and A values and densities were used for the different chamber components; like mylar, gas, cathode and anode wires. The program traced the particles in many small steps through the various media. It was found, that the anode is the most powerful scatterer and that the amount of multiple scattering is quite energy dependent. The Monte Carlo events were processed by the same reconstruction routine that was eventually used for the actual data.

To simulate the data properly, it was necessary to include the effect of intrinsic chamber resolutions. We assumed that all six chambers had the same intrinsic resolution since they were very similar in design with respect to wire spacing and distances between

anode and cathode planes. The chamber resolutions were obtained by displacing Monte Carlo generated hits with a Gaussian resolution function and comparing the resulting "difference" distributions with those from in-beam data which had a FWHM of about 1.0-1.5mm. We found, that the intrinsic resolution accounts for 80% of this width, and that the energy dependence in multiple scattering becomes undetectable once it is convoluted with the chamber resolutions. This was also born out by the in-beam spectra, which showed no change in resolution with beam energy.

As a result of this analysis, we decided that the Monte Carlo program for the simulation of the Dalitz decay experiment, can be simplified if we sample from the empirical "difference" spectra of the in-beam runs directly. This automatically includes both multiple scattering and chamber resolutions. For a point source, the program demonstrated that the experimental geometry at  $156^\circ$  enables us to reconstruct the interaction point accurate to about 1.2cm FWHM in the horizontal plane and 0.5cm in the vertical direction. The same analysis revealed that the angle between the electron positron pairs can be determined to an accuracy of about  $0.5^\circ$  FWHM.

Nevertheless, to decide whether a given electron goes through the defining counter, multiple scattering in the target and wire chambers had to be included in the Monte Carlo simulation program. To this end, media data files, representing the wire chambers as homogeneous media, were compiled for use in the EGS (electron-gamma-shower) package [36] (see chapter 7). As a test of the data files, multiple scattering was considered and the distributions from EGS were found to agree to within 10% in  $\sigma$  with the results obtained when the MWPC's were simulated in detail.

### 6.3 Wire chamber efficiencies

To obtain additional information on the efficiencies of the wire chambers from off-line analysis, a method was developed, where

$\pi^- p \rightarrow n e^+ e^-$  events were selected from the  $E_{\text{tot}}$  vs.  $x_{\text{vis}}$  scatterplot in a region free of other events (see Figure 3.1). For these events a 5 out of 6 wire chamber coincidence was required. A straight line had to track back to the target in the opposite telescope arm of where a chamber was tested. In addition, this line had to have a close approach with a second line connecting the hits in the other two chambers on the side of interest. Furthermore, the second line had to intersect the active area of the wire chamber which was examined. Only events with all MWPC hits inside the collimator aperture were used as a sample. These narrow requirements resulted in a very limited sample size. To improve the statistics, data runs were combined where the on-line method (see chapter 4.5) indicated no change in efficiency for a given chamber. The off-line method gave efficiencies which were slightly lower (0.25-1.0%) in comparison to the on-line analysis, especially when the efficiency was low all together. Since the small counter method measured mostly the efficiency of a chamber for a pair of electrons, the results from  $\pi^- p \rightarrow e^+ e^- n$  events were ultimately used in the normalization of the experiment.

The sum of the time measured at the two ends of the delay-line was required to lie within a window corresponding to the spread in ion drift-time to the MWPC wires. Again, in-beam electron data were used to establish the width of these windows. For multiple tracks, the sum lies somewhat lower than for a single electron, depending on the separation of the hits in that coordinate. Furthermore, the delay-line sum of the x and y-coordinate are correlated for a single hit by the common drift-time to the anode wires. This is not true for multiple hits. To distinguish between pairs and single electrons, the data analysis program applied a cut on the diagonal in the scatterplot of the y delay-line versus the x delay-line sum. It also applied a cut on the individual sums. To obtain the efficiencies of these cuts for single hits we applied the very same cuts to the  $\pi^- p \rightarrow e^+ e^- n$  data set, which was at that time believed to be free of external conversion pairs (see chapter 9.3).

#### 6.4 NaI response functions

The hydrogen target in the experiment was small when viewed by the crystals, resulting in a strong correlation between angle and position of illumination. The data from in-beam measurements was therefore combined in bins of angle ( $2.5^\circ$ ) and distance from center (2cm). The distribution of signal amplitudes for each bin and energy were fitted to a lineshape form with three free parameters:<sup>9</sup>

$$R(E) = A \exp \left[ \frac{(E-b)}{d} \right] \left[ 1 - \operatorname{erf} \left( \frac{(E-b)}{c} \right) \right] \quad (6.1)$$

The peak position is somewhat higher than  $b$ , by the amount  $\Delta$  and the FWHM resolution is approximately  $c + d$ ;  $c$  being the half-width on the high-energy side and  $d$  being that on the low-energy side. The parameters  $\Delta$ ,  $c$  and  $d$  have units of MeV and were normalized to the incident electron energy. Their change from bin to bin was noted relative to the central bin. A linear interpolation between the parameters obtained at the energies 30,50,70 and 90MeV produced the parameters of the NaI response at all intermediate energies. For electrons closest to the crystal center and normal incidence, i.e., bin 1, the resolution at 30MeV is 6.8% for TINA and 8.0% for MINA. At 90MeV TINA's resolution is 3.6% and 4.6% for MINA. The energy dependence of the bin 1 resolution is approximately  $E^{-0.55}$ , which is the same as that quoted by a Brookhaven group [35]. This dependence indicates that the non-uniformities of the crystals are so small as to contribute less to the resolution than the statistics of thallium photo-emission. At high energies, the resolution rises more sharply with bin number, since the showers are larger and more readily expand beyond the confines of the crystal.

<sup>9</sup> A is only a normalization factor.

To determine the origins of the response of TINA and MINA, a series of calculations were made using as a basis the Monte Carlo code EGS which traces the progress of electromagnetic showers through material [36]. EGS was used to calculate the amount of energy deposited in the crystals by electrons of various energies incident on the entire front face. The data was binned according to incident position and angle in the same manner as the experimental data. The resolutions obtained in this way were smaller than the measured values since they only include effects of shower leakage. The effects of photon statistics were then simulated. Some estimates had to be made of the actual number of photons reaching the PMT's at the back of the crystal. Of the photons created in the shower, a large fraction would be lost in the many reflections from the walls. It was assumed that the low energy ( $<1\text{MeV}$ ) resolution is entirely attributed to photon statistics; the number of photons produced are small and the effects of crystal non-uniformities and shower leakage are low because the showers are small. The resolution for 661keV gamma rays from a  $^{137}\text{Cs}$  source in the center of the crystal (14% and 12% for TINA and MINA respectively) was scaled with energy, to give the statistical component. This additional component was used to spread the bare crystal response.

Due to the many assumptions which had to be made, it is hardly surprising that the resolutions obtained in this way are distinct from the experimental values. The problem is very complex and it is customary to parametrize the discrepancy in resolution by an empirical formula. A Stanford group [37] suggested a form:

$$\left[ \frac{\Delta E}{E} (\% \text{ FWHM}) \right]^2 = \alpha + \beta/E \quad (6.2)$$

Our results tend to confirm this energy dependence but give no evidence for a constant term, suggesting that the discrepancy is

largely of statistical origin. For particles entering toward the edge of the crystal, the effects of shower leakage dominate and are well simulated by the EGS code. We had no resolution data available from in-beam measurements for particles entering the crystal outside the defining counter, and could in this case, only rely on the EGS-method to give a sufficient approximation of the resolution.

## 6.5 Energy calibration of the NaI crystals

### 6.5.1 In-beam energy calibration

The calibration function of the NaI detectors is obtained by plotting the peak position of the NaI response versus incoming electron energy. A typical curve is shown in Figure 6.2. We observed a slight saturation effect at high energies in both crystals at the beginning of the experiment. Fitting the data points below 90MeV to a straight line gives correlation coefficients of 0.999947 for TINA and 0.999865 for MINA. It should be noted that the calibration curves give the crystal response to incoming electrons which have already lost some of their energy by going through the wire chambers, layered scintillators and the crystal front face and thus actually deposit less energy in the crystal itself. The deposited energy of a positron differs by twice the electron rest-mass from that of an electron. Otherwise the crystal response is independent of particle type.

### 6.5.2 $\pi^+ \rightarrow e^+ \nu_e$ energy calibration

The two-body decay  $\pi^+ \rightarrow e^+ \nu_e$  provides a source of monoenergetic positrons at 70.81MeV, while the decay positrons from the  $\pi^+ \rightarrow \mu^+ \nu_\mu \rightarrow e^+ \nu_e \nu_\mu$  chain give a spectrum with an edge at 53.85MeV (see chapter 5). These two points can be used to confirm the the in-beam calibration data. However, the energy loss these positrons suffered by

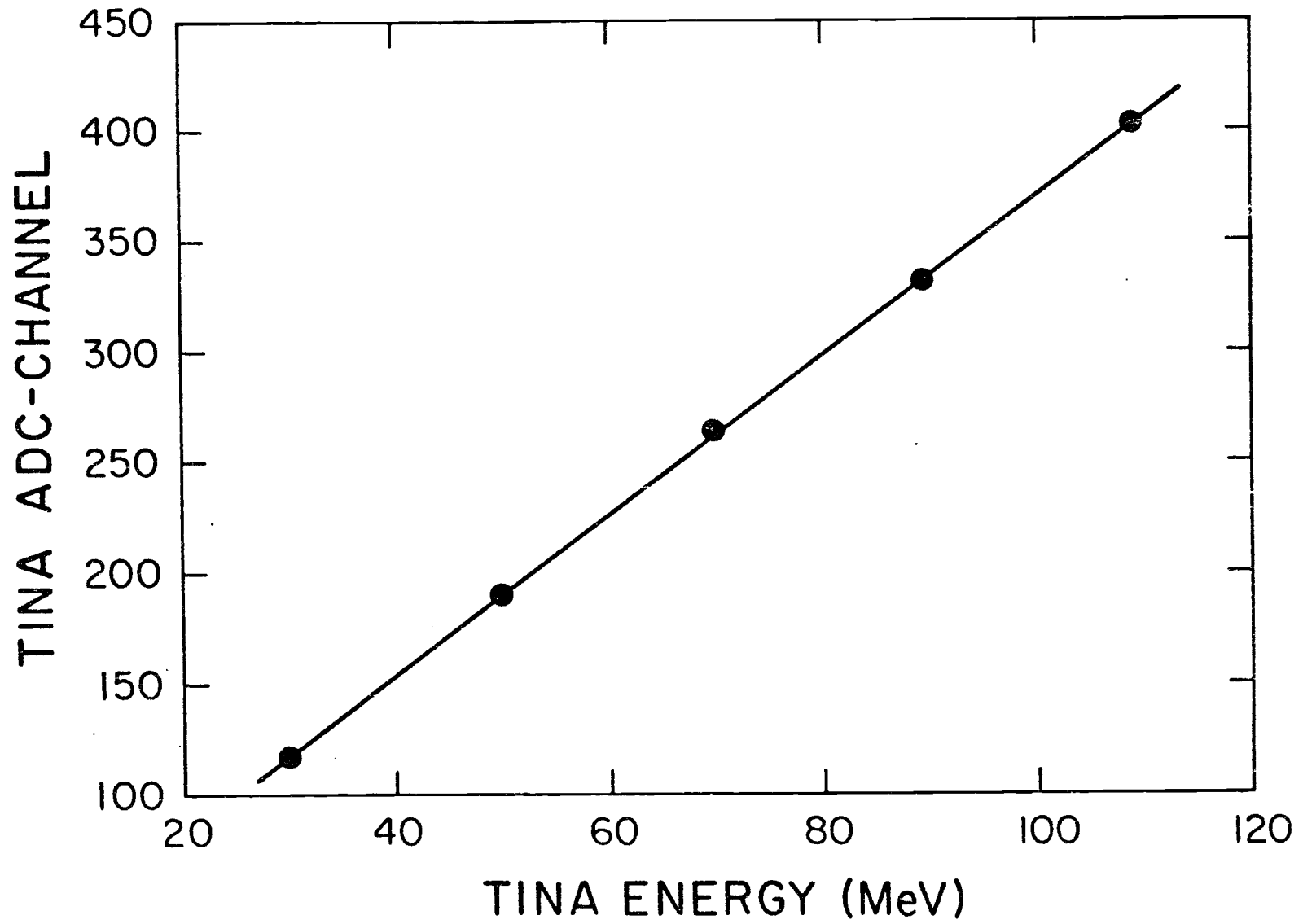


Figure 6.2 TINA in-beam energy calibration

traversing the target has to be taken into account in a direct comparison with in-beam positrons. Since the  $\pi^+ \rightarrow e^+ \nu_e$  half-life is much shorter than the half-life for the  $\pi^+ \rightarrow \mu^+ \rightarrow e^+$  chain, a TDC cut on prompt events was used for the spectrum in Figure 5.2. In hardware, a coincidence was created which already favored prompt over delayed events and therefore enhanced the ratio of  $\pi^+ \rightarrow e^+ \nu_e$  electrons over Michel electrons in the recorded data sample. Without this hardware trick the spectrum would have been completely swamped with Michel electrons since the branching ratio for  $\pi^+ \rightarrow e^+ \nu_e$  is four orders of magnitude smaller than that for the branch  $\pi^+ \rightarrow \mu^+ \rightarrow e^+$ . The peak was fitted to the TINA function (eq. 6.1). The position one third up the Michel edge is equivalent to 53.85MeV.<sup>10</sup>

### 6.5.3 Energy calibration with neutral events

The neutral single spectra contain a peak at 129MeV from  $\pi^- p \rightarrow n \gamma$  and two edges of a box at 55MeV and 83MeV from  $\pi^0 \rightarrow \gamma \gamma$ . The spectra for each crystal and each run (data tape) were fitted to EGS calculations of the response to the  $\pi^0$  box. These EGS distributions were created separately for each crystal and included a gaussian part for the finite energy resolution. In this way, the centroid position of the box could be obtained to a statistical accuracy of only one in typical 300 channels. The 129MeV point was not used because of possible saturation effects. Thus, the only other point available to establish a calibration curve from neutrals was the pedestal. However, there were various problems associated with determining the pedestal position. The pedestal was measured in TINA when a single neutral event triggered MINA and vice versa. The resulting histogram was then fitted by a Gaussian. It was realized only later, that for a 2259A peak-sensing LeCroy ADC the measured pedestal is somewhat higher than the projected zero obtained from

<sup>10</sup> This statement is based on the analysis of a previous  $\pi^+ \rightarrow e^+ \nu_e$  thesis with the same detectors [52].

calibration. This suspicion arose when the measured 129MeV peak position was compared with its position as predicted from a slope given by the measured pedestal and the  $\pi^0$ -box. There was no explanation other than an error in energy calibration when, during the last runs of the experiment, the measured 129MeV peak was found to be higher than predicted. In contrast, saturation effects at the beginning of the experiment account for a measured 129MeV peak to be lower than expected. Indeed, various tests with the 2259A ADC using a precision pulser showed that the difference between measured pedestal and projected zero depends on gate width and even peak position inside the gate; variables which were not anticipated to be of any consequence for a peak-sensing ADC.

An ultrasonic survey was performed on the front faces of TINA and MINA to determine the thickness of the aluminum to an accuracy of 0.04mm. We resorted to a measurement because previous experiments with the crystals concluded that the specifications of the manufacturers may not be trusted. The aluminum thickness was found to be 1.96mm in TINA and 5.15mm in MINA. A dedicated EGS program was then used to determine the energy lost by an electron traversing all "dead layers" before entering the crystal. The simulation included the layered scintillator, the crystal front face with its layers of aluminum, MgO reflector and rubber and an estimate of wrapping used for the scintillators. The result is energy dependent and given in Figure 6.3.

The in-beam calibration curve relates ADC channels to incoming electron energies, i.e., the energy of the electrons as selected by the bending magnet B1 in M13. The energy loss in the "dead layer" was subtracted from every point on the in-beam calibration curve to provide a relationship between deposited energies and ADC channels. Figure 6.4 helps to explain the method used to calculate the projected zero of the ADC. This method was possible because the gains for both crystals were quite different in the two in-beam

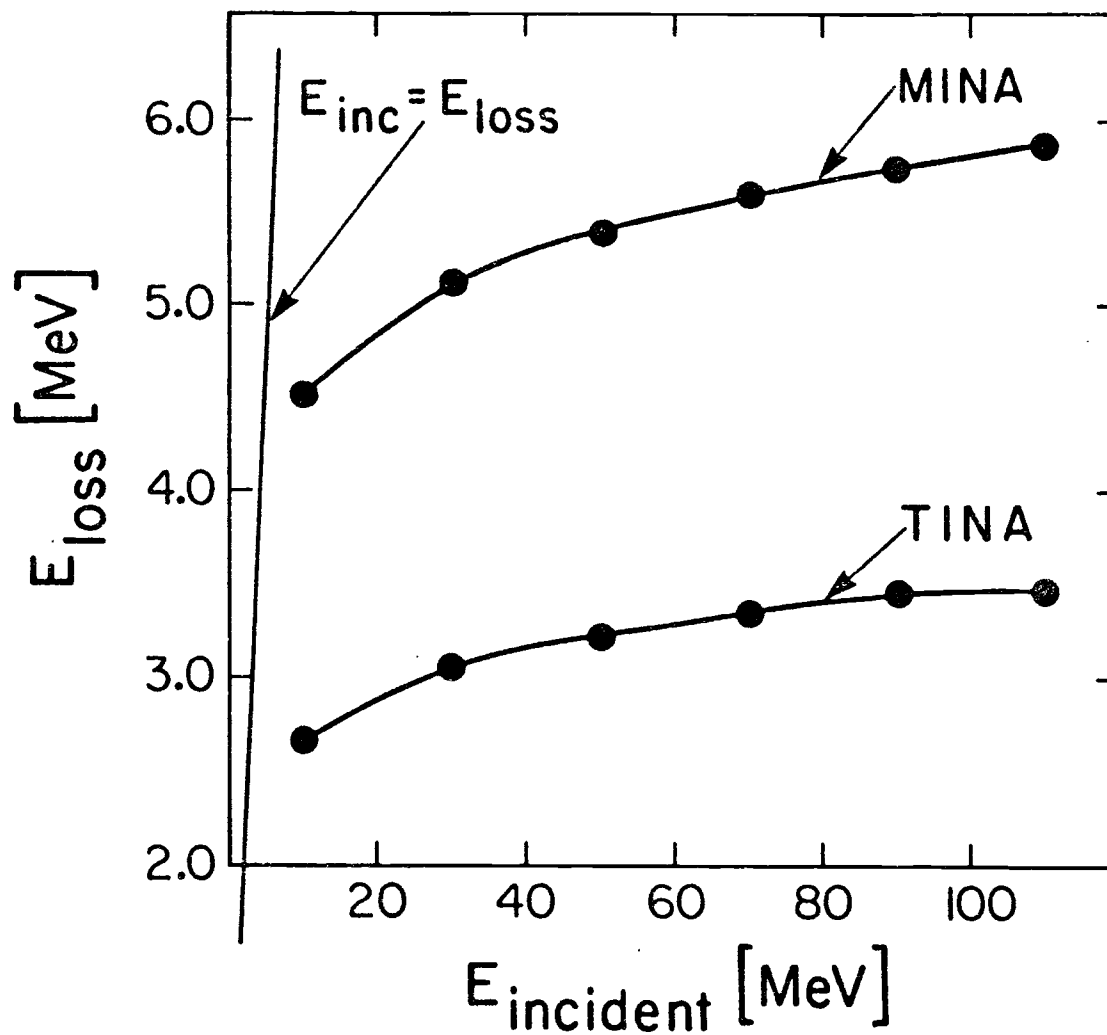


Figure 6.3 Energy loss of electrons in the dead-layers of the NaI crystals

calibration runs. The projected zero is found by simultaneously minimizing the fit of both straight lines through the data points, when the two lines are forced to go through a single point positioned along the horizontal axis:  $E_{dep} = 0\text{MeV}$ . Calculating the difference between measured pedestal and projected zero, we finally obtained the pedestal correction; so essential for the energy calibration with neutrals. This difference is unique, and the same for all data runs, since the gate width was never changed. The gate position relative to the pulse might have been different between in-beam runs and data-taking. However, the change is expected to be small and of negligible effect. The projected zero, together with the centroid of the  $\pi^0$ -box, tied down the energy scale for each run at a 10MeV cut-off, to the order of a few hundred keV.

As it turned out, the three calibration curves (neutrals,  $\pi^+e^+\nu_e$  and in-beam) obtained at the end of the data-taking could not be made to agree. It seemed, that the gain dropped drastically between the last data-taking run, the  $\pi^+e^+\nu_e$  runs and the in-beam energy calibration. The light-pulser on the NaI showed an even larger drop in gain. Since most of the light created by the photo-diode is picked up by the center photo-tube, this indicated that the central tube had faded. Quite some time elapsed between the in-beam energy calibration, the  $\pi^+e^+\nu_e$  runs and the first data-taking at the beginning of the experiment. During this time, we had no information on gain changes. In addition, the light-pulser in TINA displayed a drastic change between in-beam runs and the first data tape. Because of these difficulties and the discrepancies between calibration curves, it was found to be best to calibrate each run with its neutral spectrum. This had the added advantage of automatically correcting for the long term gain drifts. The calibration slope as determined from neutral spectra is shown for TINA in Figure 6.5. The ratio between TINA and MINA  $\pi^0$ -box centroid position is given in Figure 6.6. This ratio should remain constant if the gain change of the NaI crystals during the month long

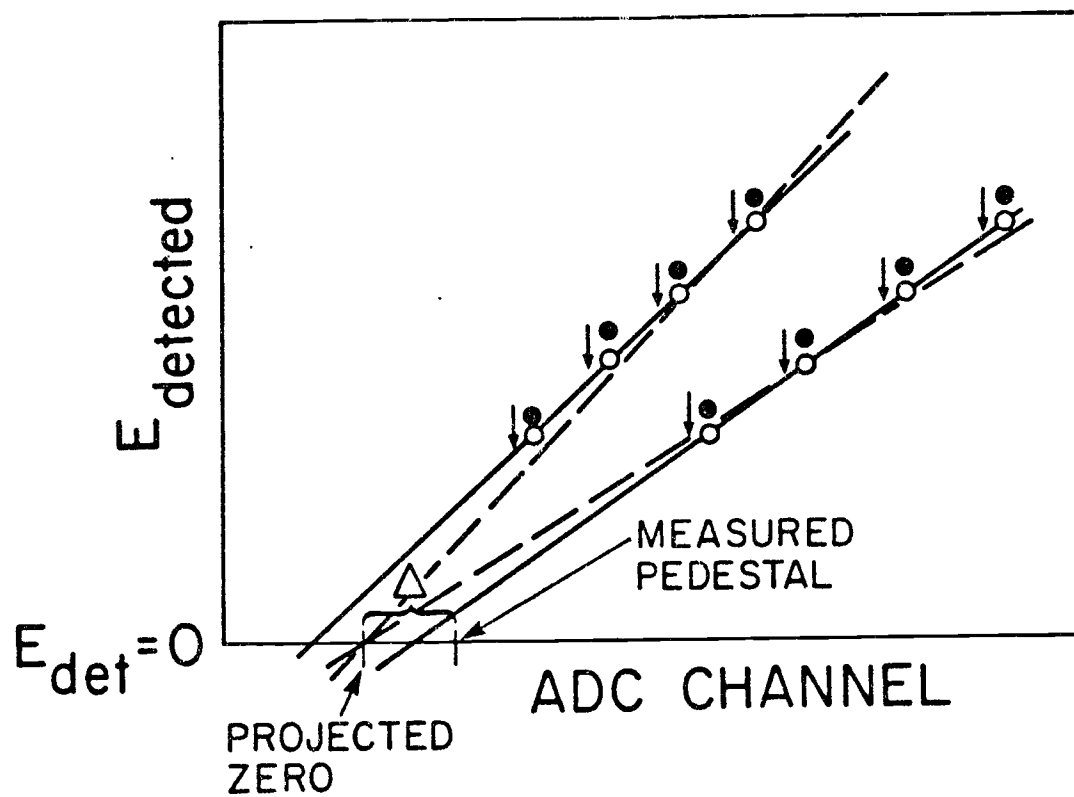


Figure 6.4 Sketch of the method to determine the projected ADC zero

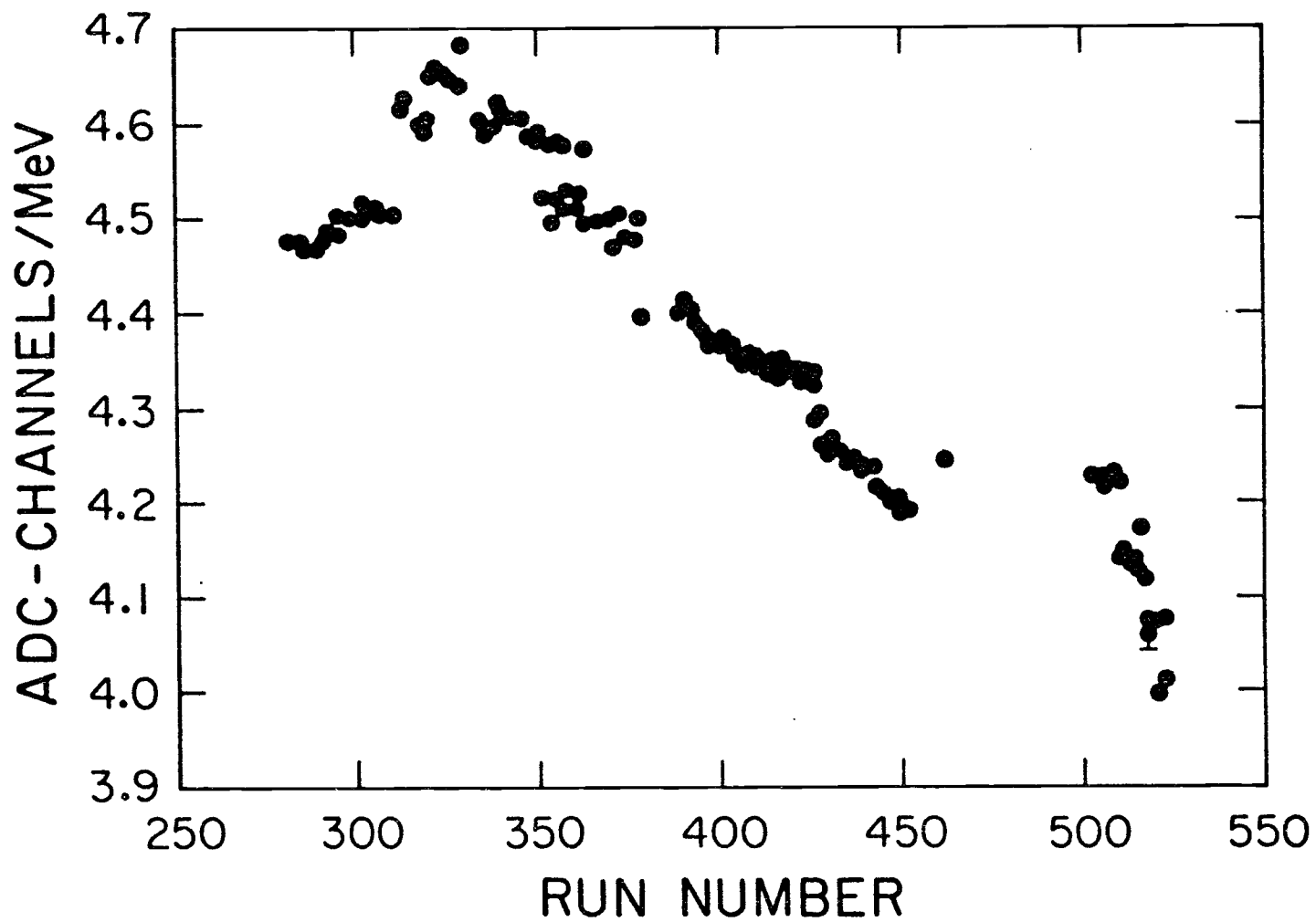


Figure 6.5 TINA energy calibration factor in the equation:

$$\text{ADC-channel} = a * E[\text{MeV}] + b$$

experiment was solely due to a drift in the main power supply or a change in room temperature. There is some variation however, indicating that other factors contributed as well and that possibly individual photo-tubes drifted independently.

#### 6.5.4 Gain stability

The 129MeV peak and the  $\pi^0$ -box in the buffered ADC neutral spectra provided a constant monitor and any short term gain changes could be detected in one minute intervals. With the help of a quick peak searching routine on the 129MeV peak, we observed that there were no short term drifts and that the gains were stable over the counting rates encountered during the  $\pi^0 \rightarrow e^+e^-\gamma$  data taking.

#### 6.6 A large NaI spectrometer as a $\pi^0$ monitor

Instead of counting the 55-83MeV gammas from  $\pi^0 \rightarrow \gamma\gamma$  in SOPHIE, it was more convenient to measure the number of events in the  $\pi^-p \rightarrow n\gamma$  peak and then obtain the number of  $\pi^0$ 's via the Panofsky ratio. Correction for the low energy tail were made according to EGS calculations fitted to the width of the peak.

The measured geometrical acceptance was  $2.89 \cdot 10^{-4}$  of  $4\pi$ . The fraction of gammas expected to be lost by conversion in the material between the target and SOPHIE was 3.0(3)% and EGS calculations indicated that a further factor of 0.984(7) had to be introduced to account for collimator effects and the self-vetoing of the shower exiting the front face of the crystal. The overall acceptance was calculated to be 0.954(8) times the geometrical acceptance.

The acceptance of SOPHIE was determined in a separate measurement by inserting a lead-scintillator sandwich in front of MINA (see Figure 5.3). With this measurement, the number of coincidences between a photon conversion in the lead scintillator and a neutral prompt in SOPHIE with total energy equal to that of the

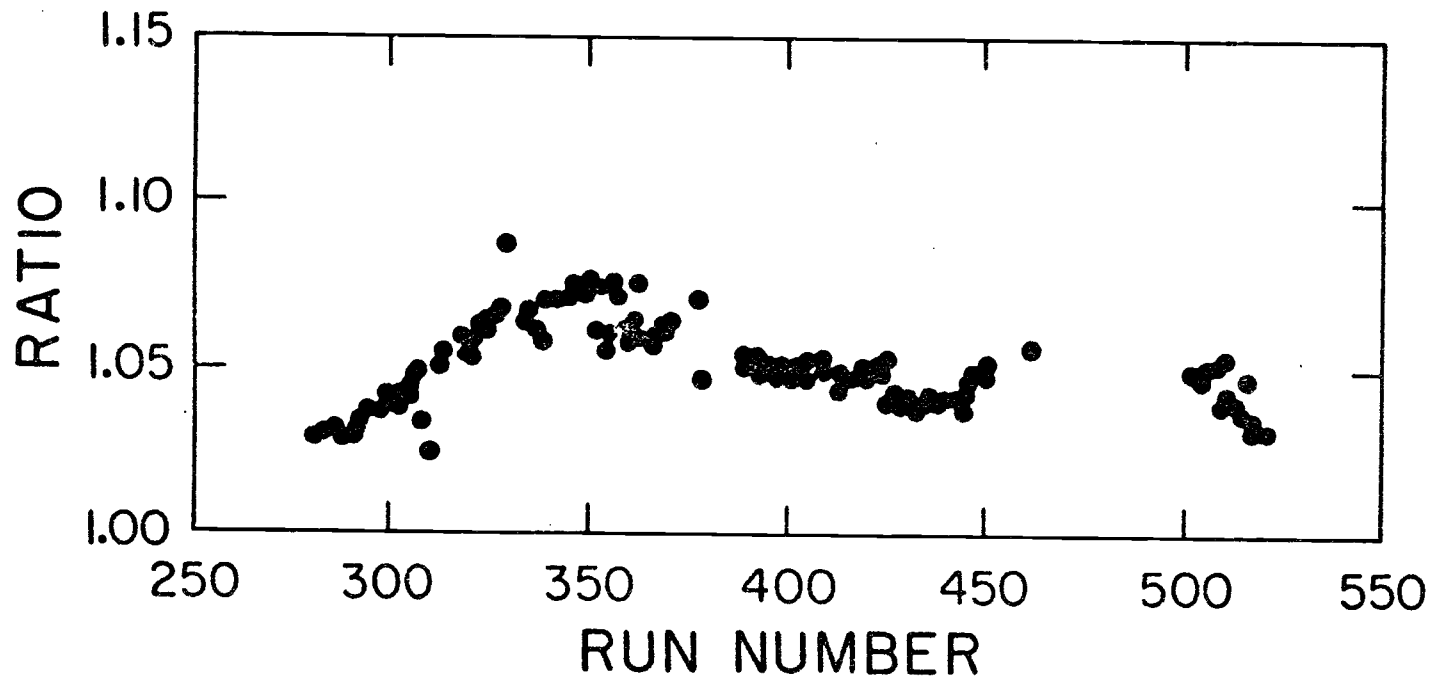


Figure 6.6 Ratio between TINA and MINA  $\pi^0$ -box centroid position

$\pi^0$  (138.27MeV), divided by the number of MINA conversion singles with energy in the  $\pi^0$ -box, can be related to the acceptance of SOPHIE by straight forward kinematic arguments. This was an effective acceptance depending on gamma interactions in the hydrogen target, collimator effects and the threshold set on the veto counters V1 and V2. Both MINA and SOPHIE coincidence spectra were fitted by EGS lineshapes. However, this effective acceptance is precisely the same as when SOPHIE is monitoring  $\pi^0$ 's, the conditions being the same. Analysis produced a value for the ratio of real to geometrical acceptance of 0.944(10) in good agreement with calculations and of the required 1% accuracy.

## 7. MONTE CARLO SIMULATION

In the present  $\pi^0$  form factor experiment, we were looking for a small departure of the observed rate for Dalitz pairs from the rate predicted by quantum electrodynamics alone. The rate is influenced by the geometrical acceptance of the apparatus, the finite resolutions of the various counters and by multiple scattering and energy loss in material traversed by the detected  $e^+e^-$  pairs. This influence is too complicated to be folded into the theoretical spectrum analytically. Thus, we had to resort to a Monte Carlo integration. In addition, there is a kinematically indistinguishable background whose size can only be estimated by a detailed Monte Carlo simulation. The following list outlines the reactions considered:

$$\pi^- p \rightarrow \pi^0 n \quad \pi^0 \rightarrow e^+ e^- \gamma \quad (7.1)$$

$$\rightarrow e^+ e^- \quad (7.2)$$

$$\rightarrow e^+ e^- \gamma \quad \left| \rightarrow e^+ e^-, e^- \right. \quad (7.3)$$

$$\rightarrow \gamma \left| \rightarrow e^+ e^-, e^- \right| \rightarrow e^+ e^-, e^- \quad (7.4)$$

$$\rightarrow e^+ e^- e^+ e^- \quad (7.5)$$

$$\pi^- p \rightarrow e^+ e^- n \quad (7.6)$$

$$\pi^- p \rightarrow n \gamma \quad \left| \rightarrow e^+ e^- \right. \quad (7.7)$$

Modes 7.1 through 7.7 constitute all known processes that contributed to the spectrum of  $e^+e^-$  pairs in the data. It was essential that the program adequately reproduces the dynamics and kinematics of each process, as well as the details of charge and neutral particle propagation through media.

The simulation program was written as the main program for the SLAC EGS code [36]. EGS incorporates multiple scattering, bremsstrahlung and energy loss of electrons, pair production, Compton scattering and the photo-electric effect, and keeps track of all the shower particles. The approximations for electron multiple scattering made in the EGS code were found to be of no appreciable consequence to the precision of the Monte Carlo simulation when compared with the results of a more detailed study. A further investigation of electron pair production in hydrogen showed that only the calculation of the total cross-section for pair production in hydrogen had to be modified in PEGS.<sup>11</sup> The simplified pair production kinematics in the EGS code was also found to be sufficiently accurate to warrant its use in the Monte Carlo program. This argument is mainly based on the fact that subsequent multiple scattering of the created  $e^+e^-$  pair will obliterate the initial situation and dominate the outgoing final directions completely.

Tracking the particles through the experimental geometry was but one task a complete Monte Carlo code had to fulfill. Creating the various decay distributions efficiently was another. In an Appendix, we outline the various sampling techniques employed in the program. The distributions for the invariant mass  $x$  and the energy partition  $y$  for the modes 7.1, 7.5 and 7.6 were taken from detailed quantum electrodynamic calculations [6,38,39]. The radiative corrections, differential in the invariant mass  $x_{vis}$ , could not be established to a meaningful accuracy to justify their inclusion in the sampling distribution [40]. However, their effect on the expected rate was determined and can be corrected for (see chapter 8). For the purpose of calculating the form factor slope, the slope dependent  $\Gamma_{SD}$  and slope independent  $\Gamma_{SI}$  parts of the spectrum in mode 7.1 were generated separately (see chapter 3.3).

The Monte Carlo simulation program was organized in three steps. This structure allowed the use of analysis routines for different purposes, without having to go through the lengthy procedure of

<sup>11</sup> PEGS is the program which generates the media input data for EGS.

creating events each time. First, a theory program decided between the different reactions according to known branching ratios. The different decay channels could be activated or deactivated by the user. In case of mode 7.1, it was possible to sample from pairs where each of the electrons has a minimum energy besides also requiring a minimum opening angle between them. To simulate the Dalitz related background (7.3), these restrictions had to be lifted since the copious small opening angle events contribute as well. The program allowed a preliminary test on the geometrical constraints to speed up the subsequent stages of the Monte Carlo code. This facility could be turned off to permit a more rigorous check on background arising from events where the initial particles did not fulfill the geometrical constraints from the outset but eventually give a valid trigger.

The stopping distribution of  $\pi^-$  in the target was taken from reconstructed experimental events at the  $60^\circ$  geometry. The  $\pi^0$ 's were "created" with a momentum of 28.085 MeV/c and uniform direction in the lab frame. All pertinent information about an event was written to disk and represented the input for the second stage which propagated the particles through the target and the apparatus together with all secondary particles from electron and photon showers. This was done with the help of the EGS code.

For EGS, data files for 10 different media were generated. The media for the wire chambers were homogeneous but tested to be equivalent in their effects on electromagnetic particles to the different MWPC types used in the experiment. In reality, the wire chambers were made up of many layers of different materials but it proved to be uneconomical to simulate them in detail.

To make efficient use of computer time, the tracking of each event was split into three shower regions. The subsequent region was executed only if the trigger condition for the previous region was fulfilled. The logical choice for region 1 was the liquid hydrogen target with its vacuum vessel including the vertical post and all

flanges up to the first MWPC on both detector arms. An event fulfilled the first trigger condition if at least one charge particle crossed the mid-plane of the first wire chamber in each telescope. All shower particles for this event were put on a stack. Particles on the stack represented the input for the next shower region. There, the loop was not only over the initial particles, but over all particles on the stack, each of which could create its own secondary particles. The second trigger condition required one charge particle to go through the defining counter on each side. The last shower region included the layered scintillators and the NaI crystals.

To simulate the energy resolution of the NaI detectors, the deposited energies were smeared by empirical resolution curves for given energy, radius and angle of entry. These curves were previously obtained during in-beam studies (see chapter 6.4). The layered scintillator pulse height distributions for minimum ionizing particles were also obtained from in-beam studies (see chapter 6.1). These distributions were sampled for every charged particle crossing the layered scintillator. This made it possible to simulate pile-up  $e^+e^-$  pairs from gamma conversion.

When a particle crossed a plane of a wire chamber, its coordinates were recorded and written to a file. This file also included the energies deposited in the layered scintillators and the NaI crystals. It acted as the input for the third stage which was equivalent to the analysis program for real data, were it not for multiple hits in the wire chambers and the finite wire chamber resolutions. The wire chamber resolutions were folded in by displacing Monte Carlo generated hits with empirical resolution functions for each chamber and coordinate. In case of a multiple hit in a wire chamber the chamber response had to be mimicked by an equivalent single hit output of the delay-lines. We used the geometrical mean as the single hit equivalent. An additional subroutine returned the delay-line sum corresponding to a multiple hit. This simulation was necessary since the data analysis program

applied a cut on the wire chamber sums in order to eliminate  $e^+e^-$  conversion pairs and the Monte Carlo program has to simulate the efficiency of this procedure correctly (see chapter 6.3). For a multiple hit the sum in x and y are uncorrelated. For a single hit these sums are correlated because the drift time to the anode wire is the same for both coordinates (see Figure 7.1). To map this correlation correctly would have required much computational effort. Instead, we used for single hits an approximation where the two delay line sums were directly correlated, i.e., they were sampled from empirical x and y sum distributions with the same random number. For a multiple hit, the delay-line sums were generated by subtracting from the sum mean the separation of the particles in TDC channels.

After these manipulations, the Monte Carlo events could be processed by the same reconstruction routine that was used for real events. First, the wire chamber hits in each arm were fitted to a straight line and the closest approach of the two lines was calculated. An additional routine optimized the least square distance sum of all the wire chamber hits to two straight lines. These lines were forced to originate from a single point and the optimization was done by varying this point around that of closest approach. In this way a unique value for the pair opening angle was obtained.

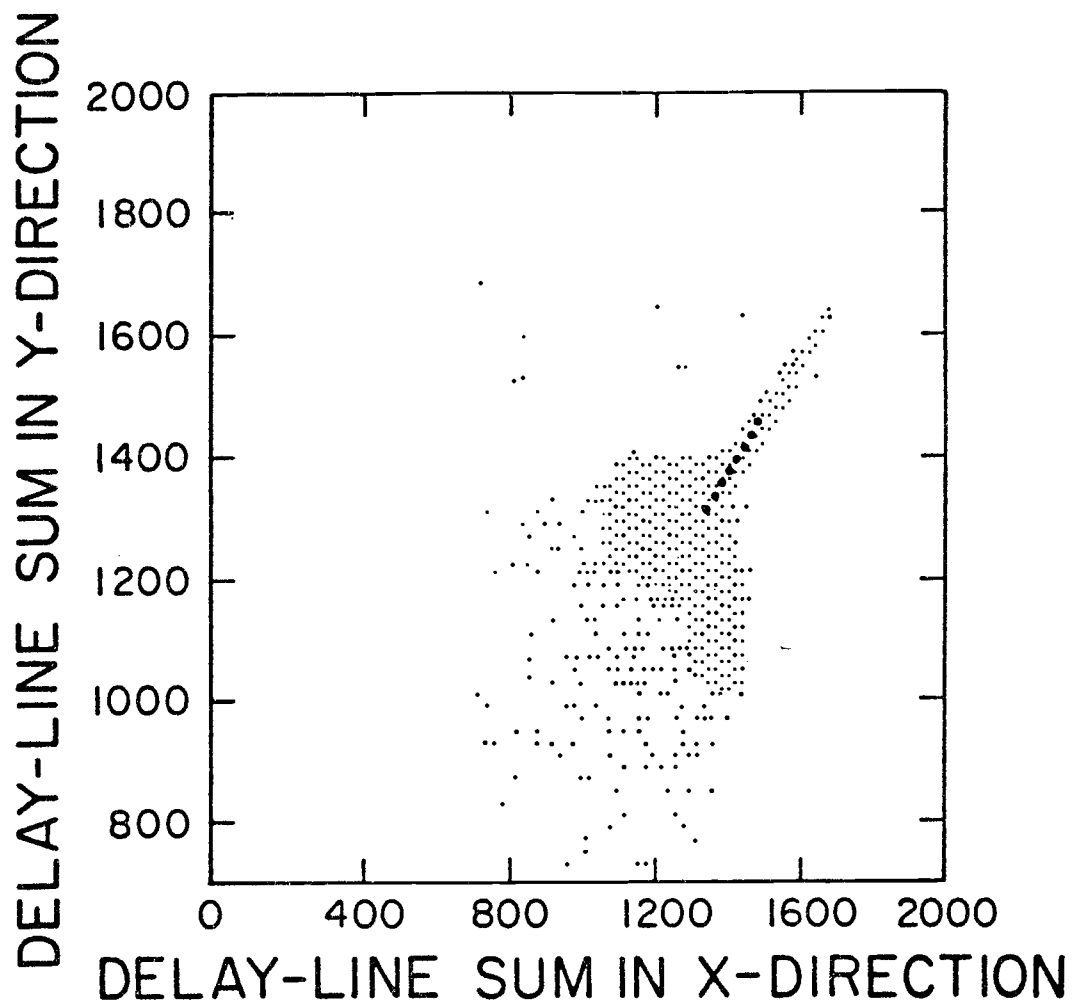


Figure 7.1 Correlation between the delay-line sum in the horizontal and vertical direction for single electrons in the third wire chamber of the TINA-arm.

## 8. RADIATIVE CORRECTIONS

The effect of the electromagnetic transition form factor on the Dalitz decay rate is small. Thus, radiative corrections  $\Gamma_{\text{rad}}$  become important. Radiative corrections to the rate of  $\pi^0 \rightarrow e^+e^-\gamma$  come from two sources: (1) virtual corrections and (2) bremsstrahlung corrections.

$$\Gamma_{\text{rad}} = \Gamma_{\text{virt.}} + \Gamma_{\text{brem}} \quad (8.1)$$

The virtual corrections  $\Gamma_{\text{virt.}}$  come from the interference of the amplitude of diagrams (2) and (3) in Figure 8.1 with the lowest-order amplitude in diagram (1). The bremsstrahlung corrections  $\Gamma_{\text{brem.}}$  involve the squares of the amplitude for the other two Feynman diagrams shown in Figure 8.1 and their counterparts obtained by exchanging the radiative and decay photons. Radiative second order effects change the measured invariant mass distribution in two ways: (1) the momentum of the radiating particle is altered by the emission of a photon and (2) the emitted bremsstrahlung photon may or may not enter the detector.

There has recently been a discussion of the necessity of including in the calculations the interference between the two-virtual photon loop graphs in Figure 8.2 with the lowest order diagram in Figure 8.1 [41]. Since the evaluations of the graphs in Figure 8.2 require a complete knowledge of the  $\pi^0 \rightarrow \gamma\gamma$  "off-shell" form factor, it is clear that the predictions are model dependent. In contrast with the results of reference [41], the analysis in reference [42] shows that these additional terms have factors of  $m_e^2 / m_\pi^2$ . So, even though the interference is of the same order in  $\alpha$  as the radiative corrections previously mentioned, these terms can

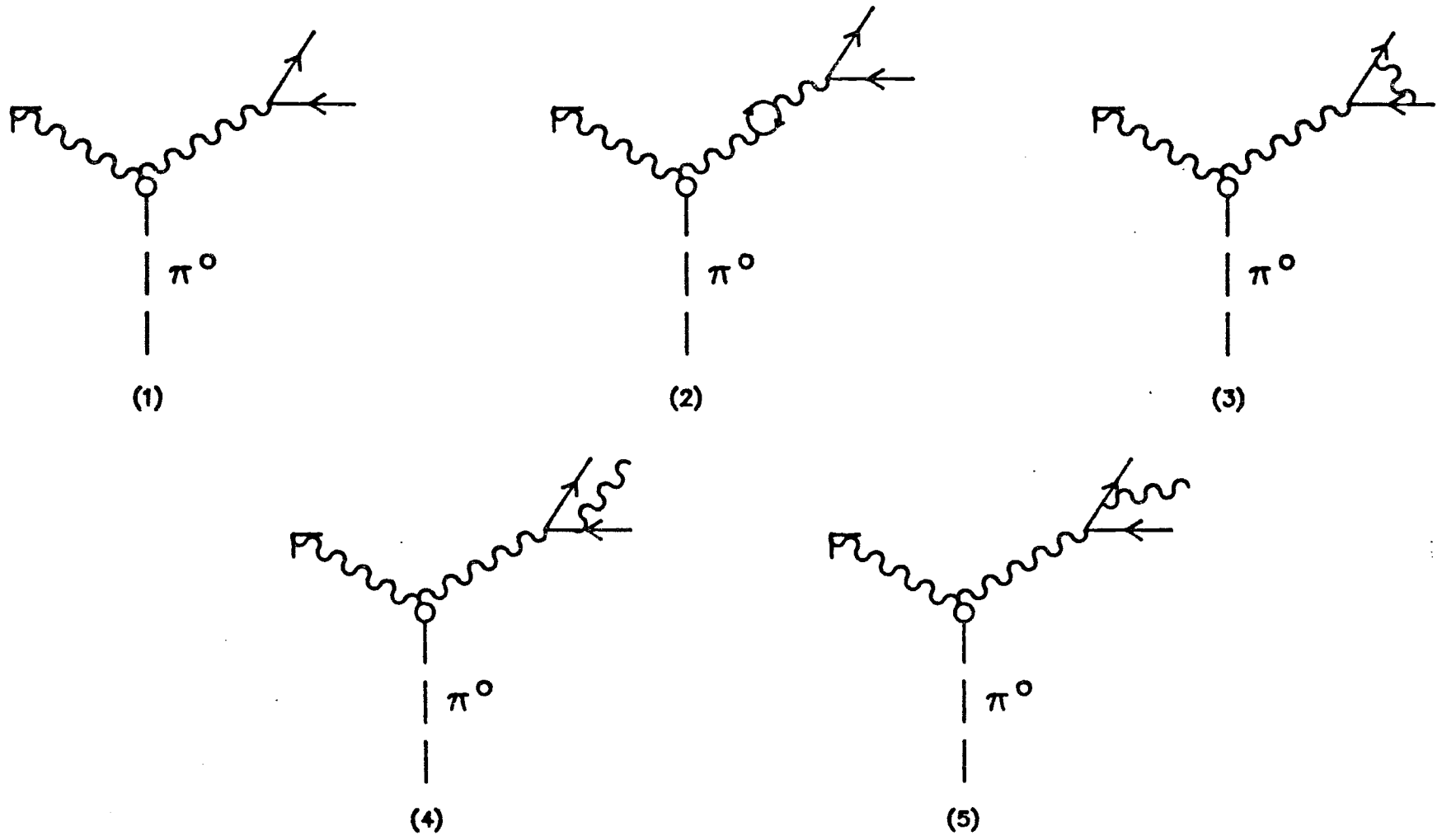


Figure 8.1 One photon diagrams

be neglected. Pending final clarification of the situation, the contributions of diagrams with two virtual photons have not been included in the analysis of this thesis.

The effect of radiative corrections to the total Dalitz decay rate was first calculated by Joseph [43] in the soft photon approximation, ignoring the interference between decay and bremsstrahlung photons. In the paper by Lautrup and Smith [46], based on previous work [44,45], the differential radiative corrections  $d\Gamma_{\text{rad}}/dx$  to the differential decay rate  $d\Gamma_{K+W}/dx$  were calculated in a complete treatment including hard-photon corrections and the interference between photons. In their calculation, terms of the order of  $a * \Gamma_{\text{brem}}$  were neglected, which is surely justifiable since the form factor slope "a" is a small number.

It was not possible to modify the published radiative correction calculations to cover the experimental situation of a limited angular acceptance and the possibility of the direct and/or radiative photon entering the NaI detectors. L. Roberts and J. Smith have therefore developed a general radiative correction program which is suitable for experiments with limited geometrical acceptance [40]. In contrast to the calculations in reference [46], the limited geometrical acceptance requires all integrations to be done numerically. The virtual corrections require simulation of the interference terms over a three-body phase space, whereas the bremsstrahlung corrections require simulation of the square of an amplitude over a four-body phase space. Infrared divergences complicate the situation since they must be canceled before the events are simulated in their separate phase spaces; attempting to cancel the divergences after simulation would be impractical due to numerical round-off error. This difficulty was solved by doing an analytic integration for  $x_{\gamma\gamma}$  (the photon-photon invariant mass) less than some parameter  $\Delta$  of the infrared-divergent terms in the bremsstrahlung corrections and adding them to the virtual corrections. This means that the infrared-divergent terms are

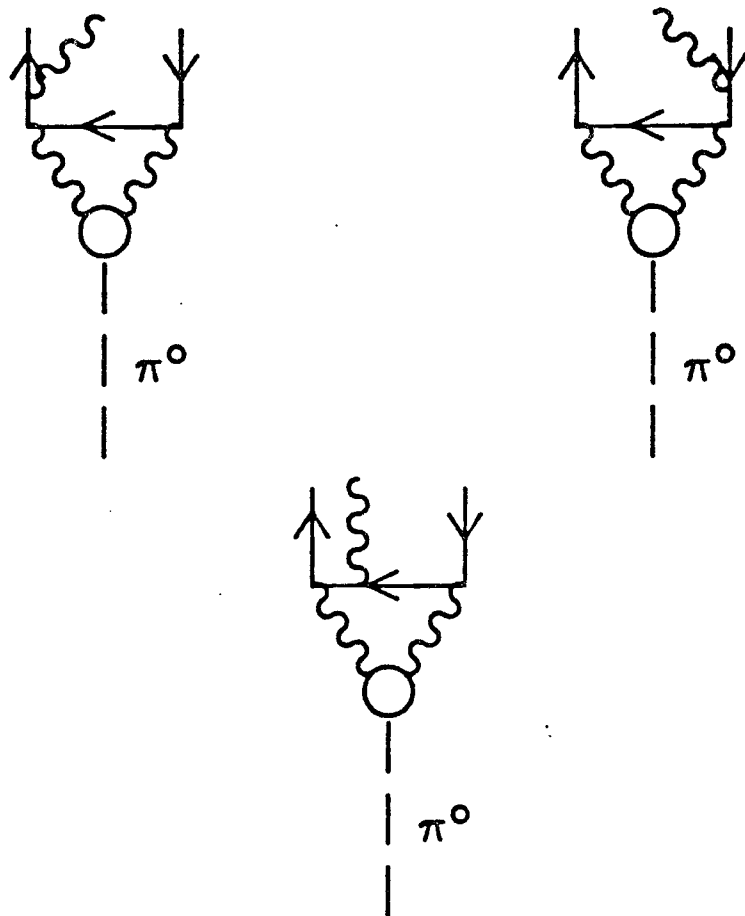


Figure 8.2 Two photon diagrams

exactly canceled, but the virtual correction contains a finite piece of the bremsstrahlung correction depending on  $\Delta$ . It was found, that for reasonable values of  $\Delta$ , the total radiative correction is independent of the ad hoc mathematical parameter  $\Delta$ . For a finite geometrical acceptance, parts of the multi-body phase space are cut out and one would expect the resulting distributions to depend somewhat upon the chosen value of  $\Delta$ . However, for a small value of  $\Delta$ , the calculations show that the radiative corrections to the measured rate are small and of the order of 1%, rendering the residual sensitivity to  $\Delta$  not important.

In the programs written by L. Roberts and J. Smith, the numerical integrations are done by the Monte Carlo technique, and the  $\pi^0$  is assumed to decay at rest. For the  $156^\circ$  detector geometry, the change in rate due to radiative corrections is:

$$\frac{\Gamma_{\text{rad}}(\pi^0 \rightarrow e^+ e^- \gamma)}{\Gamma_{\text{K+W}}(\pi^0 \rightarrow e^+ e^- \gamma)} \Bigg|_{\pi^0 \text{ at rest}}^{156^\circ} = \frac{\Gamma_{\text{virt.}} + \Gamma_{\text{brem.}}}{\Gamma_{\text{K+W}}} = -0.2\% \pm 0.3\% \quad (8.2)$$

The error in this prediction is statistical and due to the fact that  $\Gamma_{\text{virt.}}$  and  $\Gamma_{\text{brem.}}$  have opposite sign and one is in effect looking for the difference of two almost identical Monte Carlo distributions. The result in (8.2) was obtained after 5 hours of CPU-time on a VAX 8600. For the  $130^\circ$  and  $60^\circ$  geometry the result is:

$$\Gamma_{\text{rad}} / \Gamma_{\text{K+W}} \Bigg|_{130^\circ; \pi^0 \text{ at rest}} = +0.5\% \pm 0.4\% \quad (8.3)$$

$$\Gamma_{\text{rad}} / \Gamma_{\text{K+W}} \Bigg|_{60^\circ; \pi^0 \text{ at rest}} = +0.8\% \pm 0.1\% \quad (8.4)$$

Including the finite momentum of the  $\pi^0$  (28.085 MeV/c) in the calculation increases the dimension of the Monte Carlo integration from 5 to 7 for both the lowest order diagram and the virtual corrections and from 8 to 10 for the bremsstrahlung term. With all

ten dimensions, it was not possible to obtain convergence of the Monte Carlo result for the bremsstrahlung term. The limiting cases of the  $\pi^0$  moving toward, away or perpendicular to a NaI-detector were therefore investigated separately.

For the different  $\pi^0$  directions considered, the result for the  $156^\circ$  geometry changed from  $(-0.7 \pm 0.3)\%$  to  $(+0.5 \pm 0.2)\%$ . We felt therefore justified to assume that the  $\pi^0$ -momentum, averaged over all possible directions, will result in a final value close to the one calculated for the  $\pi^0$  at rest. In view of the error-bars in eq. 8.2, it is impossible to give meaningful values for the differential radiative correction  $d\Gamma_{\text{rad}}/dx_{\text{vis}}$ .  $x_{\text{vis}}$  is the measured apparent invariant mass of the lepton pair.

In summary, the radiative corrections to the detected rate do not exceed 1% and are of the same order as the expected experimental errors. This result is in strong contrast to the analysis of the recent CERN experiment [22], for which the radiative corrections were found to change the value of the slope parameter "a" by a factor of two.

## 9. FINAL EVENT ANALYSIS

The normalization between Monte Carlo simulation and experiment has to be known precisely in order to determine the form factor slope from a rate measurement. Pile-up from multiple  $\pi^-$ 's in the target is not simulated in the Monte Carlo program. So, any additional rate due to this possibility can only be estimated from TRIUMF's beam structure and the gate-width of the ADC's. Furthermore, a clean data sample, free of background from processes not included in the Monte Carlo has to be extracted from the original data tapes. These three tasks are outlined in this chapter.

### 9.1 Overall normalization

The line shape parameters for SOPHIE were obtained by fitting the NaI response function (6.1) to the 129MeV gamma-peak from  $\pi^-p \rightarrow n\gamma$ . With these parameters, the area underneath the curve between 75% and 120% of the peak was calculated to be 98.97% of the total integral. As a consequence of this analysis, we determined the overall normalization by simply counting the number of events between these boundaries in the SOPHIE neutral spectrum,  $N_{\text{SOPHIE}}$ . With SOPHIE's acceptance for neutrals ( $0.984 \cdot 2.891 \cdot 10^{-4}$ ), determined by the methods outlined in chapter 6.6, and the Panofsky ratio (1.546) [33], it is a straight forward calculation to establish the number of  $\pi^0$ 's in the target.<sup>12</sup>

$$N_{\pi^0 \text{tgt}} = 5.530 \cdot 10^3 * N_{\text{SOPHIE}} \quad (9.1)$$

<sup>12</sup> Some care has to be taken when using the Panofsky ratio since it relates the total electromagnetic channel to the strong channel  $\pi^-p \rightarrow \pi^0 n$  and not only  $\pi^-p \rightarrow n\gamma$ , i.e., there is a 0.71% contribution to the E&M channel from  $\pi^-p \rightarrow e^+e^-n$ .

Since not all six wire chambers and layered scintillators were 100% efficient, the actual number of Monte Carlo simulated events had to be reduced by the total combined efficiency of all the detectors.

When the Monte Carlo  $\pi^- p \rightarrow e^+ e^- n$  events were analysed with the final analysis routine, it was found that 3.71% of the events were rejected by the cuts on MWPC delay-line spectra. A closer investigation revealed that in these cases more than one electron was present in one of the six wire chambers. Thus, we did not determine, by the method outlined in chapter 6.3, the efficiency of the wire chambers to single charge particles, but rather to a particular kind of reaction. To correct for this, the overall efficiency of all the MWPC's and thus the number of Monte Carlo trials was increased by 3.71%.

For a given geometry, the total number of "detectable"  $\pi^0$ 's in the target,  $N_{\text{det}} \pi^0$ , is the sum over all runs included in the analysis.

$$N_{\text{det}} \pi^0 = \sum_i N_{\text{det}} \pi^0_i = s * \sum_i \epsilon_i N_{\text{SOPHIE } i} \quad (9.2)$$

where  $s=5.530*10^3$  and

$$\epsilon_i = \prod_k^{12} \epsilon_k \quad (9.3)$$

The product includes all six wire chamber and layered scintillator efficiencies.

Only runs were considered in the final analysis which gave a consistent ratio of  $N_{\text{det}} \pi^0_i / N_{\text{SOPHIE } i}$  (see Figure 9.1). Furthermore, runs were excluded where one of the wire chambers was operating at a low (<95%) efficiency. In addition, all runs were discarded for which extraordinary comments were found in the run-book. These included: poor SOPHIE energy spectrum, unsteady beam, acting up of wire chambers, poor RF spectrum and other technical problems. Since data taking at 156° was stretched over a long period of time, interrupted by other measurements, it was regarded to be of little statistical disadvantage, if the analysis

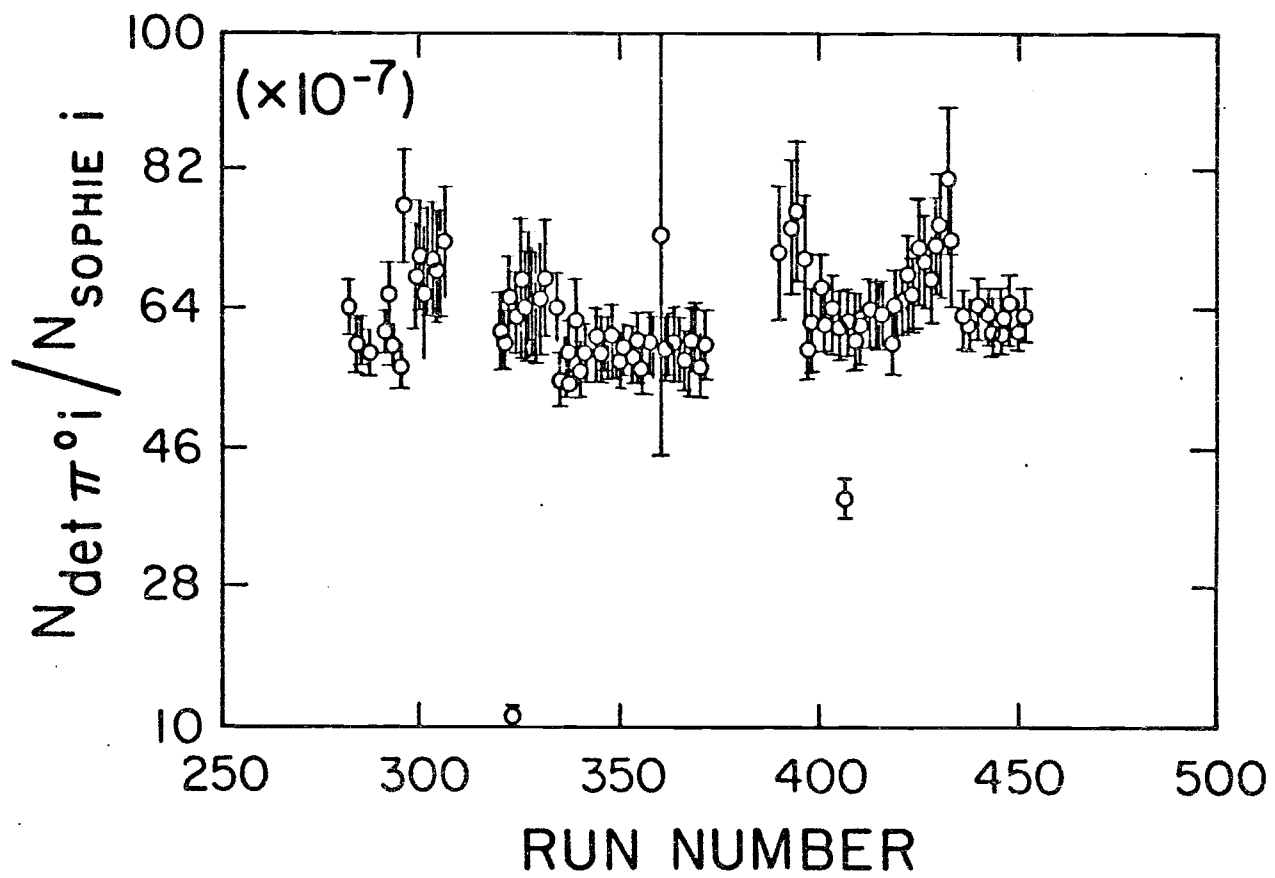


Figure 9.1 Variation of  $N_{\text{det } \pi^0_i} / N_{\text{SOPHIE}_i}$  during the run

was restricted to consecutive runs towards the end of the experiment.

With these various considerations applied to every individual run, we were left with  $1.71 \cdot 10^{10}$  "detectable"  $\pi^0$ 's in the target at  $156^\circ$ ,  $7.95 \cdot 10^9$  at  $130^\circ$  and  $1.099 \cdot 10^{10}$  at  $60^\circ$ . The accuracy of the SOPHIE normalization,  $\Delta s/s$ , was established to be 1.2% (see chapter 6.6).<sup>13</sup>

Nevertheless, the total normalization errors are slightly different for the three geometries because of the statistical nature of the detector efficiency measurements. Every efficiency of every run has an estimated statistical error attached to it. Combining all uncertainties according to:

$$\left( \frac{\Delta N_{\text{det } \pi^0}}{N_{\text{det } \pi^0}} \right)^2 = \left( \frac{\Delta s}{s} \right)^2 + \frac{\sum_i (\epsilon_i N_{\text{SOPHIE } i} (\Delta \epsilon_i / \epsilon_i))^2}{\left( \sum_i \epsilon_i N_{\text{SOPHIE } i} \right)^2} \quad (9.4)$$

where

$$\left( \frac{\Delta \epsilon_i}{\epsilon_i} \right)^2 = \frac{1}{\sum_k} \left( \frac{\Delta \epsilon_{ik}}{\epsilon_{ik}} \right)^2$$

and

$$\Delta \epsilon_{ik} = \left( \frac{\epsilon_{ik}(1-\epsilon_{ik})}{N_{ik}} \right)^{1/2}$$

( $N_{ik}$  is the number of sample events used to determine the efficiency  $\epsilon_{ik}$ ); we obtained the following errors for the total number of "detectable"  $\pi^0$ 's in the target: 1.2% at  $156^\circ$ , 1.8% at  $130^\circ$  and 1.4% at  $60^\circ$ .

We used a highly efficient Monte Carlo sampling routine for Dalitz events (see Appendix), which allowed us to specify the minimum opening angle  $\theta_{\text{min}}$  of the lepton pair, the minimum energy of the

13

The error in the experimental result of the Panofsky ratio, 0.6%, increases the normalization error of SOPHIE by 0.2% over the estimate in chapter 6.6. The statistical error in  $N_{\text{SOPHIE } i}$  is negligible in comparison

electrons  $E_{\min}$  and  $X_{\min}$ . With this routine, it was not necessary to simulate all the probable Dalitz decays but only those which resulted in events with  $\theta > \theta_{\min}$ ,  $E > E_{\min}$  and  $X > X_{\min}$ . Events below these thresholds had no chance either to survive the geometrical constraints or the final data analysis. The rate of these events is only a fraction  $R(\theta_{\min}, E_{\min}, X_{\min})$  of the total number of Dalitz events. This fraction was obtained by a numerical integration of eq. A.2 for given  $\theta_{\min}$ ,  $E_{\min}$  and  $X_{\min}$ , when compared to the total branching ratio. At  $156^\circ$  we used:  $\theta_{\min} = 100^\circ$ ,  $E_{\min} = 2.5\text{MeV}$  and  $X_{\min} = 0.05$ ; at  $130^\circ$ :  $\theta_{\min} = 75^\circ$ ,  $E_{\min} = 2.5\text{MeV}$  and  $X_{\min} = 0.05$ ; and at  $60^\circ$ :  $\theta_{\min} = 0^\circ$ ,  $E_{\min} = 2.5\text{MeV}$  and  $X_{\min} = 0.05$ . With these values for  $\theta_{\min}$ ,  $E_{\min}$  and  $X_{\min}$ , the aforementioned ratio  $R(\theta_{\min}, E_{\min}, X_{\min})$  is 0.0777 at  $156^\circ$ , 0.1275 at  $130^\circ$  and 0.1710 at  $60^\circ$ .

Since the "structure dependent"  $\Gamma_{SD}$  and the "structure independent"  $\Gamma_{SI}$  part of the spectrum were simulated separately, the corresponding number of Monte Carlo trial events had to be properly normalized by the following relation:

$$\# \text{ M.C. trials}_{\Gamma_{SD}} = (\Gamma_{SI} / \Gamma_{SD}) * \# \text{ M.C. trials}_{\Gamma_{SI}} \quad (9.5)$$

where  $\Gamma_{SI}$  and  $\Gamma_{SD}$  are, for given  $\theta_{\min}$ ,  $E_{\min}$  and  $x_{\min}$ , numerical integrals of eq. A.2 and eq. A.2 multiplied by  $x$ , respectively. We obtained:  $\Gamma_{SD}/\Gamma_{SI} = 0.2287$  at  $156^\circ$ ,  $\Gamma_{SD}/\Gamma_{SI} = 0.1844$  at  $130^\circ$  and  $\Gamma_{SD}/\Gamma_{SI} = 0.1556$  at  $60^\circ$ .

A similar numerical integration of  $d\Gamma/dx$  ( $\pi^- p \rightarrow n e^+ e^-$ ) given by expressions in ref. [38] resulted in:

$$R(x_{\min}) = \frac{\Gamma(x_{\min} > 0.05, a_{\pi^-} = 0.03)}{\Gamma(x_{\min} > 0, a_{\pi^-} = 0.03)} = 0.2775 \quad (9.6)$$

Here,  $a_{\pi^-}$  is the charge pion form factor slope. Its value, 0.03, is a world average of all published estimates.

For some of the Monte Carlo events ( $\pi^0 \rightarrow e^+ e^- \gamma$ ,  $\pi^- \rightarrow p^+ e^- n$ ), the positron direction was forced to be in a cone with half-angle  $26^\circ$  around either TINA or MINA. This restricts the solid angle ( $\Omega$  of  $e^+$ ) to 10.13% and allows a further diminution in the number of required Monte Carlo trails for these reactions. Obviously, this restriction on the positron direction had to be lifted for the estimate of the background from  $\pi^0 \rightarrow \gamma\gamma$  and  $\pi^0 \rightarrow e^+ e^- e^+ e^-$ .

To increase the rate with which valid background events from gamma-conversions are produced in the Monte Carlo, the conversion probability for each photon was increased by a factor of 10, by artificially decreasing the mean free path in LH<sub>2</sub> and Mylar. This gives a reduction in needed Monte Carlo trials by a factor  $F_\gamma = 10 \cdot 10 = 100$  for  $\pi^0 \rightarrow \gamma\gamma \rightarrow e^+ e^-$  pairs and a factor  $F_\gamma = 10$  for either Dalitz related background or  $\pi^- \rightarrow p^+ n \gamma \rightarrow e^+ e^-$  pairs. Immediately after the event of a photon conversion in the program, the mean free path was set back to its real value, so that the electron showers weren't wrongly propagated in excessively dense media.

Dalitz related background was simulated by sampling the complementary phase-space than was done for direct Dalitz pairs, i.e.,  $\theta < \theta_{\min}$ ,  $E < E_{\min}$  and  $X < X_{\min}$ , assuming  $a_\pi = 0$ . Here, the positron direction is also no longer constrained to a finite solid angle around the detectors. The ratio of Dalitz related background to the total Dalitz spectrum  $R(x_{\min}, E_{\min}, X_{\min})$  is just one minus the ratio given for the direct Dalitz pairs.

In summary, the number of Monte Carlo trials for each event type and geometry is given by:

$$\# \text{ M.C. trials} = N_{\text{det}} \pi^0 * \text{BR} * R(\theta_{\min}, E_{\min}, x_{\min}) * (1/F_\gamma) * (\Omega \text{ of } e^+) \quad (9.7)$$

where  $\text{BR} = 1 * 0.0184$  for  $\pi^0 \rightarrow e^+ e^- \gamma$

$$\text{BR} = 0.6468 * 0.0071 \text{ for } \pi^- \text{p} \rightarrow e^+ e^- n$$

$$\text{BR} = 1 * 0.9816 \text{ for } \pi^0 \rightarrow \gamma\gamma$$

$$\text{BR} = 2 * 10^{-7} \text{ for } \pi^0 \rightarrow e^+ e^-$$

$$\text{BR} = 3.28 * 10^{-5} \text{ for } \pi^0 \rightarrow e^+ e^- e^+ e^-$$

$$\text{BR} = 0.6468 \text{ for } \pi^- \text{p} \rightarrow n\gamma$$

(Unless applicable, the factors  $R(\theta_{\min}, E_{\min}, x_{\min})$ , ( $\Omega$  of  $e^+$ ) and  $F_\gamma$  are equal to 1.)

The comparatively large systematic errors in the form factor slope (see chapter 10), made it unnecessary to simulate more events in the Monte Carlo than were present in the data. However, some of the background events would have had an excessive CPU-time requirement on a VAX 8600 if they had been simulated to the full experimental statistics. Since in all cases, they were only a small contribution to the total rate, a fraction of these Monte Carlo events was sufficient to determine "a" without much loss in statistical error. For this reason, only 50% of the  $\pi^0 \rightarrow \gamma\gamma$  and the Dalitz related background events were simulated. For Double Dalitz decay, the numbers are 20%, 10% and 40%, in case of the  $156^\circ$ ,  $130^\circ$  and  $60^\circ$  geometry, respectively. For single photon conversion at  $60^\circ$ , we simulated only 10% of  $\pi^- \text{p} \rightarrow n\gamma$  and  $\pi^0 \rightarrow \gamma\gamma$  events. At the  $130^\circ$  and  $156^\circ$  geometries, single photon conversion contributes nothing to the spectrum, as wide opening angle pair production is very improbable.

## 9.2 Background from $\pi^-$ pile-up in the target

Another possible source of background is due to pile-up of unrelated charged particles. This background is rate dependent and can be estimated from TRIUMF's beam structure. With a maximum stopping rate of about 400kHz in the LH<sub>2</sub> target and a cyclotron frequency of 23MHz, the number of beam bursts per stopped  $\pi^-$  is:

$$\frac{\text{Beam burst}}{\pi^- \text{ stop}} = \frac{23\text{MHz}}{400\text{kHz}} = 57.5 \quad (9.8)$$

Thus, the probability of a second  $\pi^-$  stopping per beam bucket once one  $\pi^-$  has already stopped, is 1/57.5. Combining the probabilities for two  $\pi^-$ 's producing charge particles through either  $\pi^0 \rightarrow e^+ e^- \gamma$ ,  $\pi^- \rightarrow p^+ e^- n$  or a mixture of both, we obtain  $10^{-4}$  for the probability of creating four electrons/positrons. Furthermore, geometrical arguments based on the results for the coincidence rate of Dalitz and internal conversion pairs from Monte Carlo simulation, lead us to the conclusion, that the probability for a charge-charge coincidence with four electrons is about  $3 \cdot 10^{-3}$ .<sup>14</sup> After multiplying these probabilities it becomes clear that the expected background from charge particle creation in the target by multiple pions is exceedingly small when compared to the number of six wire chamber events. The numbers are: 85/103000 at  $156^\circ$ , 20/46000 at  $130^\circ$  and 25/91500 at  $60^\circ$ .

Similar arguments can be made to investigate the probability of an all neutral event piling up on a charge particle pair. A consequent external gamma-conversion can then also contribute to the charge-charge coincidence rate. As it turns out, even without photon conversion, this pile-up is only by about a factor of 2-3 more likely than the one considered above and can be neglected as well.

The pile-up rate of two all neutral events from different  $\pi^-$  in the target is about  $4 \cdot 10^{-5}$  of the single neutral event rate. However, neutral events are by a factor of 100 more copious than charged events. Nevertheless, the required external gamma-conversion probability and subsequent identification of a single neutral event as a charge-charge coincidence,  $5 \cdot 10^{-5}$  at  $156^\circ$ , also reduces this background to a negligible amount.

In summary, pile-up events from multiple stopped  $\pi^-$ 's in the target contribute virtually nothing to the detected charge coincidence rate.

<sup>14</sup> The dependence of this number on detector geometry is small and negligible on the scope of the desired estimate from this treatise.

### 9.3 Event selection

The original data tapes were first skimmed for charge-charge coincidences. In a second iteration, the data was further reduced by demanding that all six MWPC's had triggered. Furthermore, only when all wire chamber hits were inside an aperture defined by the lead collimator, was the event considered for further analysis. These criteria reduced the data sample by 97.2% at  $156^\circ$ , 92.5% at  $130^\circ$  and 71.2% at  $60^\circ$ , reflecting a relative high trigger rate from photon conversions in front of the defining counters and in the lead collimator whenever the acceptance for  $\pi^0 \rightarrow \gamma\gamma$  coincidences was large, i.e., for large detector opening angle.

For these "genuine" six wire chamber events, an opening angle between the detected pair was determined and stored on tape, together with other event information such as ADC and TDC outputs for the layered scintillators, TINA/MINA pulseheight and timing information, MWPC delay-line sum spectra, the time of the event relative to the cyclotron pulse and parameters reflecting the goodness of the track through the wire chamber hits. This approach reduced the number of tapes further, but it also retained some flexibility for the remaining analysis, since at this stage, cuts on the above event parameters were not yet established.

The Monte Carlo simulation predicts a low energy region in the E-MINA vs. E-TINA scatter-plot (see Figure 9.2), which is completely free of Dalitz events and contains hardly any events from all other simulated background processes. It was therefore clear, that a cut on this region would mainly reject events which are not accounted for in the Monte Carlo program. For small energies, we discarded events below a semi-circle shown in Figure 9.2. This cut is slightly more restrictive, so that some of the simulated events are also lost. Thus, the very same cut had to be applied on the Monte Carlo result. Any event in the data sample above the  $\pi^- p^+ e^- n$  region (in Figure 9.2) is likely due to pile-up of a neutral particle, for instance one of the many neutrons present in the experimental area, on the

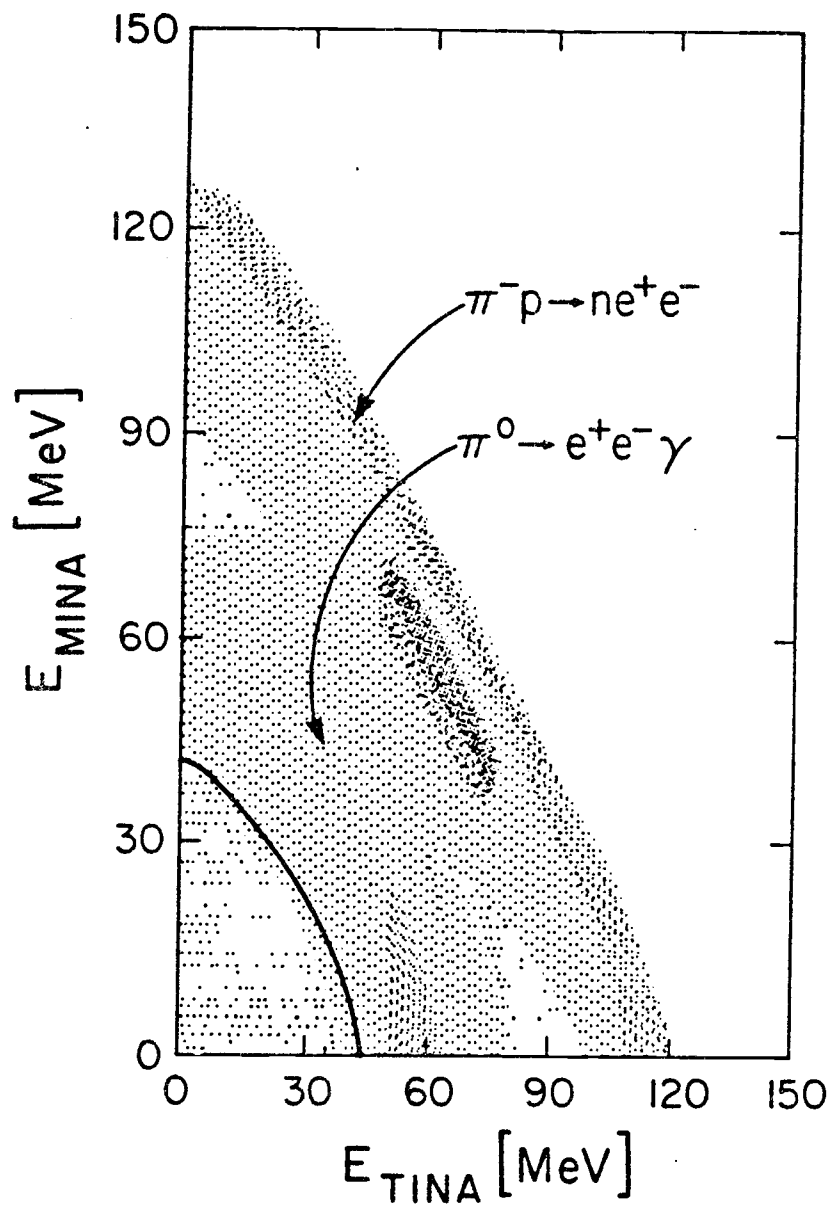


Figure 9.2 Monte Carlo result for the  $156^\circ$  geometry of  $E_{\text{MINA}}$  vs.  $E_{\text{TINA}}$

energy measurement of a good charge-coincidence. No cut was applied on these events.

There were two more cuts at our disposal, which did not need to be investigated further. Actually, they had to be applied to the data in exactly the same way as they were defined during the wire chamber efficiency determination. These included a cut on the minimum sum in each delay-line as well as a cut on the correlation between the delay-line sums in the two orthogonal directions. Both cuts were designed to eliminate  $e^+e^-$  pairs from external conversions (see chapter 6.3). We did not apply cuts on the layered scintillator energy spectra for reasons mentioned in chapter 6.1. However, we demanded that the signals in both defining counters were in time with each other and the beam counter B3.

The effect of the remaining four cuts on the result for the  $\pi^0$  form factor had to be studied in more detail. These included cuts on the minimum recorded energy in the two NaI detectors, on individual straight tracking through each set of three MWPC's, on closest approach when the tracks were extrapolated back to the target and on the reconstructed interaction point. It turned out, that the cuts on interaction point and closest approach are both very sensitive to even small discrepancies between the simulated wire chamber resolutions and the actual resolution. We decided therefore, not to cut on closest approach and to apply a cut on interaction point only if it did not interfere with the simulated stopping distribution. At  $130^\circ$ , some events were left in the data sample which obviously had come from the target post and were clearly outside the Monte Carlo stopping distribution. Thus, a cut on target position was both necessary and possible at  $130^\circ$ . We could not identify events in the  $156^\circ$  data sample which had clearly come from the post. Quite contrary, the region of the post is free of any events even though the resolution of the MWPC's creates, at this geometry, an elongated halo around the target (see Figure 9.3). This halo was also reproduced in the Monte Carlo study. For this reason, no cut on interaction point was used for the  $156^\circ$  data. We also avoided a cut on target position at  $60^\circ$ , since no events were found to come

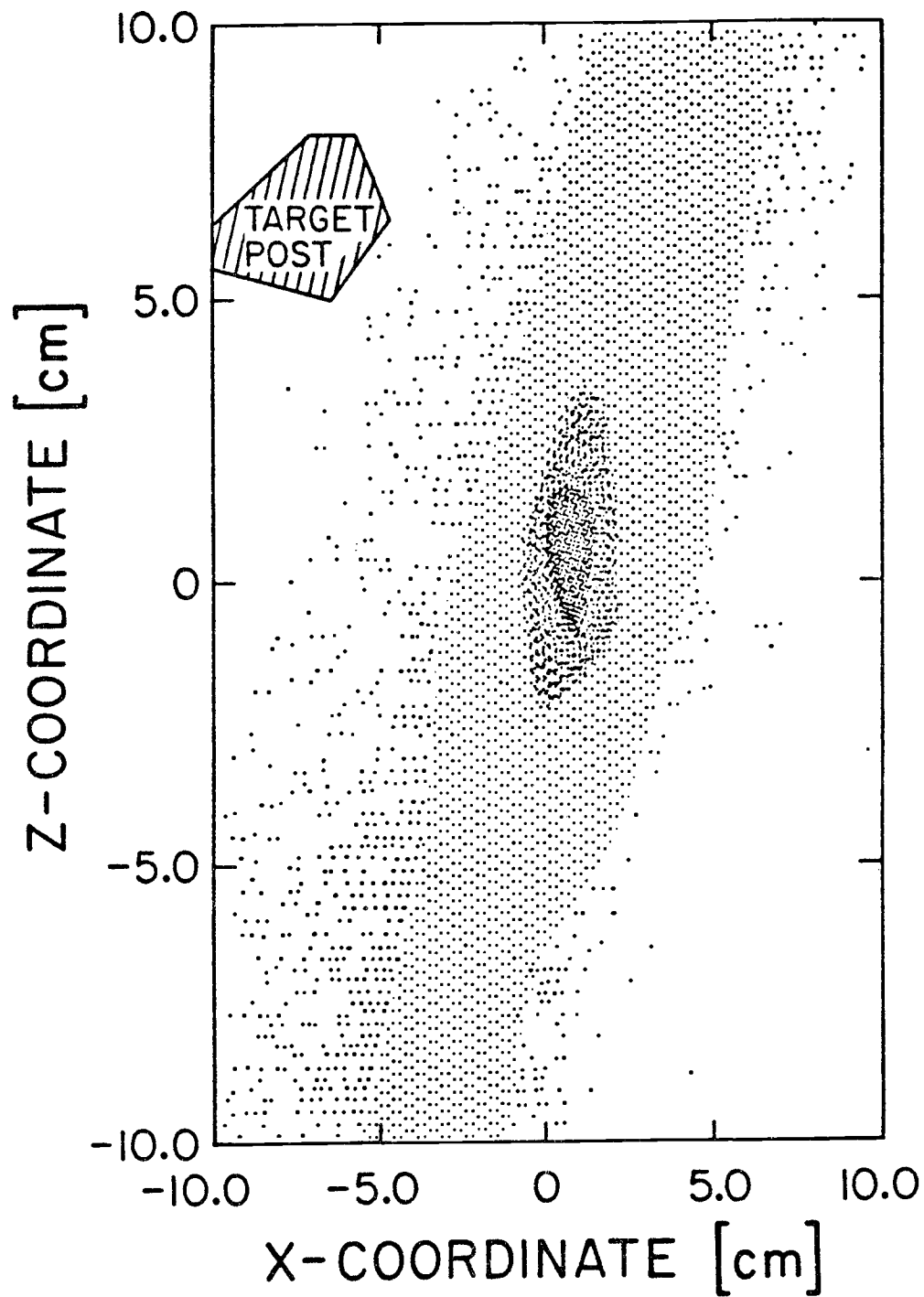


Figure 9.3 Measured stopping distribution in the target (X vs. Z).  
Z points along the  $\pi^-$  beam and X is positive on TINA's side.

from outside the target. Incidentally, at  $130^\circ$  some events were clearly not associated with pions from the beam and could be eliminated by a cut on timing relative to the primary proton pulse. At both  $156^\circ$  and  $60^\circ$ , no such events were seen.

Finally, we had to verify that the result for "a" is insensitive to the exact value of the minimum energy cut and that it is also stable over a wide range of cuts on individual straight tracking. Let us now concentrate on the  $130^\circ$  data. The straight line parameter is called DIFMAX and it is defined as the maximum difference (in cm) between a hit in a MWPC and its intersection with a fitted line through all three chambers. For a very tight cut (CUTMAX) on this parameter, resolution uncertainties come into play again and fewer events survive in the data sample than is the case for the Monte Carlo. For reasonable values of CUTMAX, above 0.3cm, the result for "a" remains constant within the error-bars. Only at large CUTMAX ( $>1.0\text{cm}$ ), do background events with poor tracking come into the spectrum and thus increase the result for "a". As a compromise, we chose 0.5cm for CUTMAX.

Our final task was now to verify that "a" does not change for a range of cuts applied on the minimum energy recorded in the two NaI detectors,  $E_{\min}$ . This is shown in Figure 9.4. At small values of  $E_{\min}$ , the value of "a" calculated from the data rises because of small energy events, which are included in the data but apparently were not simulated by the Monte Carlo. As  $E_{\min}$  increases, the statistical error on "a" increases, but its value remains constant to within the error-bars. Furthermore, comparison of the individual NaI-energy spectra between data and Monte Carlo showed an excess of data events below 10MeV in TINA and 15MeV in MINA (see for example Figure 9.5). We therefore chose these two values as our  $E_{\min}$  for TINA and MINA respectively.

With a similar analysis of the  $60^\circ$  data, we obtained again as a good compromise, 0.5cm for CUTMAX and 10MeV for  $E_{\min}$  in TINA and MINA. This time, the individual energy spectra could not be called upon to determine  $E_{\min}$  since the Monte Carlo program simulated no events with  $x < 0.05$  whereas the data had many of these events present.

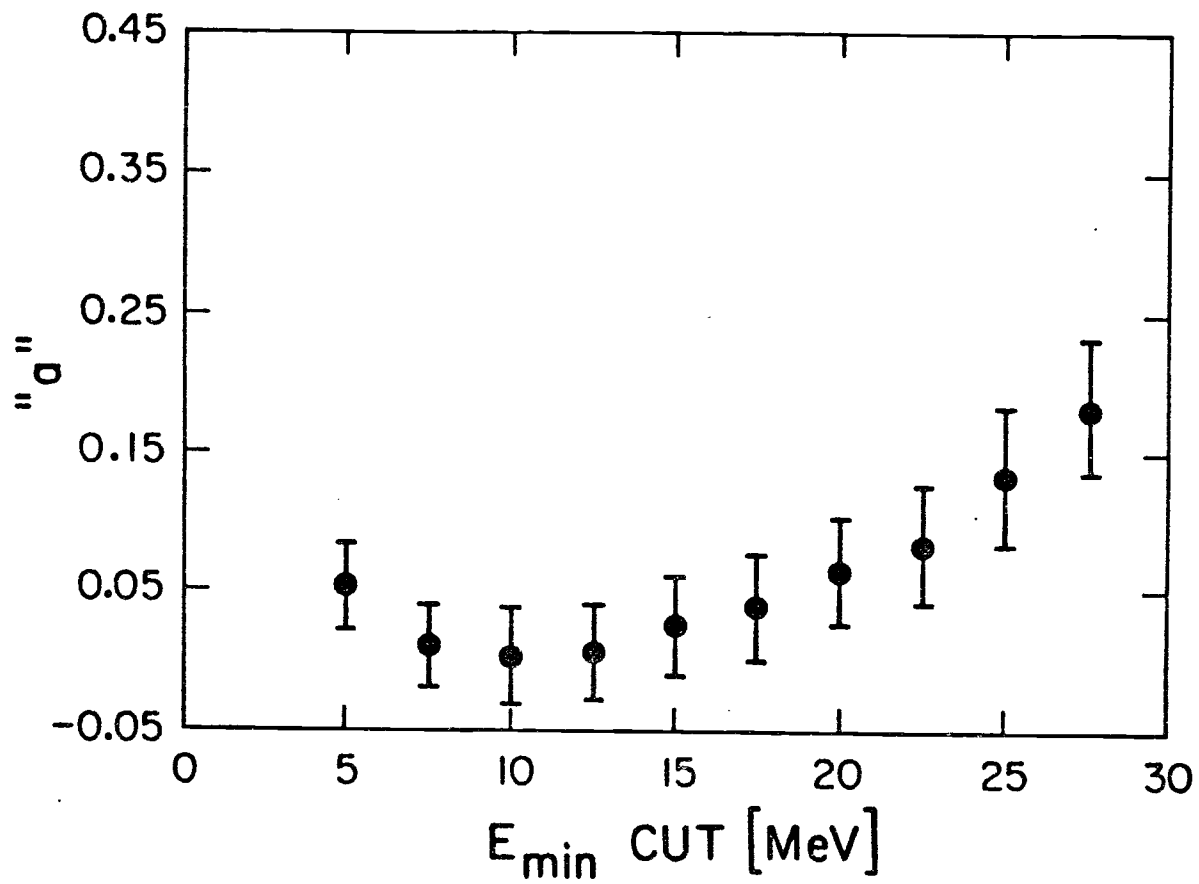


Figure 9.4 The form factor slope "a" obtained with the  $130^\circ$  geometry for different energy cuts,  $E_{\min}$ . The error-bars represent the statistical error only.

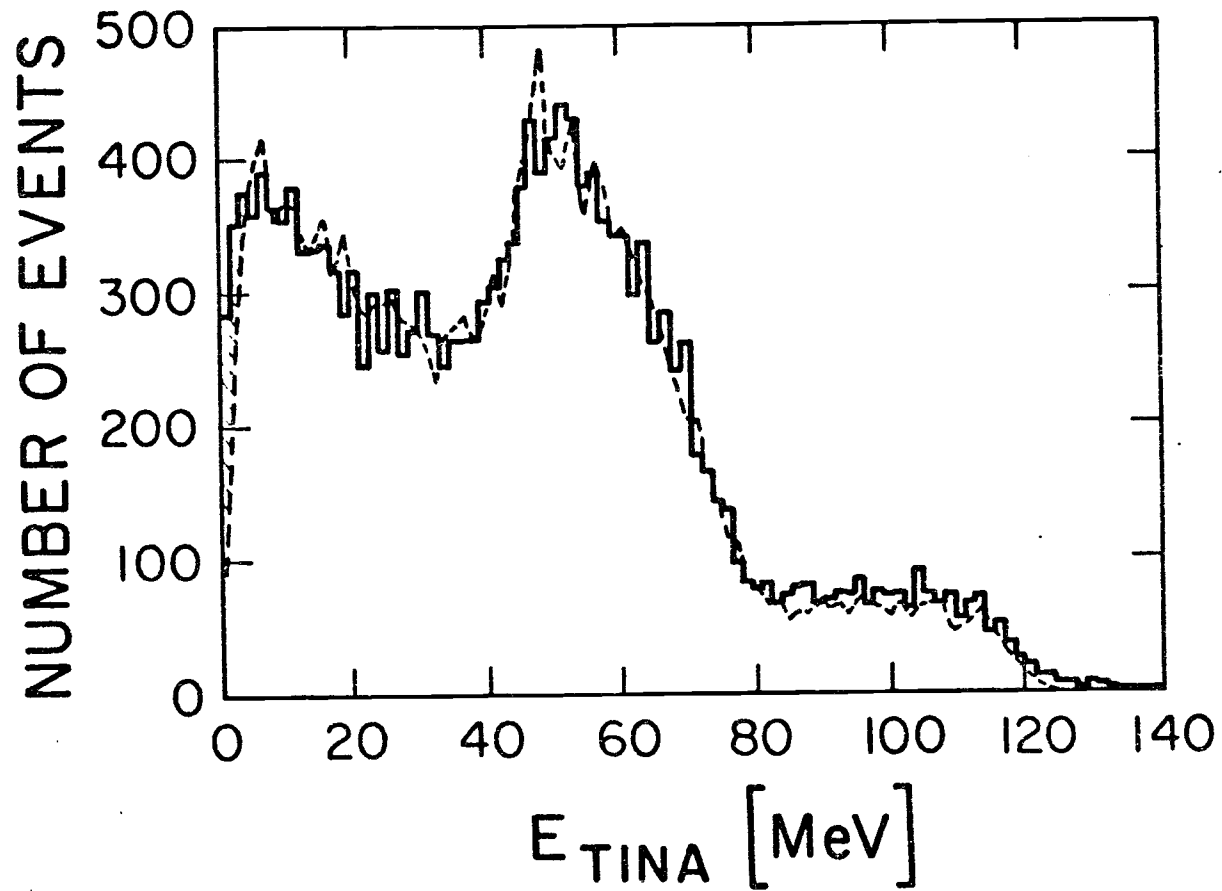


Figure 9.5 Energy distribution in TINA at  $130^\circ$  before an energy cut is applied. The data are represented by the histogram. The Monte Carlo result is the dashed curve.

For this reason, a cut on  $x$  was also required in the  $60^\circ$  analysis. We chose  $X_{\min}=0.1$ , which, given the detector resolutions, is safely above a possible value,  $x_{\text{vis}}$ , for an event with  $x=0.05$ .

The situation at  $156^\circ$  is not so clear. First of all, the Monte Carlo and real wire chamber resolutions are somewhat different (see Figure 9.6). The width of the distributions are about the same but their position is shifted. This is caused by the fact that the wire chamber positions were recalibrated every time the detector arms had been moved. Apparently, a slightly better result ( $<0.2\text{mm}$ ) for the DIFMAX spectrum on TINA and MINA's side was achieved at  $130^\circ$  than was possible at  $156^\circ$ . A discrepancy of this small magnitude is not unexpected considering the accuracy of the calibration method. Nevertheless, it raises questions about the relative normalization between data and Monte Carlo. Some of this discrepancy may also be attributed to background events with poor tracking, still left in the data sample. Conceding a difference in the two spectra, we tried to remedy this problem by applying the CUTMAX at different places in the Monte Carlo and in the data. Unfortunately, the normalization is very sensitive to the relative position of these two cuts. We used the relative peak position of the spectra as the obvious scaling factor. The change in "a" as a function of CUTMAX in the Monte Carlo when the relative scaling is preserved, is shown in Figure 9.7. Again, CUTMAX=0.5 seemed to be a reasonable choice. The large value for "a" in Figure 9.7, is due to background which is not accounted for in the Monte Carlo simulation (see chapter 10). Changing  $E_{\min}$  for both TINA and MINA over a range from 5-25MeV helped little in reducing the relative size of the background and thus "a". It seems that this background cannot simply be eliminated with any reasonable value for  $E_{\min}$ . In the next chapter, we elaborate on what this background could be and why it is only present in the  $156^\circ$  data.

A second problem with the simulation at  $156^\circ$  relates to the assumed resolution of the NaI spectrometers for photons entering the crystals outside the defining counters. For them, no empirical resolution data were available from in-beam measurements. The

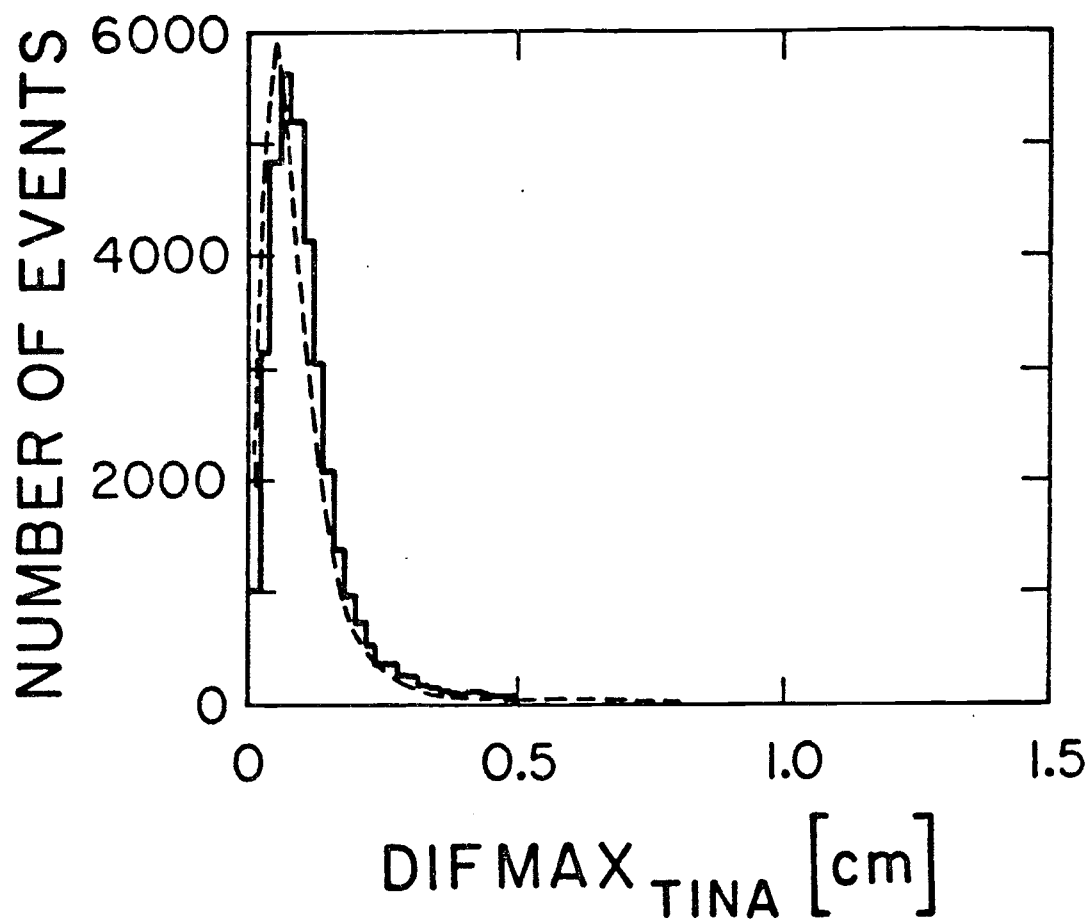


Figure 9.6  $DIFMAX$  distribution of the TINA-arm for the  $156^\circ$  geometry. The data are represented by the histogram. The Monte Carlo result is the dashed line.

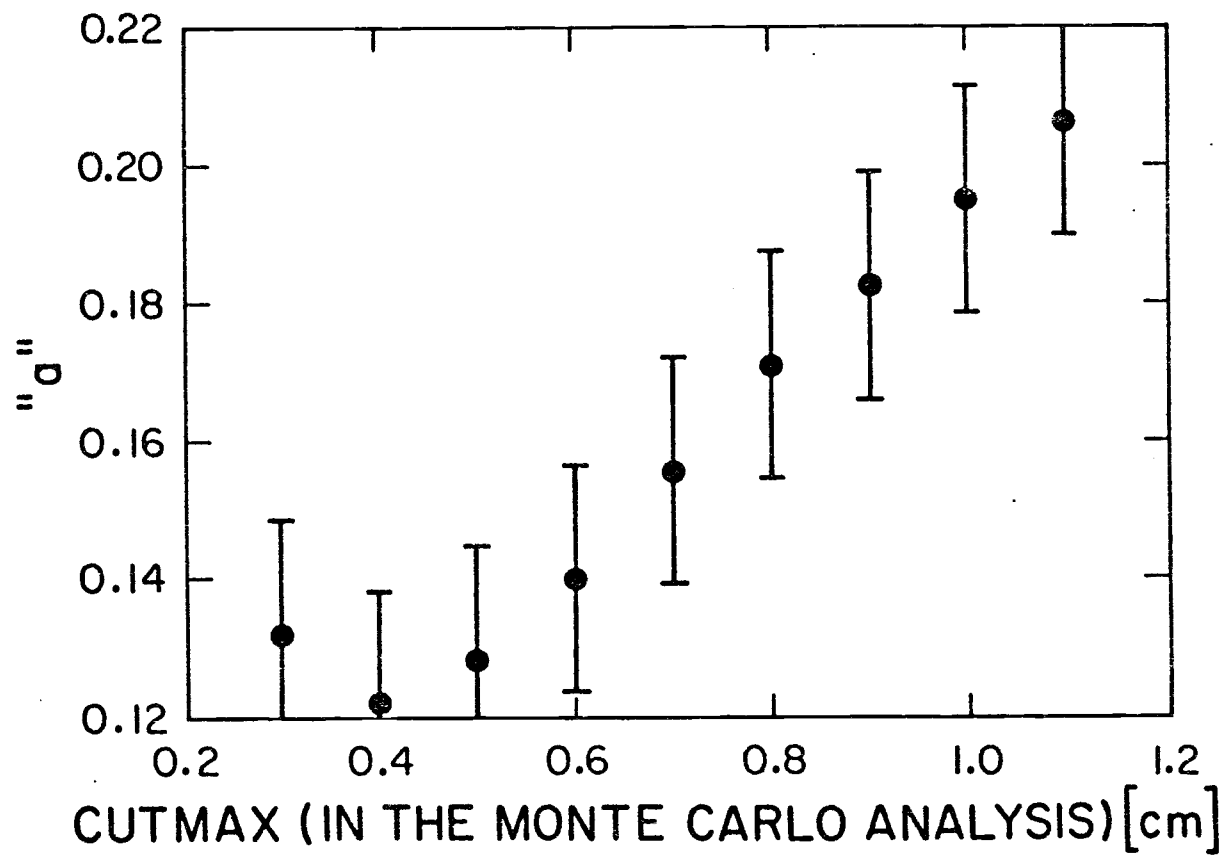


Figure 9.7 The form factor slope "a" obtained with different cuts on DIFMAX for the 156° geometry. The error-bars represent the statistical contribution only.

assumed resolutions at the rim of the crystals were taken from EGS-shower calculations. However, the intrinsic resolution of the detectors, beyond the spread due to shower leakage, had to be extrapolated from results with 0.66MeV photons. It is not clear, that this procedure is adequate to give the right Monte Carlo spectrum for variables such as  $E_{\text{tot}}$  and  $x_{\text{vis}}$ , which are combinations of  $E_{\text{TINA}}$  and  $E_{\text{MINA}}$ . Oddly enough, the individual energy spectra (see for example Figure 9.8) look quite reasonable, but if we plot the difference between data and Monte Carlo scatter-plots of  $E_{\text{MINA}}$  vs.  $E_{\text{TINA}}$  (see Figure 9.9), it becomes obvious that most of the discrepancy is in the region of Dalitz events where the photon is detected as well. The Monte Carlo simulation predicts very few of these events at  $130^\circ$  and so the above resolution problem never arises. This is the reason why the shape of the  $x_{\text{vis}}$  spectrum at  $130^\circ$  is very well reproduced in the Monte Carlo (see Figure 9.10), while we are incapable of simulating its shape properly at  $156^\circ$ .

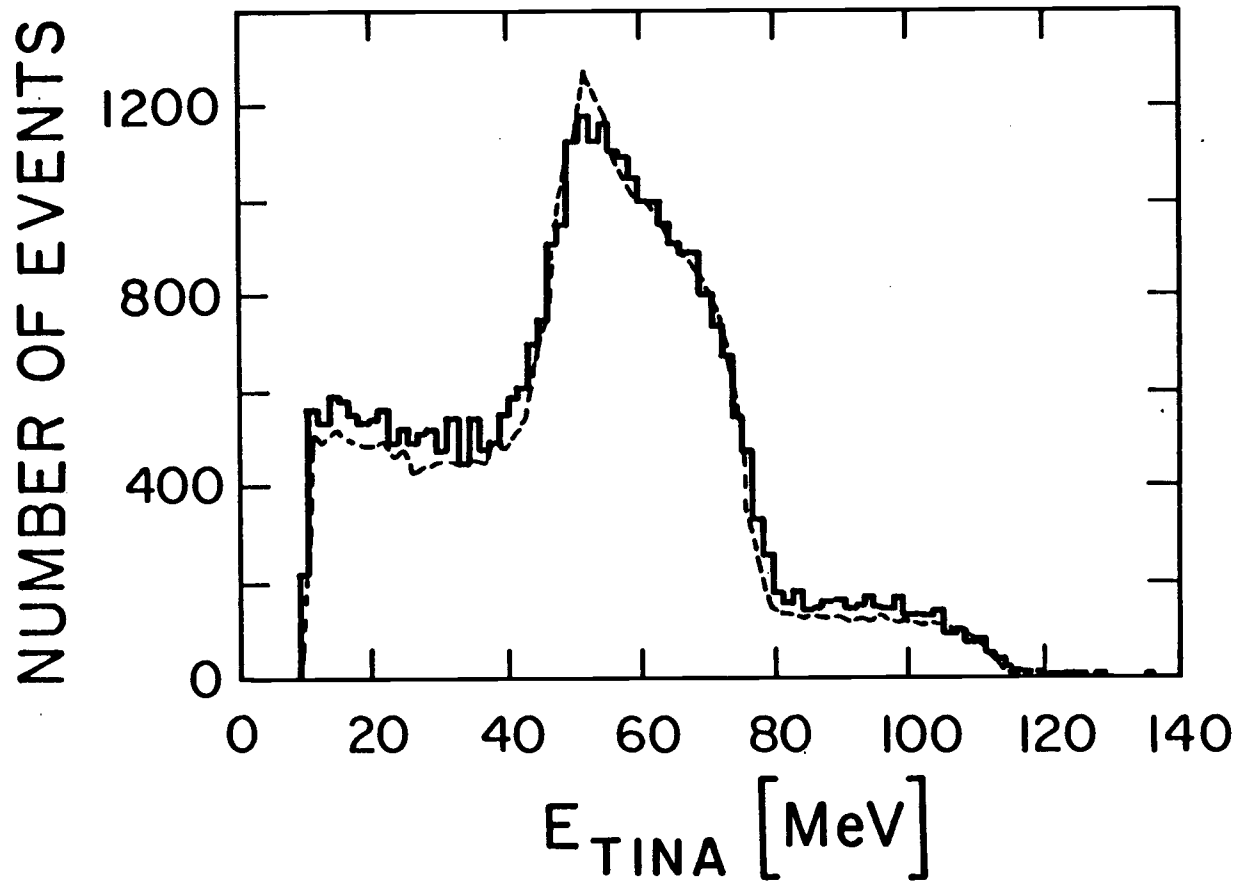


Figure 9.8 Energy distribution in TINA at  $156^\circ$  after all cuts are applied. The data are represented by the histogram. The Monte Carlo result is the dashed curve.

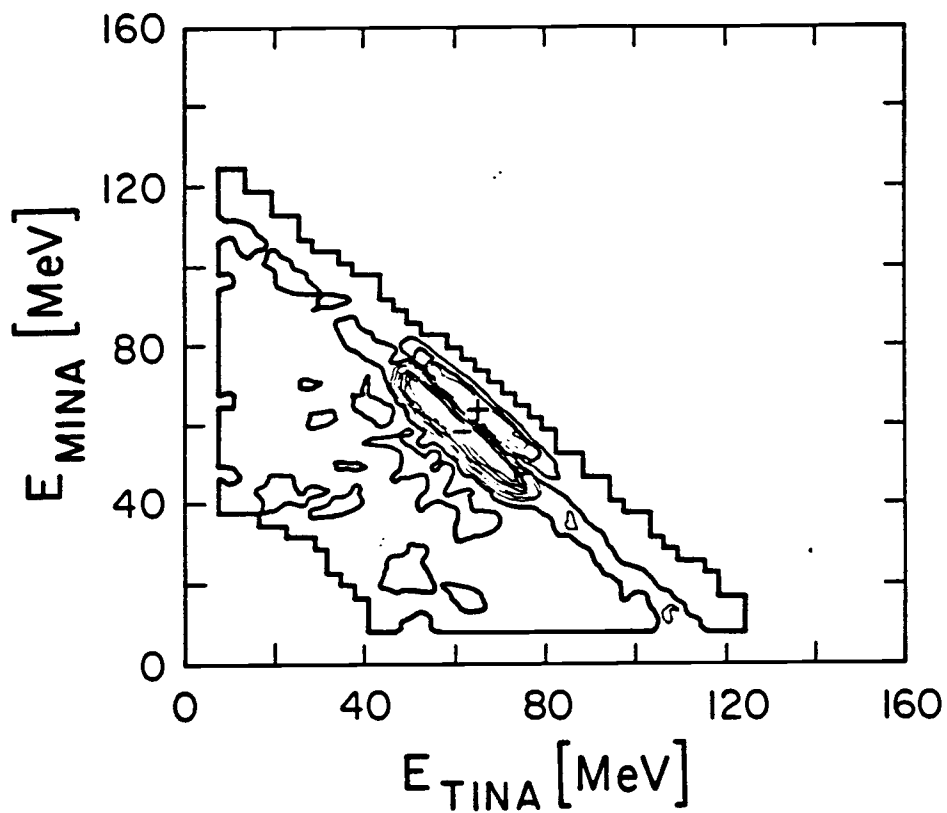


Figure 9.9 The difference (Data - Monte Carlo) of the scatter-plot  $E_{\text{MINA}}$  vs.  $E_{\text{TINA}}$  at  $156^\circ$ .

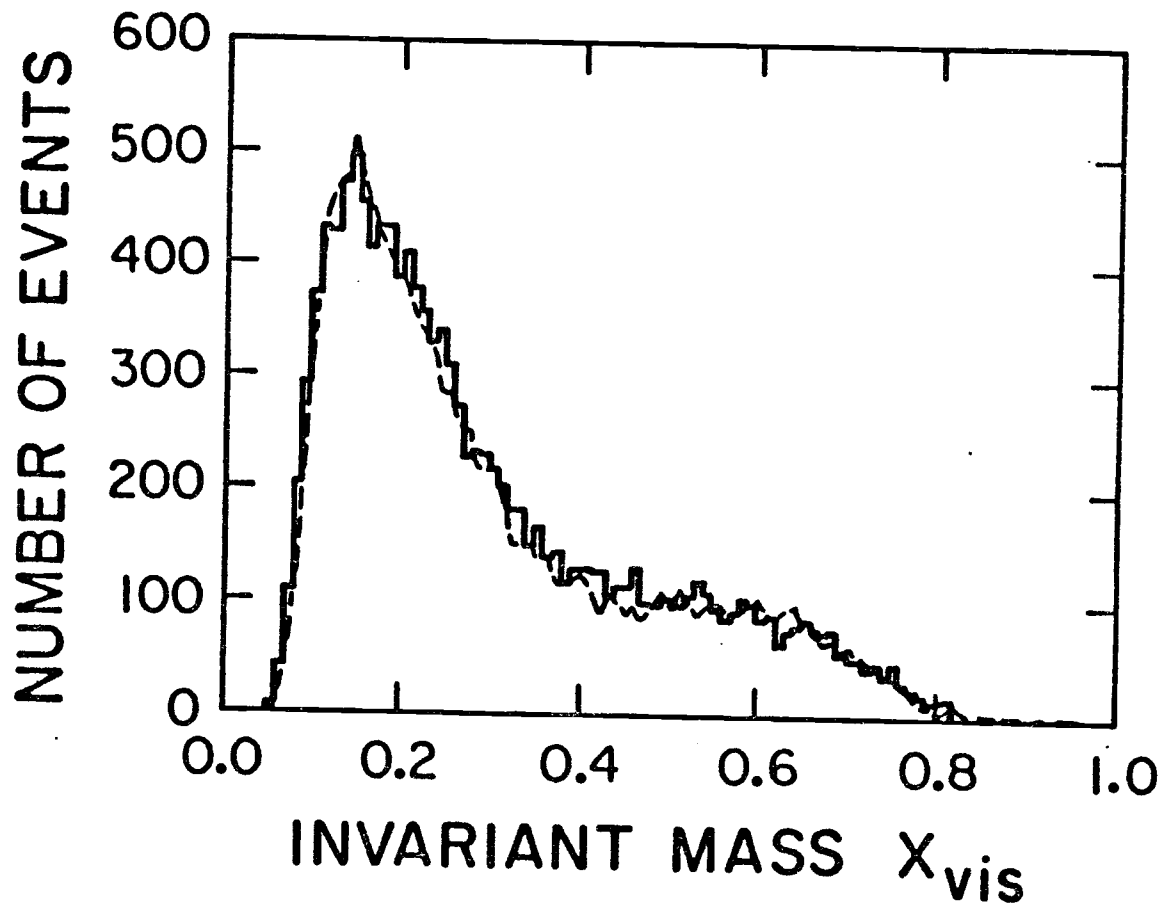


Figure 9.10 The invariant mass distribution  $x_{vis}$  at  $130^\circ$ . The data are represented by the histogram. The Monte Carlo result is the dashed curve.

## 10. RESULTS AND CONCLUSIONS

10.1 60° Geometry

With cuts applied to the 60° data, as outlined in chapter 9.3, we were left with 10402 events. These are the remaining events from  $1.099 \cdot 10^{10}$  "detectable"  $\pi^0$ 's in the target.<sup>15</sup> With this normalization and the same cuts applied to the Monte Carlo data, we arrived at the following prediction:

$$\begin{array}{ll}
 (1) \pi^0 \rightarrow e^+ e^- \gamma \quad (\Gamma_{SI}) & 802 \\
 (2) \pi^- p \rightarrow e^+ e^- n & 9978 \\
 (3) \pi^0 \rightarrow e^+ e^- e^+ e^- & 5 \\
 (4) \pi^0 \rightarrow e^+ e^- & 0 \\
 (5) \pi^0 \rightarrow e^+ e^- \gamma \Big|_{\rightarrow e^+ e^-, e^-} & 0 \\
 (6) \pi^0 \rightarrow \gamma \Big|_{\rightarrow e^+ e^-, e^-} \gamma \Big|_{\rightarrow e^+ e^-, e^-} & 0 \\
 (7) \pi^0 \rightarrow \gamma \gamma \Big|_{\rightarrow e^+ e^-} & 0 \\
 (8) \pi^- p \rightarrow n \gamma \Big|_{\rightarrow e^+ e^-} & 0 \\
 \\
 (9) \pi^0 \rightarrow e^+ e^- \gamma \quad (\Gamma_{SD}) & 136
 \end{array} \tag{10.1}$$

Reactions 7 and 8 are wide opening angle pair productions of a single photon, thought to be a possible background. The reason for the imbalance between Dalitz and  $\pi^- p \rightarrow e^+ e^- n$  events lies in the  $X_{\min}$  cut and does not reflect the detector geometry. For  $X_{\min} = 0.1$ , many more Dalitz events are eliminated than internal conversions. We are

<sup>15</sup> The adjective "detectable" refers to the number of  $\pi^0$ 's detectable with a  $4\pi$  detector having the same overall efficiency as our apparatus.

therefore, in effect, checking our Monte Carlo normalization almost exclusively with  $\pi^- p \rightarrow e^+ e^- n$  events.

With few Dalitz events left in the data sample and the sensitivity of this geometry to the  $\pi^0$ -form factor being already minimal, it is justifiable to set the unknown form factor slope equal to zero in the calculation:

$$N_{\text{norm}} = \frac{N_{\text{exp}}}{N_{\text{SI}} + 2a N_{\text{SD}} + N_{\text{B}}} \quad (10.2)$$

$N_{\text{B}}$  is the sum of background events, which in this case, is essentially the rate of internal conversions. With the numbers in (10.1), we obtain:  $N_{\text{norm}} = 0.965 \pm 0.02$ , where the error is statistical. To determine the systematic error from uncertainties in the overall normalization ( $\pm 1.4\%$ ), we simply changed the number of Monte Carlo events by this factor and recalculated  $N_{\text{norm}}$ . This gives:  $\Delta N_{\text{norm}} / N = \pm 0.01$ . The other systematic error is due to an uncertainty in the energy scale and was estimated by reanalysing the data with altered calibration functions. We changed the calibration by  $\pm 1$  channel at both calibration points (the pedestal and the center of the  $\pi^0$ -box). The result for this error is asymmetric,  $\Delta N_{\text{norm}} / N = \begin{matrix} +0.03 \\ -0.01 \end{matrix}$ , and reflects a steeply varying rate at the energy and x cut-off. Adding the independent systematic errors and the statistical error in quadrature yields:  $\begin{matrix} +0.04 \\ -0.02 \end{matrix}$ . We found that the fractional change in Dalitz rate due to radiative corrections is  $+0.8\% \pm 0.1\%$  (see chapter 8). With only few Dalitz events left in the data sample, the effect of this change on  $N_{\text{norm}}$  is minimal. Thus, our final result is:

$$N_{\text{norm}} = 0.965 \begin{matrix} +0.04 \\ -0.02 \end{matrix} \quad (10.3)$$

As it should be, this value is within errors consistent with one. The result serves as a check on the normalization, but the large error-bars make it impossible to see a systematic shift in the result

on a scale smaller than 1%. Had this been possible, we would have been able to renormalize the other geometries and thus automatically correct for unknown errors in the overall normalization.

There is no penalty for normalizing on  $\pi^- p \rightarrow e^+ e^- n$ , since it not only checks the overall normalization but also the relative rate of Dalitz decays and internal conversions. In particular, it examines the rate prediction of the theory code used to simulate the reaction  $\pi^- p \rightarrow e^+ e^- n$  [38]. At the outset of this experiment, several conflicting results for the differential decay rate of this process were available in the literature [6,47-50]. Our result confirms the independent calculation of D. Beder [38] to the 4% level.

## 10.2 $130^\circ$ Geometry

Again, the cuts mentioned in chapter 9.3, reduced the data sample to 11736 events. They correspond to  $7.95 \cdot 10^9$  "detectable"  $\pi^0$ 's in the target. The Monte Carlo simulation predicts the following event rate:

$$\begin{aligned}
 (1) \quad \pi^0 &\rightarrow e^+ e^- \gamma \quad (\Gamma_{SI}) & 7713 \\
 (2) \quad \pi^- p &\rightarrow e^+ e^- n & 3705 \\
 (3) \quad \pi^0 &\rightarrow e^+ e^- e^+ e^- & 310 \\
 (4) \quad \pi^0 &\rightarrow e^+ e^- \gamma \Big|_{\rightarrow e^+ e^-, e^-} & 10 \\
 (5) \quad \pi^0 &\rightarrow \gamma \Big|_{\rightarrow e^+ e^-, e^-} \Big|_{\rightarrow e^+ e^-, e^-} & 16 \\
 (6) \quad \pi^0 &\rightarrow e^+ e^- \gamma \quad (\Gamma_{SD}) & 2296
 \end{aligned}
 \tag{10.4}$$

Inserting these numbers into the equation:

$$a = \frac{N_{\text{exp}} - N_{SI} - N_B}{2N_{SD}}
 \tag{10.5}$$

yields:  $a = -0.00 \pm 0.035$ , where the error is statistical. This error was calculated from the formula:

$$\left( \frac{\Delta a}{a} \right)^2 = \frac{1}{N_{SD}} + \frac{N_{exp} + N_{SI} + \sum_i (R_i)^2 N_{Bi}}{\left( N_{exp} - N_{SI} - \sum_i R_i N_{Bi} \right)^2} \quad (10.6)$$

where  $1/R_i$  is the fraction of Monte Carlo events simulated for a given background process relative to the number of these events in the data sample. The systematic errors due to uncertainties in normalization and energy calibration were determined in the same way as outlined in chapter 10.1. The results are  $\Delta a_N = \pm 0.04$  and  $\Delta a_E = +0.05$  and  $-0.02$ . We obtained again an asymmetric error  $\Delta a_E$ , reflecting a steep change in rate near the energy cut. Adding all errors in quadrature yields  $+0.08$  and  $-0.06$ . We found that the fractional change in Dalitz rate due to radiative corrections is  $+0.5\% \pm 0.4\%$  (see chapter 8). This change in rate produces a change in "a",  $\Delta a = -0.01 \pm 0.01$ . The final result is then:

$$a = -0.01 \begin{array}{l} +0.08 \\ -0.06 \end{array} \quad (10.6)$$

This result is in accord with most theoretical calculations indicating that there is no unexpected structure in the  $\pi^0$  transition form factor.

It should be noted at this point, that there is a dependence of the result for "a" on the assumed stopping distribution in the target. It is very difficult to extract the correct stopping distribution from the data. First of all, the measured stopping distribution is different from the real stopping distribution by resolution effects of the wire chamber telescopes. Secondly, any correlation between the coordinates in the real distribution becomes lost if the three coordinates are sampled separately. If now the resolution effects are position dependent, one does not retrieve the measured stopping distribution along the coordinate axis, even though they served as input for the Monte Carlo (see Figure 10.1). We

found, that the rate for accepted Dalitz events could be changed by about 1% depending on the approximations used to sample the stopping distribution. This can change "a" by  $\pm 0.03$ .

Future  $\pi^0$  form factor experiments should be designed with this difficulty in mind. One exotic solution is an active target, where the liquid hydrogen serves as drift media for the drift chamber. In another solution, larger detectors could be placed at a greater distance from the target. This preserves the solid angle, but reduces the sensitivity of the acceptance to the exact stopping distribution.

### 10.3 $156^\circ$ Geometry

We already mentioned two problems with the analysis of the  $156^\circ$  data in chapter 9.3. Figure 9.9 shows a small excess of events in the data sample over the Monte Carlo, across the entire region of accepted events. We know, that a large number of small energy events present in the data were never reproduced in the Monte Carlo (see figure 10.2 and 9.2). There is no certainty that these events are confined to the region in the  $E_{\text{MINA}}$  vs.  $E_{\text{TINA}}$  scatterplot, which is free of simulated Dalitz events. It is more likely, that their spectrum extends into the accepted region and unless we can identify these events by other means, they will remain in the data.

The Monte Carlo program did not simulate electron showers in dense material, like the collimator or the target flanges, since otherwise the CPU-time requirement would have been astronomical. There is however a considerable chance for combinations of exiting shower particles to create valid trigger conditions. These showers are ever present since the target flanges and the collimator subtended large solid angles, and even though the analysis requirements are very restrictive, the rate from  $\pi^0 \rightarrow \gamma\gamma \rightarrow e^+e^-$  pairs is large enough to insure that some will survive. This background problem is especially stubborn, since its spectra contain no clear

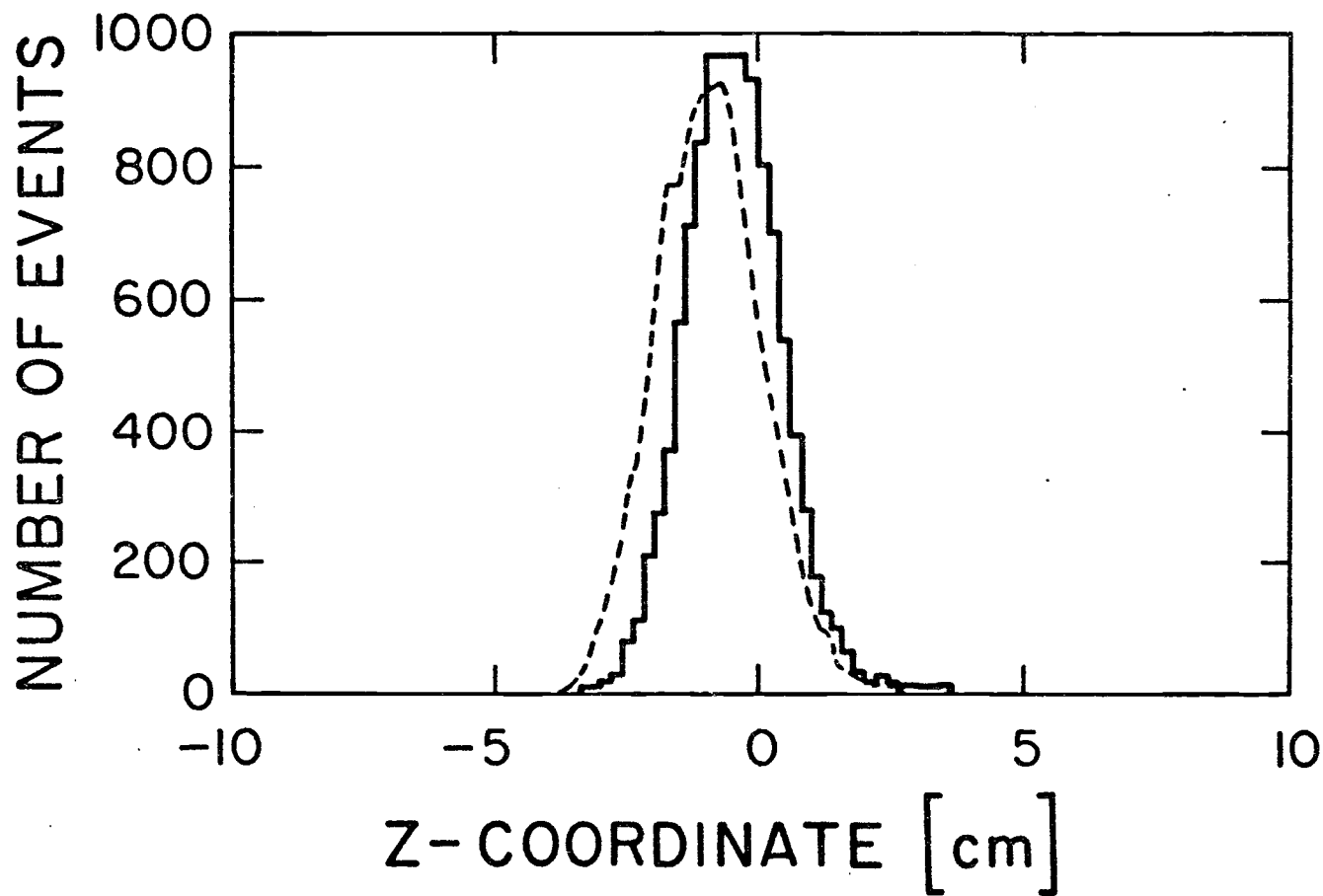


Figure 10.1 The  $\pi^-$  stopping distribution in the Z-direction (along the  $\pi^-$  beam) for the  $130^\circ$  geometry. The measured distribution is represented by the histogram. The result of the Monte Carlo simulation is the dashed curve.

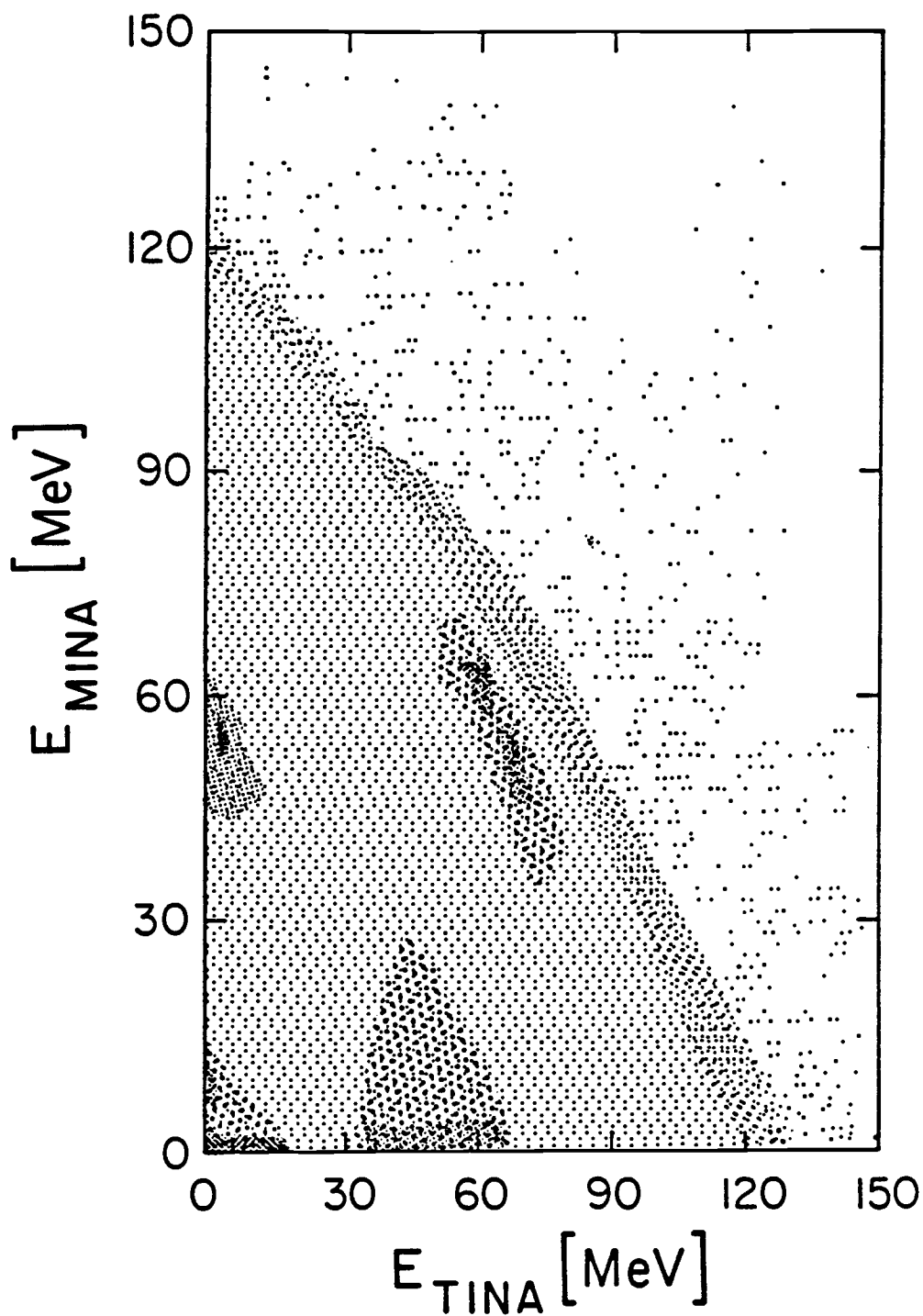


Figure 10.2  $E_{\text{MINA}}$  vs.  $E_{\text{TINA}}$  as measured with the  $156^\circ$  geometry before any cuts are applied to the data.

features. Unfortunately, we were not able to constrain the requirements, like straight tracking and target position, even further, because new uncertainties caused by resolution effects would have destroyed the confidence in normalization.

The Monte Carlo situation is further complicated by the possibility of electrons from showers in the NaI spectrometers exiting the crystal and then accidentally retrace back to the target. Even though this possibility seems remote, it is well known from EGS simulations, that electrons exit NaI-crystals in the backward direction. To include these events into the program, would require simulating the showers in NaI and redesigning the EGS geometry routine so that it can handle particles that travel back to the target.<sup>16</sup>

From these arguments it becomes apparent, that future measurements of the  $\pi^0$ -transition form factor should be built with the intention to reduce its dependency on a Monte Carlo simulation to a minimum. This can most directly be accomplished by a target design with no post and the target flanges far removed from the liquid hydrogen vessel. A definite identification of a charge particle pair originating in the target would also be helpful. Using NaI-crystals as the charge particle spectrometers forced us to use lead collimators to define the solid angle for photons. Replacing both NaI-crystals by magnetic spectrometers would eliminate the need for collimators. For a target completely surrounded by a magnetic detector, resolution effects may cause difficulties in determining the opening angle of the pair, especially when it is close to  $180^\circ$ . A magnetic field free region for the angle measurement would therefore be of advantage.

For a rate measurement, it is of utmost importance to have a very well defined acceptance. Plastic defining counters, as in the

<sup>16</sup> Note, the  $156^\circ$  geometry has a relative large acceptance for the required initial  $\pi^0 \rightarrow \gamma\gamma$  coincidence.

present experiment, serve this purpose very well. In any event, only a rate measurement along the lines of the present approach has a chance to measure "a" to a 1% accuracy.

We took most of our data at  $156^\circ$ , equivalent to  $1.71 \times 10^{10}$  "detectable"  $\pi^0$ 's. This results in a smaller statistical error:  $\pm 0.02$  and a smaller error due to normalization uncertainties:  $\Delta a_N = \pm 0.03$ . The data was also taken at a geometry which is less sensitive to calibration errors. We obtain  $\Delta a_E = \pm 0.01$ . By adding these errors in quadrature, we arrive at an overall error of  $\pm 0.04$ , in accord with our initial proposal. Unfortunately, our value for "a" is sensitive to the position of cuts designed to eliminate background evens, i.e., cuts on the straightness of the tracks in the wire chambers and cuts on target position. Loose cuts leave many unaccounted background events in the data sample whereas tight cuts are not admissible because of our ignorance of details in the detector resolutions. For this reason, we cannot quote a value for "a" from the analysis of the  $156^\circ$  data.

We were guided by considerations concerning calibration errors and sensitivity to "a", to take most of our data at  $156^\circ$ . We also knew, in view of the average opening angle between photons in  $\pi^0 \rightarrow \gamma\gamma$ , that this geometry would favor background events from external conversions. This background turned out to be more troublesome than originally anticipated because of our inability to simulate it well enough.

## APPENDIX

## BIBLIOGRAPHY

- [1] R. Hofstadter, R.W. McAllister, Phys. Rev. 98, 217 (1955).
- [2] J. Burger, Doctoral Thesis, Columbia Univ., New York, Physics (1972).
- [3] R.H. Dalitz, Proc. Phys. Soc. A64, 667 (1951).
- [4] C.N. Yang, Phys. Rev. 77, 242 (1950).
- [5] R. Plano, A. Prodell, N.Samios, M. Schwartz, J. Steinberger, Phys. Lett. 3, 525 (1959).
- [6] N.M. Kroll, W. Wada, Phys. Rev. 98, 1355 (1955).
- [7] N.A. Schardt et.al., Phys. Rev. D23, 639 (1981).
- [8] S.D. Drell, Nuovo Cimento 11, 692 (1959).
- [9] S.M. Berman, D.A. Geffen, Nuovo Cimento 18, 1192 (1960).
- [10] M. Gell-Mann, F. Zachariasen, Phys. Rev. 124, 953 (1961).
- [11] D. Geffen, B. Young, Phys. Lett. 15, 316 (1965)
- [12] G. Barton, B. Smith, Nuovo Cimento 36, 436 (1965).
- [13] A. Mukherjee, J. Phys. G4, 797 (1978).
- [14] H.S. Wong, Phys. Rev. 121, 289 (1961).
- [15] D.A. Geffen, Phys. Rev. 128, 374 (1962).
- [16] V.M. Budnev, V.A. Karnakov, Pis'ma Zh. Eksp. Teor. Fiz. 29, 439 (1979).
- [17] L.G. Landsberg, Phys. Rev. 128, #6, 301 (1985).
- [18] N. Samios et.al., Phys. Rev. 121, 275 (1961).
- [19] H. Kobrak et.al., Nuovo Cimento 20, 1115 (1961).
- [20] S. Devons et.al., Phys. Rev. 184, 1356 (1969).
- [21] R.I. Djhelyadin et.al., Phys. Lett. 94B, 548 (1980).
- [22] J. Fischer et.al., Phys. Lett. 73B, 359 (1978).
- [23] S.L. Adler, Phys. Rev. 177, 2426 (1969).
- [24] H.J. Schnitzer, S. Weinberg, Phys. Rev. 164, 1828 (1967).
- [25] I.S. Gerstein, H.J. Schnitzer, Phys. Rev. 170, 1638 (1968).
- [26] A.I. Ivanov, V.M. Shekhter, Sov. Journ. Nucl. Phys. 32, 40 (1980).

- [27] M.A. Shifman, M.I. Vysotsky, Z. Phys. C10, 131 (1981).
- [28] A. Bramon, E. Masso, Phys. Lett. 104B, 311 (1981).
- [29] L. Bergstrom et.al., Phys. Lett. 126B, 117 (1983).
- [30] L.L. Ametller et.al., Nucl. Phys. B228, 301 (1983).
- [31] A. Pich, J. Bernabeu, Z. Phys. C22, 197 (1984).
- [32] K.S. Babu, E. Ma, Phys. Lett. 119B, 449 (1982).
- [33] J. Spuller et.al., Phys. Lett. 67B, 479 (1977).
- [34] C. Oram et.al., Nucl. Inst. Meth. 179, 95 (1981).
- [35] A.M. Sandorfi, M.T. Collins, Brookhaven National Lab. report, BNL-33720 (1983).
- [36] R.L. Ford, W.R. Nelson, SLAC report 210, (1978).
- [37] R.L. Carrington et.al., Nucl. Inst. Meth. 163, 203 (1979).
- [38] D. Beder, private communication and unpublished internal group report.
- [39] T. Miyazaki, E. Tagasugi, Phys. Rev. D8, 2051 (1973).
- [40] L. Roberts, J. Smith, State Univ. of New York at Stony Brook, preprint ITP-SB-85-90 (1985).
- [41] G.B. Tupper, T.R. Grose, M. Samuel, Phys. Rev. D28, 2905 (1983).
- [42] M. Lambin, J. Pestieau, Phys. Rev. D31, 211 (1985).
- [43] D. Joseph, Nuovo Cimento 16, 997 (1960).
- [44] K.O. Mikaelian, J. Smith, Phys. Rev. D5, 1763 (1972).
- [45] K.O. Mikaelian, J. Smith, Phys. Rev. D5, 2890 (1972).
- [46] B.E. Lautrup, J. Smith, Phys. Rev. D3, 1122 (1971).
- [47] R. Garland, Doctoral Thesis, Columbia Univ. New York, Physics (1972).
- [48] S. Fubini, Y. Nambu, V. Wataghin, Phys. Rev. 111, 329 (1958).
- [49] H. Barkhardl, R.K.P. Zia, J.D. Darts, J. Phys. A7, 40 (1974).
- [50] N. Dombey, B.J. Read, Phys. G3, 1659 (1977).
- [51] C. Waltham et.al., submitted to Nucl. Inst. Meth. (1986).
- [52] D. Berghofer, Doctoral Thesis, UBC, Vancouver, Physics (1979).

## MONTE CARLO GENERATING TECHNIQUES

When sampling from a distribution in a Monte Carlo routine, it is imperative to devise a method with which the CPU-time requirement is minimized. The solution to this problem is often tailored to the particular distribution at hand. In this appendix, several sampling procedures are illustrated with the help of distributions that appear in the Monte Carlo simulation of the present experiment.

### A.1 Sampling from the Kroll-Wada distribution

The sampling from the Kroll-Wada distribution in the present Monte Carlo code differs from standard programs in that it allows for the leptons to have a minimum energy and minimum pair opening angle. With the minimum energy and opening angle different from zero, the possible range in  $x$  is restricted by a lower limit. This cut-off is given where the curve for the minimum allowed energy-sharing  $y$ , due to the opening angle requirement, intersects the maximum allowed  $y$ , due to the energy restriction. This situation is shown in Figure 3.9.  $x_{\min}$  is calculated for given  $E_{\min}$  and  $\theta_{\min}$  by numerically solving the transcendental equation  $y_{\max}(x) - y_{\min}(x) = 0$ . Where:

$$y_{\min} = \pm \left[ \frac{(1+x)^2}{(1-x)^2} - \frac{(8z - 16m_e^2)}{m_\pi^2 (1-x)^2} \right]^{1/2} \quad (\text{A.1})$$

with

$$z = (1/\sin^2 \theta_{\min}) * (2m_\pi^2 o * x + m_\pi^2 o * \cos \theta_{\min} * [x^2 - 1/4r(1+x)^2 \sin^2 \theta_{\min}]^{1/2})$$

$$r = 4m_e^2/m_\pi^2 o \quad ; \quad E_T = (m_\pi o/2)*(1+x) \quad ; \quad p_T = (m_\pi o/2)*(1-x)$$

$$y_{\max} = \frac{1}{p_T} \left( E_T^2 - 4E_{\min}(E_T - E_{\min}) \right)^{1/2}$$

To increase the speed with which the  $x$ -distribution is sampled, the whole range in  $x$  from  $x_{\min}$  to 1 is divided into 10 intervals. For each subrange an array of 100  $x$ -values is calculated so that each  $x$ -value corresponds to a 1% increment of the integral of  $f(x)$  over the same subrange.  $f(x)$  is the Kroll-Wada distribution:

$$f(x) = \frac{(1-x)^3}{x} \left[ 2y_{\max} \left( 1 + \frac{x}{y_{\max}} \right) + \frac{2}{3}y_{\max}^2 - 2y_{\min} \left( 1 + \frac{x}{y_{\min}} \right) - \frac{2}{3}y_{\min}^3 \right] \quad (\text{A.2})$$

Curves of  $f(x)$  for different values of  $E_{\min}$  and  $\theta_{\min}$  are shown in Figures A.1 and A.2. In order to use the "direct" Monte Carlo method we need to invert the function  $F(\chi) = \int_{x-\min}^{\chi} f(x)dx$ , i.e., we have to find  $\chi$ -values which correspond to equally spaced values of  $F(\chi)$ . This is done by interpolating between previously calculated values of  $F(\chi)$  where the  $\chi$ -values were equally spaced. This procedure creates a look-up table with a hundred entries for each interval. The different intervals are selected according to their contribution to the total  $x$ -integral over the full allowed range. All integrations are done numerically. Since the distribution  $f(x)$  can be highly peaked for small  $x$ , it is important to use more than one interval. Only then, one obtains finely spaced values of  $x$  over the entire range.

To get a distribution of the variable  $x$  inside an interval, the addresses of the look-up table are called randomly. To fine-tune this method, an interpolation is performed between neighbouring values. The energy partition  $y$  between  $y_{\min}$  and  $y_{\max}$  is sampled by the "rejection" technique described in A.4.

To improve the efficiency of creating detectable Dalitz pair events further, we first "throw" the positron direction uniformly into the solid angle of either TINA or MINA. Since we chose to fix the positron direction first, the direction of the  $\pi^0$  is no longer arbitrary in the lab frame. It can be shown, that in a frame where the positron is along the positive  $z$ -axis, the angle  $\theta_{\pi^0 e^+}$  between

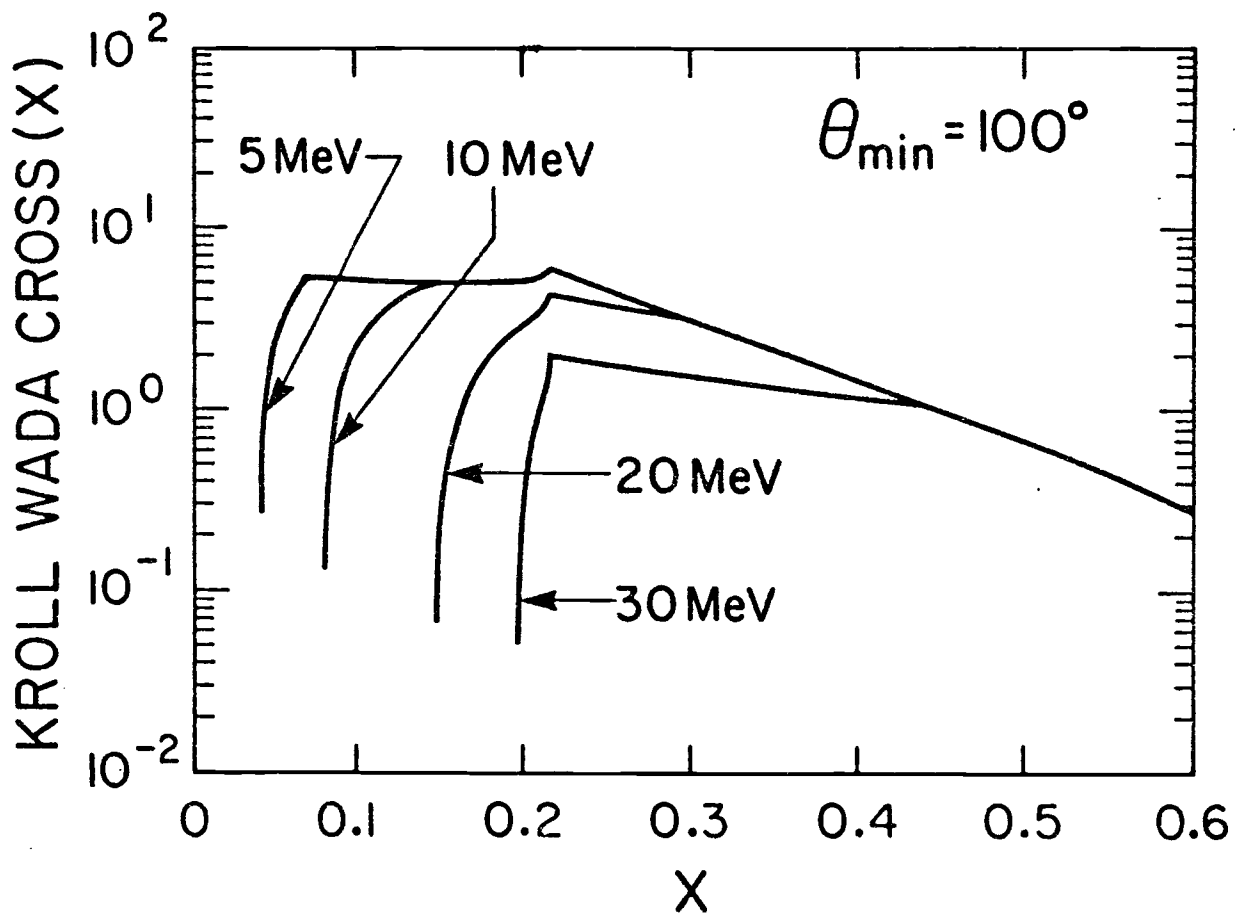


Figure A.1 Kroll-Wada distribution for Dalitz pairs with  $\theta_{\min} = 100^\circ$  and lepton energies  $E > E_{\min}$ .

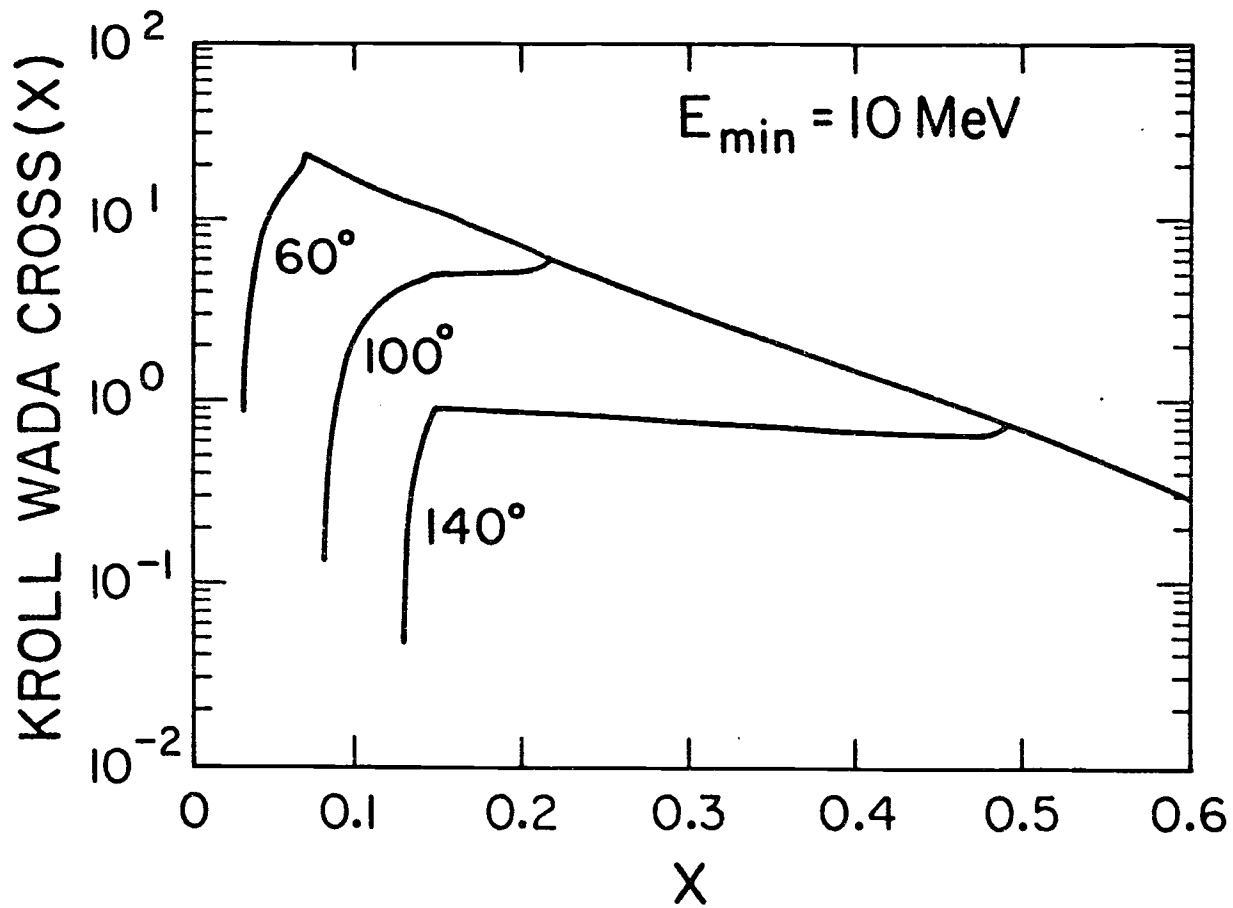


Figure A.2 Kroll-Wada distribution for Dalitz pairs with  $E_{\min} = 10 \text{ MeV}$  and lepton pair angles  $\theta > \theta_{\min}$ .

$\pi^0$  and  $e^+$  satisfies the distribution:

$$[ 1 / ( 1 - \beta \cos \theta_{\pi^0 e^+} ) ] \quad \text{where } \beta = 0.2037 \quad (\text{A.3})$$

In this frame, the azimuthal angle  $\phi_{\pi^0 e^+}$  is still uniform. The energies of the positron and electron are found by solving the equation:

$$(m_{\pi^0}^2/4) [(1+x) + (1-x)y] = E_{\pi^0} E_{e^+} - \vec{P}_{\pi^0} \cdot \vec{P}_{e^+} \quad (\text{A.4})$$

$$(m_{\pi^0}^2/4) [(1+x) + (1-x)y] = E_{\pi^0} E_{e^-} - \vec{P}_{\pi^0} \cdot \vec{P}_{e^-}$$

The cosine between the lepton pair is given in the  $\pi^0$ -rest frame by:

$$\cos \theta_{e^+ e^-} = (2E_{e^+} E_{e^-} - x * m_{\pi^0}^2 + 2m_e^2) / (2|\vec{P}_{e^+} + \vec{P}_{e^-}|) \quad (\text{A.5})$$

We have to transform  $\vec{P}_{e^+}$  from the lab into the  $\pi^0$ -rest frame and pick  $\vec{P}_{e^-}$  so that  $\phi_{e^+ e^-}$  is uniform around  $\vec{P}_{e^+}$  and  $\cos \theta_{e^+ e^-}$  is given by eq. A.5. The photon momentum is opposite to the pair momentum in the  $\pi^0$ -rest frame. Finally,  $\vec{P}_{e^+}$  and  $\vec{P}_{e^-}$  are transformed back into the lab-system.

## A.2 Sampling from empirical spectra

To simulate an empirical spectrum, it is first summed and normalized to get an integral of the histogrammed variable. This integral is then inverted and the values of the independent variable corresponding to equal increments of the integral are stored in an array. To get a distribution of that variable the addresses of the array are called randomly and if need be an interpolation is performed between neighbouring values. This technique is used to get the wire chamber sum distributions, and to sample the statistical deviations of a straight line fit from the actual wire chamber hits.

### A.3 Sampling from the NaI detector response function

The NaI response function is given in closed form:

$$f(e') = \tilde{A} \exp \left( \frac{(e'-b)}{d} \left[ 1 - \operatorname{erf} \left( \frac{(e'-b)}{c} \right) \right] \right) \quad (\text{A.6})$$

where  $b = E_{\text{dep.}} + \Delta$

$\Delta$ ,  $c$  and  $d$  are response function parameters. They were obtained from beam electron studies (see chapter 6.4) and were tabulated as functions of angle and radius of particle entry. The measured energy is given by:

$$E_{\text{measured}} = b + e \quad (\text{A.7})$$

The function in eq. A.6 can be integrated analytically to give:

$$F(e) = \int_{-\infty}^e f(e') de' = \tilde{A} \left[ \exp\left(\frac{e}{d}\right) \left(1 - \operatorname{erf}\left(\frac{e}{c}\right)\right) + \tilde{B} \left(\operatorname{erf}\left(\frac{e}{c}\right) - \tilde{C}\right) + 1 \right] \quad (\text{A.8})$$

Here:

$$\tilde{A} = \left[ 2 \exp(c^2/(4d^2)) \right]^{-1} \quad \tilde{B} = \exp(c^2/(4d^2)) \quad \tilde{C} = c/(2d) \quad (\text{A.9})$$

for

$$\int_{-\infty}^{\infty} f(e') de' = 1$$

Since the integral is normalized to one, we can set it equal to a random number between zero and one. This is known as the "direct" Monte Carlo method.

$$F(e) = \#_{\text{random}} \quad (\text{A.10})$$

We cannot solve for  $e$  in eq. A.10 and thus have to resort to a numerical method to find the zero. This causes no problem since  $F(e)$  is a well-behaved and monotonically increasing function.

#### A.4 Sampling by an optimized rejection technique

The following procedure for sampling the invariant mass distribution of the reaction  $\pi^- p \rightarrow e^+ e^- n$  was adopted from the thesis of J. Burger [2]. The total range of the invariant mass  $x$  is divided into subintervals and the "rejection" technique is applied separately in each interval after choosing between the intervals with the proper weighting. For a fixed number of subdivisions  $n$  the choice of partition can be optimized in the sense of minimizing the area in the boxes above the curve  $f(x)$  (shaded in Figure A.3). That is, we minimize:

$$S = \sum_{i=1}^n \left\{ f(t_{i-1}) (t_i - t_{i-1}) - \int_{t_{i-1}}^{t_i} f(x) dx \right\} \quad (\text{A.11})$$

(for  $f(x)$  monotonically decreasing [38])

For a minimum  $\partial S / \partial t_i = 0$ , we obtain a recurrence formula which gives all  $t_i$  inductively from  $t_0$  and  $t_1$ .

$$t_{i+1} = \frac{f(t_i) - f(t_{i-1})}{\left. \frac{\partial f}{\partial x} \right|_{t_i}} \quad (\text{A.12})$$

$t_0$  and  $t_1$  are initially chosen by trial and error such that  $t_n$  has its proper value. The weight of each subinterval is its rectangular area normalized to the total area of all boxes. We chose 19 subintervals as a compromise between complexity and CPU-time efficiency.

First, a subinterval is picked according to its weight. Then,  $x_{\text{trial}}$  is found random inside the partition. Whether this  $x$ -value is kept or the entire procedure repeated is decided by a new random number between 0 and the maximum of the function  $f(x)$  inside the interval. If this number is smaller than  $f(x_{\text{trial}})$ , the particular  $x$  is kept.

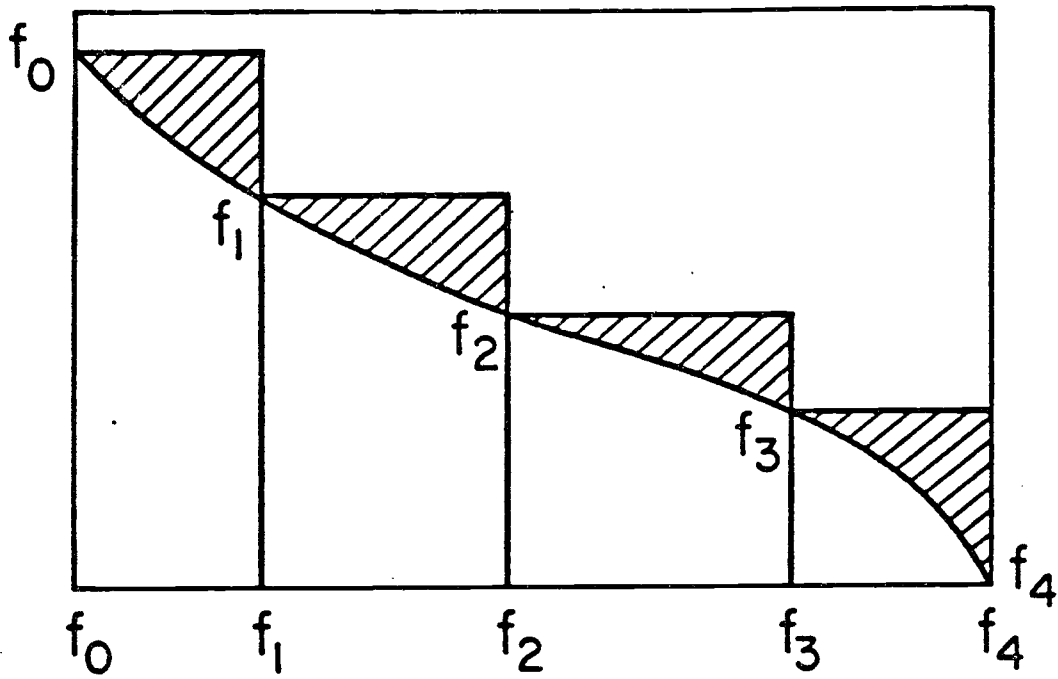


Figure A.3 Sketch of the optimized Monte Carlo "rejection" technique

Once the invariant mass  $x$  is chosen, the energy partition  $y$  is picked random between  $-\eta$  and  $+\eta$ , where  $\eta$  is a limit set by  $x$ :

$$\eta = \left( 1 - (4m_e^2)/(m_\pi^2 o^*x) \right)^{1/2} \quad (\text{A.13})$$

By the "rejection" technique a second random number between 0 and  $g(\eta)$  decides whether this value of  $y$  should be retained.  $g(y)$  is given in reference [38] for  $\pi^- p \rightarrow e^+ e^- n$ . For the Dalitz decay:

$$g(y) = \left( 1 + (4m_e^2)/(m_\pi^2 o^*x) \right) + y^2 \quad (\text{A.14})$$